Gamma-rays and neutrons effects on optical fibers and Bragg gratings for temperature sensors

Adriana Morana

UNIVERSITÉ JEAN MONNET DE SAINT-ÉTIENNE (FRANCE)

and

UNIVERSITÀ DEGLI STUDI DI PALERMO (ITALIA)

Cotutelle PhD Thesis

Gamma-rays and neutrons effects on optical fibers and Bragg gratings for temperature sensors

Adriana Morana

Saint-Étienne, December 6th 2013

Supervisor	
Prof. A. BOUKENTER	University of Saint-Etienne, France
Prof. M. CANNAS	University of Palermo, Italy
Dr. E. MARIN	University of Saint-Etienne, France
Reviewer	
Dr. A. GUSAROV	SCK-CEN, Mol, Belgium
Prof. P. MÉGRET	University of Mons, Belgium
Examiner	
Prof. Y. OUERDANE	University of Saint-Etienne, France
Prof. F.M. GELARDI	University of Palermo, Italy
Dr. S. AGNELLO	University of Palermo, Italy
Prof. S. GIRARD	University of Saint-Etienne, France
Dr. J. PÉRISSE	Manager of AREVA NP, France

A mia Nonna...

Acknowledgements

This thesis has been realized thanks to a grant of the *Centre National de la Recherche Scientifique* (CNRS) and the *AREVA*, a French group working in the energy domain, in cotutelle between the *Laboratoire Hubert Curien* of Saint Etienne (France) and the *Department of Physics and Chemistry* of the University of Palermo (Italy), in collaboration with the French *Commissariat à l'Énergie Atomique et aux Énergies Alternatives* (CEA). Moreover, it was supported also by the Vinci project of the *French-Italian University*.

And we reached the end of this journey...
It is my wish to say thanks to all the important people that have made it possible.
To Prof. Aziz Boukenter and Prof. Youcef Ouerdane, for giving me the possibility to work in their research group, for guiding me through this thesis until the end and for finding always time for me.
To Prof. Marco Cannas, for having supported me once more: the distance has not stopped him to contribute strongly to this thesis.
To Dr. Emmanuel Marin, for sharing with me his knowledge about the gratings and for providing all we needed, from the gratings to the help during the experiments.
To Prof. Sylvain Girard, for his organizational abilities and his useful comments and suggestions.
To Prof. Roberto Boscaino and the LAMP group, for their interest and constructive discussions during my period in Palermo, especially to Dr. Simonpietro Agnello, Dr. Lavinia Vaccaro and Dr. Antonino Alessi, for their help.
To Claude Marcandella, for the his time spent with me in the CEA of Arpajon, for the X-ray irradiations.
To Jean-Yves Michalon, for his competence and patience in the installation of the experimental equipments.
To my first French family, Marilena, Xavier Luc and Cherif, today new doctors, for making happier the first period in France, that is always more difficult, and the second one, Monica, Diego and the new girls, Chiara and Serena, for standing me during the

thesis writing, in which I freaked out.
To my family, that, despite miles apart, is always my family, supporting and encouraging me all the time.
To Rossella, a new sister that knows me better than anyone and even so she is always there for me.
Merci et Grazie!

Adriana

Contents

Introduction

Nowadays the nuclear industry shows an increasing interest in the fiber optic technology for both data communication and sensing applications in nuclear plants. The optical fibers offer several advantages, such as small size, light weight and resistance to electromagnetic interference. Moreover, the sensors based on this technology do not need any electrical power at the sensing point, they have a quick response and they can be easily multiplexed: in the case of a temperature sensor, for example, several thermocouples can be substituted by a single fiber, resulting in a decrease of the waste material.

Beside these advantages, the use of fiber sensors can be influenced by the level of ionizing radiation. The fission reactors are one of the harshest environments: it is characterized by the highest dose of γ-rays, of the order of magnitude of GGy for a fuel cycle, besides a high flux of neutrons and an operating temperature higher than 300°C for the current reactors, known as generation III. Radiation exposure degrade the fiber transmission because of several phenomena, radiation-induced attenuation, emission and compaction, whose amplitude and kinetics depends on the fiber composition.

This work has been carried out in collaboration with AREVA, the French industrial conglomerate active in the energy domain, with the aim of realizing a temperature sensor resistant to the harsh environment of a nuclear reactor of generation IV, in particular a Sodium-cooled Fast Reactor: the sensor should withstand, in two years, a γ-dose of about 0.2 GGy, a neutron flux of 10^{19} n cm^{-2} and an operating temperature around 550°C. The currently used technology, the thermocouples, presents a drift of the measurement due to irradiation, that needs a calibration, and a response time of one second. In order to remove the drift, to reduce the response time (down to 0.5 s) and to increase the precision, two alternatives can be considered: improving the same technology or developing a new one. In regard to all the advantages of the optical fibers, a fiber optic temperature sensor was chosen. Moreover, using the optical fiber technology improves safety because of the temperature sensor diversification. Up to now, a lot of researchers focused their attention on the optical fiber system performances; however, no predictive model exists yet. Then, to understand the behavior of such system in a harsh environment, as the nuclear reactor

core, we have used an experimental approach based on complementary techniques such as radiation-induced attenuation, photoluminescence, electron paramagnetic resonance and Raman spectroscopies, for studying the mechanisms of formation and transformation of point defects and structural evolution.

The thesis is organized in 6 chapters. In chapter 1 is presented a brief introduction on silica optical fibers and the radiation effects. Then, in order to identify the most promising technology suitable for Areva's demand, in chapter 2 is reported the state of the art on the fiber optic temperature sensors. The chosen sensor for the aimed application is a Fiber Bragg Grating (FBG) written in a radiation-resistant fiber. The chapter 3 reports a detailed overview of this sensor: the different possible techniques to write the gratings in various classes of fibers, and in particular in the radiation-hardened one, the different types of gratings and their response under radiation. So, our research was addressed to determine the most radiation tolerant component made of a rad-hard fiber with a FBG written in it. Two types of fibers were taken into account, doped with germanium and/or fluorine. Because of their photo-sensitivity, FBGs can be easily written in Ge-doped fibers by using UV laser light and, for years, they have been the focus of attention of a lot of researchers for their application in harsh environments. The F-doped fibers, instead, are radiation-resistant, quality that makes them resistant also to the UV light of continuous wave or nanosecond pulsed lasers. A more recent technology allows the grating inscription in such fibers, by using femtosecond laser. As a consequence, we studied mainly FBGs written with femtosecond radiation at 800 nm, in both types of fibers. The chapter 5 reports the most important results concerning their behavior during high thermal treatments, up to 750°C, and during X-irradiation performed both at room temperature and at about 230°C. The chapter 6 is dedicated to the effects on the fiber transmission of the γ-rays, neutrons and thermal treatments. In order to identify the origin of the radiation induced attenuation, several spectroscopic techniques (reported in chapter 4) have been used. Finally, some conclusions and perspectives will be summarized.

Introduction

Aujourd'hui, l'industrie nucléaire montre un intérêt croissant pour les technologies basées sur les fibres optiques soit pour la transmission des données soit comme capteurs. Les fibres optiques offrent plusieurs avantages, petite taille, faible poids et une relative immunité vis-à-vis du rayonnement électromagnétique. En plus, les capteurs utilisant cette technologie n'ont pas besoin d'alimentation électrique au point de détection. Ils ont une réponse rapide et peuvent être facilement multiplexés : dans le cas d'un capteur de température, par exemple, plusieurs thermocouples peuvent être substituées par une seule fibre, résultant en une diminution des déchets.

Toutefois, les capteurs à fibres optiques peuvent être affectés par le rayonnement ionisant. Les réacteurs à fission nucléaire constituent un des environnements les plus agressifs : la dose de rayonnement gamma sur un cycle du combustible est de l'ordre du GGy avec une très forte fluence de neutrons et une température de fonctionnement supérieure à 300°C pour les réacteurs actuels, connus sous la dénomination de génération III. L'exposition aux radiations dégrade la performance des fibres à cause de plusieurs phénomènes : l'atténuation optique et l'émission induites par le rayonnement ainsi que le compactage dont l'amplitude et la cinétique dépendent de la composition de la fibre.

Ce travail a été réalisé en collaboration avec la société AREVA, industriel français actif dans le domaine de l'énergie, dans le but de réaliser un capteur de température résistant à l'environnement sévère d'un réacteur nucléaire de génération IV, réacteur à neutrons rapides refroidi au sodium liquide. Le capteur doit supporter, en deux ans, une dose gamma d'environ 0.2 GGy, une fluence neutronique de 10^{19} n cm^{-2} et une température de fonctionnement d'environ 550°C. La technologie actuellement utilisée, les thermocouples, présente une dérive de la mesure due au rayonnement nécessitant un étalonnage et un temps de réponse d'une seconde. Afin de supprimer la dérive, de réduire le temps de réponse (inférieur à 0.5 s) et d'augmenter la précision, deux possibilités peuvent être envisagées : l'amélioration de la même technologie ou le développement d'une nouvelle. Dans le cadre du développement d'une nouvelle technologie, le choix s'est porté sur un capteur de température à fibre optique. Le développement d'un tel capteur vise l'amélioration des performances et la diversification de la nature des capteurs pour renforcer le contrôle et par la même la sécurité. Jusqu'au présent, les chercheurs ont concentré leur attention sur les performances des capteurs à fibres optiques, mais aucun modèle prédictif n'existe encore. Dans un souci de compréhension des mécanismes à l'origine de la dégradation de tels capteurs dans un environnement sévère, comme le coeur d'un réacteur nucléaire, nous avons utilisé une approche expérimentale utilisant des techniques

complémentaires (atténuation spectrale, photoluminescence, résonance paramagnétique électronique et spectroscopie Raman) pour l'étude des mécanismes de formation et transformation des défauts ponctuels et l'évolution structurale en fonction de la sollicitation radiative.

La thèse est organisée en 6 chapitres. Dans le chapitre 1 est présentée une brève introduction sur les fibres optiques à base de silice et les effets du rayonnement. Le chapitre 2 reprend l'état de l'art sur les capteurs de température à fibres optiques ainsi que les motivations du choix de réseaux de Bragg (Fiber Bragg Grating ou FBG) inscrit dans une fibre résistante aux radiations pour l'application visée. Le chapitre 3 présente un résumé détaillé sur ce capteur : les différentes techniques utilisées pour inscrire les réseaux dans différentes classes de fibres, en particulier dans une fibre durcie, et les différents types de réseaux ainsi que leur réponse sous rayonnement. Deux types de fibres ont été retenues dans le cadre de cette étude : dopée au germanium et/ou au fluor. Grâce à leur photosensibilité, les fibres dopées au germanium permettent facilement la photoinscription de réseaux de Bragg sous UV. Pendant des années, ces réseaux ont été le centre d'attention pour leur utilisation dans des environnements sévères. Mais les fibres dopées au germanium ne présentent qu'une faible immunité au rayonnement ionisant. En revanche les fibres dopées au fluor présentent une bonne résistance dans certains environnements radiatifs mais ne permettent pas la photoinscription de FBG au moyen des installations standards sous UV. Une technologie plus récente utilisant un laser à impulsions femtosecondes permet de contourner cette difficulté. En conséquence, nous avons étudié principalement les FBG inscrits avec radiation laser femtoseconde à 800 nm dans les deux types de fibres. Le chapitre 5 présente les principaux résultats de l'étude des FBG en fonction des traitements thermiques à haute température, jusqu'à 750°C, et sous rayonnement X à la température ambiante et à 230°C. Le chapitre 6 est consacré aux effets du rayonnement gamma, des neutrons et des traitements thermiques sur la transmission des fibres. Afin d'identifier l'origine de l'atténuation induite par le rayonnement, plusieurs techniques spectroscopiques (présentées dans le chapitre 4) ont été utilisées. Le manuscrit se termine par quelques conclusions et perspectives de ce travail de thèse.

Introduzione

Oggigiorno l'industria nucleare mostra un interesse crescente nella tecnologia delle fibre ottiche sia per la trasmissione di dati sia come sensori negli impianti nucleari. Les fibre ottiche offrono diversi vantaggi: hanno dimensioni ridotte, sono leggere e non sono influenzate dai campi elettromagnetici. Inoltre, i sensori basati su questa tecnologia non necessitano d'energia elettrica nel punto di rilevamento, hanno una risposta rapida e possono essere facilmente "multiplexed", ossia combinati: nel caso di un sensore di temperatura, per esempio, diverse termocoppie possono essere sostituite da una unica fibra, con una conseguente riduzione delle scorie.

Nonostante questi vantaggi, l'uso dei sensori basati sulle fibre può essere influenzato dal livello di radiazione ionizzante. I reattori a fissione sono ambienti estremi: essi sono caratterizzati dalla dose più alta di raggi gamma, dell'ordine di grandezza dei GGy per un ciclo di combustibile, oltre ad un alto flusso di neutroni ed una temperatura di funzionamento superiore ai 300°C per i reattori attuali di III generazione. L'esposizione alla radiazione degrada la trasmissione delle fibre a causa di fenomeni, come l'attenuazione ottica e la compattazione, con entità e cinetiche che dipendono dalla composizione delle fibre.

Questo lavoro è stato realizzato in collaborazione con l'AREVA, industria francese attiva nel settore dell'energia, con l'obiettivo di realizzare un sensore di temperatura resistente all'ambiente di un reattore nucleare di IV generazione, veloce raffreddato al sodio: il sensore deve sopportare, in due anni, una dose gamma di circa 0.2 GGy, un flusso di neutroni di 10^{19} n cm^{-2} e una temperatura di funzionamento di circa 550°C. La tecnologia attualmente utilizzata, ossia le termocoppie, presenta una sistematica deriva della misura dovuta alla radiazione, che necessita di una calibrazione, e un tempo di risposta di un secondo. Per eliminare questi errori sistematici, ridurre il tempo di risposta (fino a 0.5 s) e aumentare la precisione, possono essere considerate due alternative: migliorare la stessa tecnologia o svilupparne una nuova. Dati i vantaggi sopra descritti, è stato scelto un sensore di temperatura a fibre ottiche. Inoltre, utilizzare la tecnologia a fibre ottiche migliora la sicurezza grazie alla diversificazione dei sensori di temperatura. Fino ad oggi, nonostante molti ricercatori abbiano focalizzato la loro attenzione sulle prestazioni dei sensori a fibre ottiche, non esiste ancora un modello predittivo. Quindi, per comprendere il comportamento di tali sistemi in un ambiente estremo come il nucleo di un reattore nucleare, abbiamo utilizzato un approccio sperimentale basato su tecniche complementari come l'attenuazione indotta dalla radiazione, la fotoluminescenza, la risonanza paramagnetica elettronica e la spettroscopia Raman, per studiare i meccanismi di formazione e

trasformazione dei difetti di punto e l'evoluzione stutturale.

La tesi è organizzata in 6 capitoli. Nel capitolo 1 viene presentata una breve introduzione sulle fibre ottiche in silice e gli effetti indotti dalla radiazione. Al fine di individuare la tecnologia più promettente adatta per la richiesta dell'Areva, nel capitolo 2 viene riportato lo stato dell'arte sui sensori di temperatura a fibre ottiche. Il sensore scelto per l'applicazione è un reticolo di Bragg (Fiber Bragg Grating o semplicemente FBG) iscritto in una fibra resistente alle radiazioni. Il capitolo 3 riporta uno studio dettagliato su questo sensore: le differenti tecniche utilizzate per iscrivere i reticoli nelle diverse classi di fibre, e in particolare in una resistente alla radiazione, i differenti tipi di reticoli e la loro risposta sotto irraggiamento. Quindi, la nostra ricerca è stata indirizzata a determinare il componente più tollerante alla radiazione realizzato da una fibra ed un FBG inscritto in essa. Due tipi di fibre sono state prese in considerazione, drogate con germanio e/o con fluoro. A causa della loro fotosensibilità, i FBG possono essere iscritti in fibre dopate con germanio usando luce laser UV e, per anni, sono stati al centro dell'attenzione di molti ricercatori per il loro uso in ambienti nucleari. Le fibre drogate con fluoro, invece, sono resistenti alla radiazione laser UV, sia continua sia pulsata al nanosecondo; l'iscrizione di reticoli in tali fibre può essere realizzata solo utilizzando laser al femtosecondo. Di conseguenza, abbiamo studiato principalmente FBG iscritti con radiazione laser a 800 nm con impulsi al femtosecondo in entrambi i tipi di fibre. Il capitolo 5 riporta i risultati più importanti che riguardano il loro comportamento durante trattamenti ad alta temperatura, fino a 750°C, e durante irraggiamenti X realizzati sia a temperatura ambiente sia a circa 230°C. Il capitolo 6 è dedicato agli effetti sulla trasmissione della fibra della radiazione gamma, dei neutroni e dei trattamenti termici. Per identificare l'origine dell'attenuazione indotta dalla radiazione, sono state utilizzate varie tecniche spettroscopiche (riportate nel capitolo 4). Infine, sono riportate le conclusioni e le prospettive di questo lavoro di tesi.

Chapter 1

Background on optical fibers and radiation effects

Before dealing with the fiber optic sensors in radiative environment, it is useful to introduce the optical fibers and the effects induced by the radiation on them and to provide the background to understand the results reported in this thesis. The chapter starts with a general description of optical fibers and some of their properties; it continues with the silica optical fibers: the structure and the most common defects of the silica glass, pure and doped with germanium, will be presented. Finally, the radiation effects on optical fibers will be introduced.

1.1 Optical fibers

An optical fiber [1, 2] is a dielectric waveguide operating at optical frequencies. Its simplest form is shown in fig. 1.1, it consists of a dielectric cylinder, called *core*, surrounded by a solid dielectric *cladding* whose refractive index is lower than that of the core. Usually, the core is made of glass, whereas the cladding can be made of glass or plastic. Thanks to this structure, the light is guided in the core along the fiber axis. To make the fiber more resistant, the cladding is surrounded by a coating, ensuring the mechanical properties of the device.

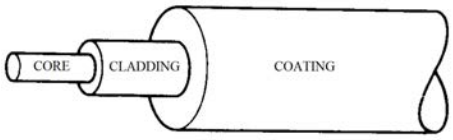

Figure 1.1: Structure of an optical fiber [1].

The propagation of the light along a waveguide can be described in terms of a set

of finite members of guided electromagnetic waves. Depending on the number of modes propagating through the core, the fiber is known as:

- *single-mode* (SM), if only one mode, the fundamental one, is guided in the core; this corresponds to a core diameter of about 8-12 μm, for fibers operating at IR telecom wavelengths;
- *multi-mode* (MM), if it can support several modes and it is characterized by a core diameter between 50 and 200 μm, for fibers working in the IR.

In fact, a single-mode fiber behaves as such only for wavelengths longer than a value known as *cutoff wavelength* [1]:

$$\lambda_{cutoff} = \frac{2\pi r_{core}}{V}\sqrt{n_{core}^2 - n_{clad}^2} \tag{1.1}$$

where V, the normalized frequency, is 2.405, for the telecommunication fibers. Generally, λ_{cutoff} is around 1250 nm in telecom fibers.

Depending on the refractive index profile (fig. 1.2), the fiber is called:

- *step-index* (SI), if the refractive index of the core is uniform and undergoes an abrupt change at the core-cladding interface;
- *graded-index* (GI), if the refractive index changes gradually with the radial distance inside the core. A particular graded-index fiber is the *multi-step index* fiber, whose refractive index parabolic profile is approximated by several steps.

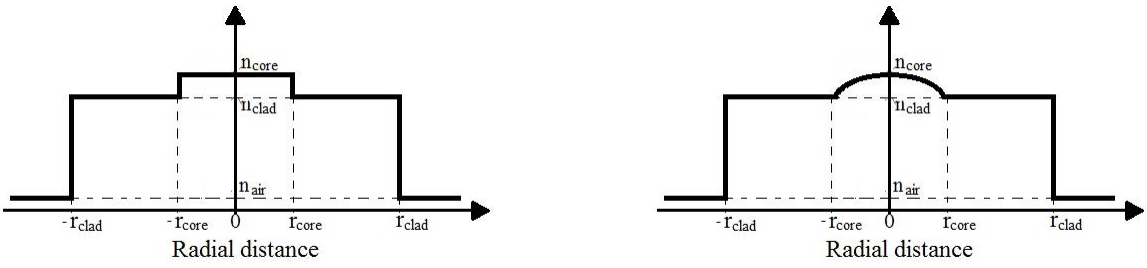

(a) (b)

Figure 1.2: Refractive index profile for (a) a step-index and (b) a graded-index fiber.

Another important parameter for an optical fiber is the *numerical aperture* (NA), a dimensionless quantity less than unity, which represents its capability of collecting light. For a step-index fiber, NA depends on the refractive index of the core and the cladding [1]:

$$NA = \sqrt{n_{core}^2 - n_{clad}^2} \tag{1.2}$$

Fiber loss

Optical attenuation is one of the most important properties of an optical fiber: it is the reduction of optical power as light travels through the waveguide; indeed, it is defined as the ratio of the optical output power from a fiber of length L to the optical input power and it is reported in dB/km. Fig. 1.3 reports a typical attenuation spectrum for a silica optical fiber.

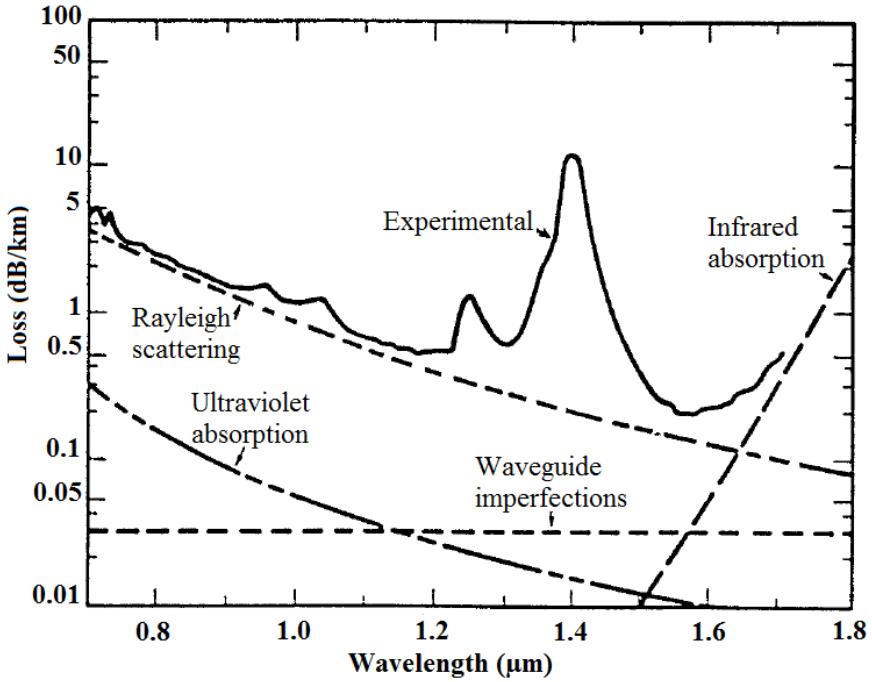

Figure 1.3: Attenuation spectrum of a silica based optical fiber [2].

The mechanisms causing the attenuation are [1]:

- scattering, that arises from microscopic variations in the material density or from structural inhomogeneities and depends on $1/\lambda^4$;
- absorption, that can be due to the fiber material constituents, as:
  - the IR-tail associated with the vibration modes of the molecules,
  - the UV-tail that is associated with the electronic transitions from the valence to conduction bands and decays exponentially with increasing wavelength,

or to impurities, as the OH groups which absorb around 2.73, 1.38 and 0.95 μm, or the defects in the glass, whose most common are reported in the next section;

- bending losses, particularly macrobending, when the fiber undergoes a bend having a radius larger than the fiber diameter, i.e. when a fiber turns a corner, and microbending, that is microscopic bends of the fiber axis, due, for example, to the drawing fabrication step or the incorporation into cables.

Generally, single-mode fibers have lower attenuation than the multi-mode ones, especially for silica-based optical fibers.

1.2 The silica glass

The material, that the fibers studied in this thesis are made of, is the silica glass. To produce two materials having slightly different refractive indices, dopants have to be added during the fabrication process, as GeO_2 in the core or F in the cladding, to increase the refractive index of the core or to decrease that of the cladding, respectively [1].

Two types of fibers have been mainly studied in this thesis: the Germanium-doped fibers, known for their photo-sensitivity, and the Fluorine-doped fibers, known for the radiation resistance to high γ-doses, reported in literature. To have a clear picture on the used materials, in this section the structure and the most common defects of the pure and the Ge-doped silica will be briefly introduced.

1.2.1 Silica: structure and defects

The amorphous silicon dioxide, known as silica (a-SiO_2), can be considered as a Continuous Random Network (CNR) of SiO_4 tetrahedra joined by bridging oxygen atoms [3]. The structural unit is the SiO_4 tetrahedron consisting of a silicon atom bounded with four oxygens atoms with the Si-O bond length of 1.62 Å and the O-Si-O angle of 109.5°, as for the quartz that is its crystalline form. The disorder of the glassy state is related to the continuous distribution in intertetrahedral Si-O-Si angle and torsion angles, in particular the Si-O-Si angle varies between 120° and 180°, with a maximum around $144° - 150°$, which are the values for the two types of quartz (α and β, respectively) [4]. The silica structure is constituted by n-membered $(Si\text{-}O)_n$ rings, where n is distributed between 3 and 10, with most of the rings having 6-7 size [4]. It was demonstrated that the 3-rings are planar and characterized by Si-O-Si angle of 130.5° and strained Si-O bonds, whereas the 4-rings can not be planar but slightly puckered with Si-O-Si angle of 160.5° [5, 6].

The presence of dopants or impurities, the fiber drawing and the radiation generate defects in the glass matrix. The most common intrinsic defects are listed below [7] and for each of them the structure is shown in fig. 1.4 and it is denoted with the most used symbolism, where (≡) and (=) indicate the bonds of a Si with three or two O atoms, whereas ($^\bullet$) and ($^{\bullet\bullet}$) represent an unpaired electron and two paired electrons in the same orbital:

- *E´ center* (≡Si$^\bullet$): it consists of a dangling silicon bond, with an unpaired spin in half-filled sp^3 orbital; this gives rise to a characteristic narrow EPR signal with axial symmetry;
- *neutral oxygen vacancy* or ODC(I) (≡Si-Si≡): it consists of a bonding between two Si atoms and it is diamagnetic;
- *twofold coordinated silicon* or ODC(II) (=Si$^{\bullet\bullet}$): it consists of a Si coordinated with two O atoms and having a lone pair (that is two paired electrons in the same orbital), it is a diamagnetic center;
- *non-bridging oxygen hole center* or NBOHC (≡Si-O$^\bullet$): it consists of a dangling oxygen bond; as it has an unpaired spin in an oxygen p orbital, it is paramagnetic;
- *peroxy linkage* (≡Si-O-O-Si≡): it is a vacancy of silicon and it is diamagnetic;
- *peroxy radical* or POR (≡Si-O-O$^\bullet$): it consists of a Si atom linked to an oxygen molecule with an unpaired electron that is delocalized on the two O atoms and makes the center paramagnetic;
- *self trapped hole* or STH [8], that are stable at temperatures lower than 200 K and can be divided in two types:
  - STH_1 consists of a hole trapped on a normal bridging oxygen in the glass matrix,
  - STH_2 is tentatively ascribed to a hole trapped on two normal oxygens;
- *self trapped exciton* or STE.

The defects give rise to electronic states within the bandgap and so to absorption bands, mainly in the UV and visible part of the spectrum. Fig. 1.5 reports the absorption (OA) bands associated with these defects [9]. However, the attribution is often not certain: whereas for the paramagnetic centers it is based on the correlation between the EPR signals and the OA bands, for the diamagnetic ones it is possible thanks to computational works or by observing defects conversion due to thermal treatments.

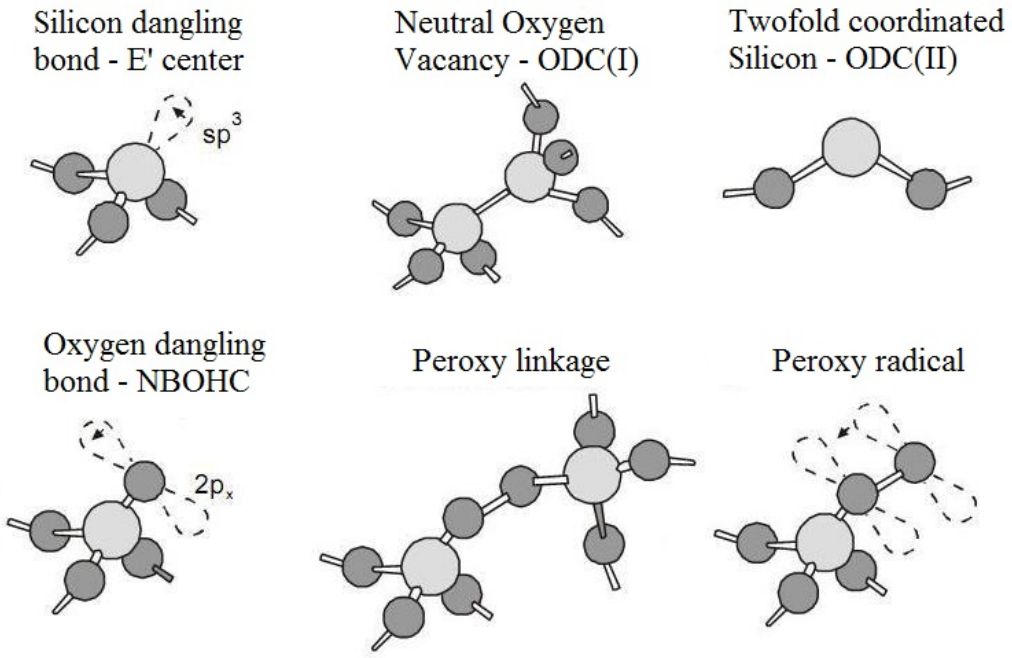

Figure 1.4: Intrinsic point defects in silica: at the top oxygen deficient centers and at the bottom oxygen excess-related centers [7]. The dark and light gray spheres represent O and Si atoms, respectively.

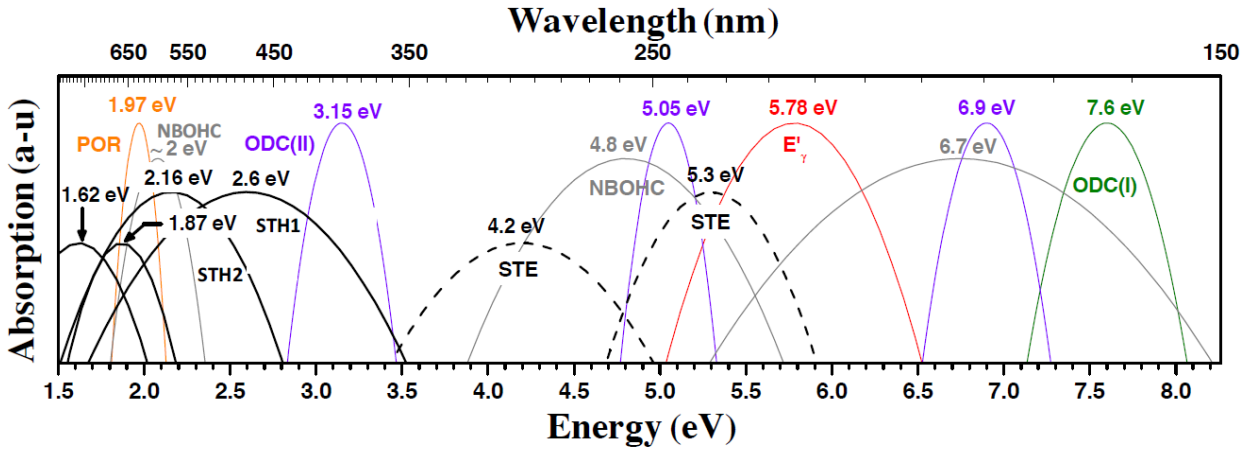

Figure 1.5: Summary of the main optical absorption bands of the Si-related defects in semi-logarithmic plot [9].

1.2.2 Ge-doped silica: structure and defects

The germanium is isoelectronic with the silicon and its amorphous oxide, known as germania (a-GeO_2), has the same structure of the silica. It is composed by tetrahedra linked through their corners, but the distribution of the Ge-O-Ge angle is peaked around 132° and is narrower and the Ge-O bond is longer, 1.74 Å, than in the case of a-SiO_2 [10].

When GeO_2 is incorporated into the silica glass, most of the small SiO_4 rings convert to larger mixed Ge/Si rings; so, the network is constituted by large (≥6-membered) SiO_4 rings, large (≥6-membered) mixed rings and small and large (≥3-membered) GeO_4 rings [10].

Due to the similarity between Si and Ge atoms, several Ge-related point defects are structurally identical to Si-related centers apart from the substitution of Si with Ge [11], as the *GeE´ center* (≡Ge$^\bullet$) and the *Ge-NBOHC* (≡Ge-O$^\bullet$), structurally identical to the E´ and the NBOHC, respectively, or the *Ge-lone pair center*, briefly GLPC (=Ge$^{\bullet\bullet}$), that is, as the twofold coordinated silicon, a dicoordinated Ge atom with a lone pair [12]. Other defects are the germanium electron centers:

- *Ge(1) center* ($GeO_4^\bullet$): it consists of an electron trapped by a substitutional tetra-coordinated Ge atom, it is a paramagnetic defect, typical only of the Ge-doped silica and not present in pure GeO_2, because the electron has to be localized on a Ge atom, condition verified when it has Si atoms as its neighbors [12];

- *Ge(2) center*, whose structure is still not unambiguously identified: a first model associates it with an electron trapped at a GeO_4, such as the Ge(1) center, but having a Ge atom as nearest neighbor [12,13], whereas, according to a second model, it consists of an ionized GLPC (=Ge$^\bullet$) [14];

and the GeX center, that is a diamagnetic defect whose structure is unknown but to whom an absorption band has been associated [15, 16].

The absorption bands associated with these Ge-related defects are reported in fig. 1.6. As for the Si-related defects, the attribution is still open to debate at least for the diamagnetic centers.

1.3 Radiation induced effects on optical fibers

A lot of researches demonstrated that the optical fiber properties change under irradiation, especially the transmission that is deteriorated because of three important phenomena:

- *Radiation Induced Attenuation* (RIA): the fiber attenuation increases because of the absorption bands of the point defects generated by the radiation through ionization and knock-on processes;

- *Radiation Induced Emission* (RIE): the photoluminescence emitted by some of centers (preexisting or induced by radiation), excited by the radiation itself, or the Cerenkov emission superpose on the transmitted signal;

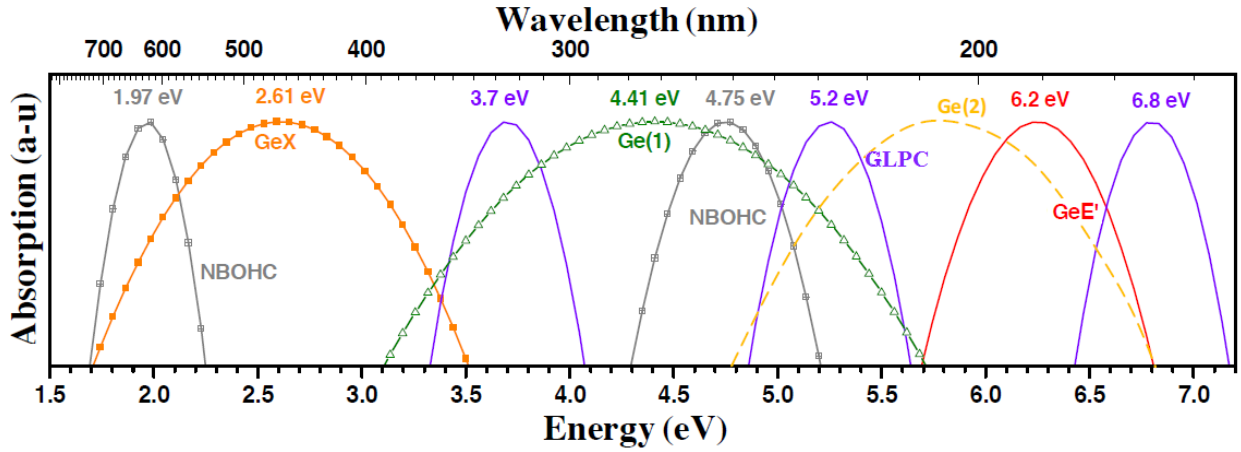

Figure 1.6: Summary of the main optical absorption bands of the Ge-related defects in semi-logarithmic plot [9].

- *compaction*, that is a fractional increase of the silica density ρ.

The radiation response of the fibers depends on several parameters [17]:

- the chemical composition and the fabrication process;
- the experimental measurement conditions, as wavelength and power of light propagating in the fiber;
- the irradiation conditions, as nature of the incident particles, accumulated dose, dose rate and temperature.

For the compaction, its dependence on the radiation dose D has been found for the silica glass [18]:

$$\frac{\Delta\rho}{\rho} \propto D^c \tag{1.3}$$

where

$$c = \begin{cases} 2/3 \text{ for } \gamma - \text{rays} \\ 1 \quad \text{for neutrons} \end{cases} \tag{1.4}$$

However, the γ-radiation induced effects depend on the glass strain and even a dilatation (negative compaction) can be observed, above all in the sample pre-compacted by other processes [19].

It is worth noting that neutron irradiation transforms the structure of silicon dioxide, both amorphous and crystalline, into a new phase, known as metamict phase, characterized by a narrower Si-O-Si angle, around 135°. As a consequence, with increasing neutron fluence, the density of amorphous silica (2.20 g/cm^3) increases, whereas that of the quartz

(2.65 g/cm^3 for the α-quartz and 2.53 g/cm^3 for the β-quartz) decreases, up to reach the same value, that of the metamict phase, around 2.25 g/cm^3, as shown in fig. 1.7.

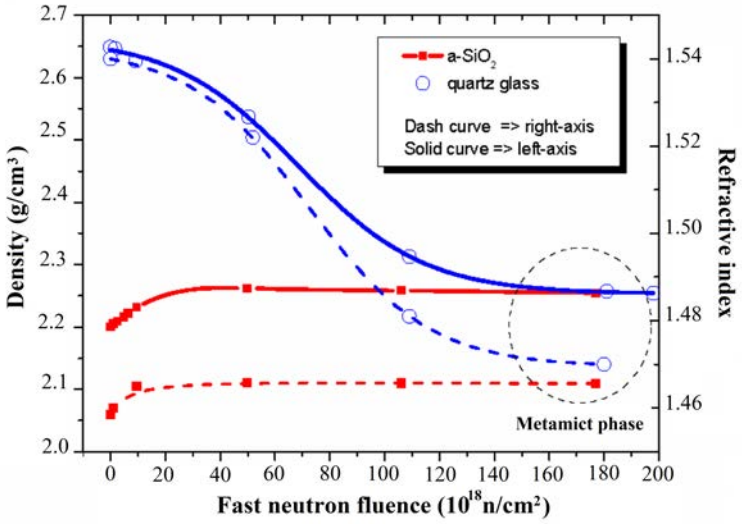

Figure 1.7: Density change and corresponding refractive index change induced by neutrons in quartz and amorphous silica [9].

Radiation induced changes in refractive index

Both the RIA and the density change cause a change in the refractive index of the glass (n) leading to different guiding properties.

- A change of the absorption ($\Delta\alpha(\lambda')$) influences the refractive index ($n(\lambda)$) through the Kramers-Kronig dispersion relation:

$$\Delta n\left(\lambda\right) = \frac{1}{2\pi^2}\int_0^\infty \frac{\Delta\alpha\left(\lambda'\right)}{1-\left(\lambda'/\lambda\right)^2}\,\mathrm{d}\lambda' \tag{1.5}$$

- The dependence of the refractive index change as a function of a change in density (ρ) and in the molar refractivity (R) can be obtained using the Lorentz-Lorenz equation [20]:

$$\Delta n = \frac{(n^2+2)\cdot(n^2-1)}{6n}\left(\frac{\Delta\rho}{\rho}+\frac{\Delta R}{R}\right) \tag{1.6}$$

1.4 Coating

The choice of the coating depends on the fiber profile of use and mainly on the application temperature. Table 1.1 reports the operational temperature range of the most common coatings.

Optical fiber coating	Operational temperature range (°C)
acrylate	-50 → 85
polymide	-190 → 350
aluminium	-269 → 400
copper	-269 → 500
gold	-269 → 700

Table 1.1: Operational temperature range of the most common coatings.

It is important to note that the coating can influence the fiber degradation, above all under neutron or proton irradiation. Fig. 1.8 displays the RIA of a pure silica fiber (KS4V) with two different coatings, subjected to both γ-rays and neutrons: a higher absorption band associate with the SiOH groups is observed in the polymer coated fiber. Its origin is linked to the neutron-induced knock-on processes: hydrogen nucleii are released from the coating and embedded into the fiber, resulting in H-related species [21].

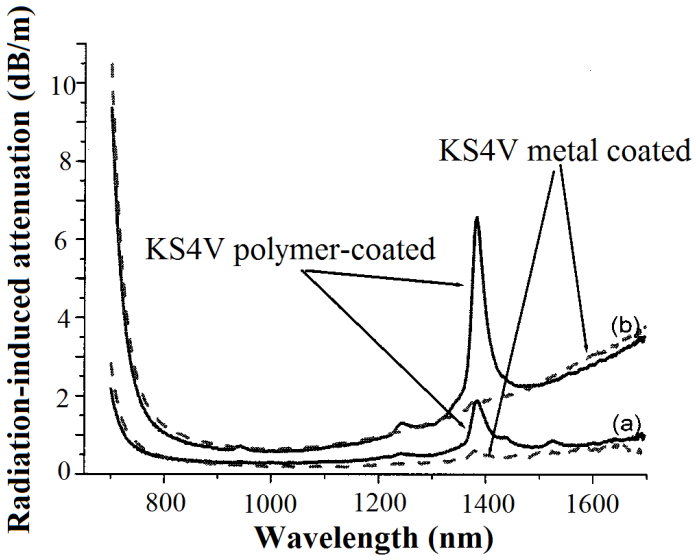

Figure 1.8: Comparison of the RIA in the infra-red region of two KS4V fibers: one metal coated (dashed line) and the other polymer coated (continuous line). The γ-doses and the neutron fluences (above 1 MeV) are: (a) 34 MGy and $1.46 \cdot 10^{17}$ n/cm^2 and (b) 150 MGy and $6.19 \cdot 10^{17}$ n/cm^2 [21].

This chapter provides an introduction to the optical fibers, the effects of radiation and the main defects of pure and germanium-doped silica.

Ce chapitre présente une introduction sur les fibres optiques et les effets des radiations ainsi que les principaux défauts de la silice pure et dopée au germanium.

In questo capitolo, è presentata un'introduzione sulle fibre ottiche e gli effetti della radiazione, insieme ai principali difetti della silice pura e drogata con germanio.

Chapter 2

Fiber Optic Temperature Sensors: advantages and limitations in radiative environments

Since the first experiments on optical fibers several research groups have focused their attention on developing this technology not only for telecommunication but also for sensing applications. In fact, the optical fiber properties depend on several parameters, as temperature, strain, pressure, refractive index of the surrounding environment, therefore they can be used as sensors. The optical fiber sensors (OFS) have all the advantages which characterize optical fibers, as small size, light weight and resistance to electromagnetic interference, as well as no need of electrical power at the sensing point and the ability to be easily multiplexed [22, 23].

All these excellent features make OFSs an interesting alternative for applications in harsh environments; however, as introduced in chapter 1, optical fibers suffer from a degradation of their properties under radiation and this influences the OFS response and compromises their use in a radiative environment.

Independently of the physical parameter to measure, sensors can be distinguished by their measurement principles: they can use a variation of the signal intensity, frequency or polarization. Generally, the frequency-based techniques are more accurate.

This chapter will deal with the fiber optic temperature sensors, their working principles and features, advantages and limitations in harsh environments, highlighted by previous studies reported in literature. In particular, we will focus our attention on:

- Blackbody Sensor;
- Distributed Sensors, that allow the temperature monitoring along all the fiber

length:

  - Rayleigh Scattering,
  - Raman Scattering,
  - Brillouin Scattering;

- Fiber Grating Sensors:
  - Fiber Bragg Grating,
  - Long Period Grating.

2.1 Blackbody sensor

The blackbody sensor is one of the oldest and it consists of a high temperature resistant optical fiber, as a sapphire fiber (working at temperature up to 2000°C), with an end covered with a thin ($\sim\mu$m) metallic film (generally made of platinum or iridium) and then with a protective film of aluminum oxide, as shown in fig. 2.1 [24].

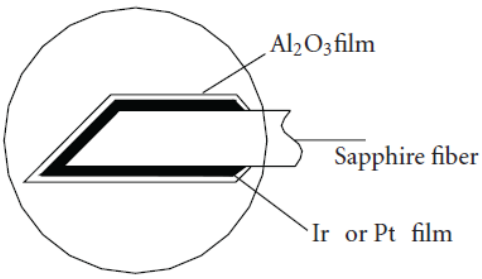

Figure 2.1: Schema of a blackbody sensor using a sapphire fiber [24].

This end realizes a quasi blackbody cavity; however, some of these sensors use the light generated directly in the fiber core, without any metallic film [25].

The emission from such a cavity at a wavelength λ is proportional to the blackbody emission and it depends on the environment temperature T, according to the Planck's law [26]:

$$W(\lambda, T) = \frac{2hc^2}{\lambda^5} \frac{1}{\exp\left(\frac{hc}{\lambda K_B T}\right) - 1} \tag{2.1}$$

By recording the signal emitted by the cavity in a spectral region, that is:

$$W(T) = \int_{\lambda_1}^{\lambda_2} W(\lambda, T)\, \mathrm{d}\lambda \tag{2.2}$$

the temperature can be determined by the ratio of the power W(T) measured at the temperature T to $W(T_0)$, recorded at a reference temperature T_0. In this way, the signal dependence on system parameters such as emissivity, that can change because of contaminations during its employment, is eliminated; however, the sensor losses sensitivity, because of dividing two nearly similar signals [24].

Moreover, the emission $W(\lambda, T)$ (Eq. 2.1) presents a maximum at a wavelength (λ_{max}) that shifts towards the blue with increasing temperature, following the Wien's displacement law:

$$\lambda_{max} \cdot T = 2.898 \cdot 10^{-3}\,\mathrm{K\ m} \tag{2.3}$$

so, the temperature can be calculated by using this property, but it is mandatory to find an easy way to determine λ_{max}.

This sensor is mainly based on intensity measurements: since a fraction of the emitted light is absorbed as it travels from the sensing tip to the detector, the fiber attenuation should be accounted for, because it decreases the signal intensity and it can also change the shape of the curve $W(\lambda, T)$.

Blackbody sensors can operate over a wide range of temperatures. However, in the low temperature region the signal intensity is very weak and this causes a degradation of the resolution [24]. The optimum measuring temperature range depends on the fiber material:

- for a sapphire fiber, the range is (500-1900)°C, because the melting point of the sapphire is 2070°C, and the temperature resolution is about 0.5°C [24];
- for a silica fiber, the range is (300-1000)°C, indeed in this range the thermal radiation is largest in the intermediate infrared region where the silica fibers do not present absorption bands, and the temperature measure is determined with a precision of about 0.05% [25].

Moreover, the measurement time depends on the small size (on the order of μm) and the heat conduction of the blackbody cavity [24] and it can be even lower than 20 ms [27].

Under radiation

This sensor was tested in a nuclear reactor, with a γ-dose rate of 18 MGy/h and a neutron flux of $5.1 \cdot 10^{14}$ n cm^{-2} s^{-1}, for 300 h irradiation time (that means an accumulated γ-dose of about 5 GGy) [25]. Under these conditions, the sensor works well only for temperatures higher than 300°C; instead, below 250°C the blackbody emission is weak and

the main component of the measured light consists of the Cerenkov emission induced by the radiation. However, both RIE and RIA have to be taken in account, as they influence the blackbody emission and the temperature measurement. The obtained precision is about 2% around 650°C.

2.2 Distributed Sensors

When a pulse light is launched into a fiber, it can be transmitted, absorbed and scattered. The scattering can be:

- elastic, if the scattered light is at the same wavelength as the incident one, for example Rayleigh scattering and Fresnel reflections;
- inelastic, if a wavelength change happens, as Raman and Brillouin scatterings.

Fig. 2.2 shows all the scattered signals.

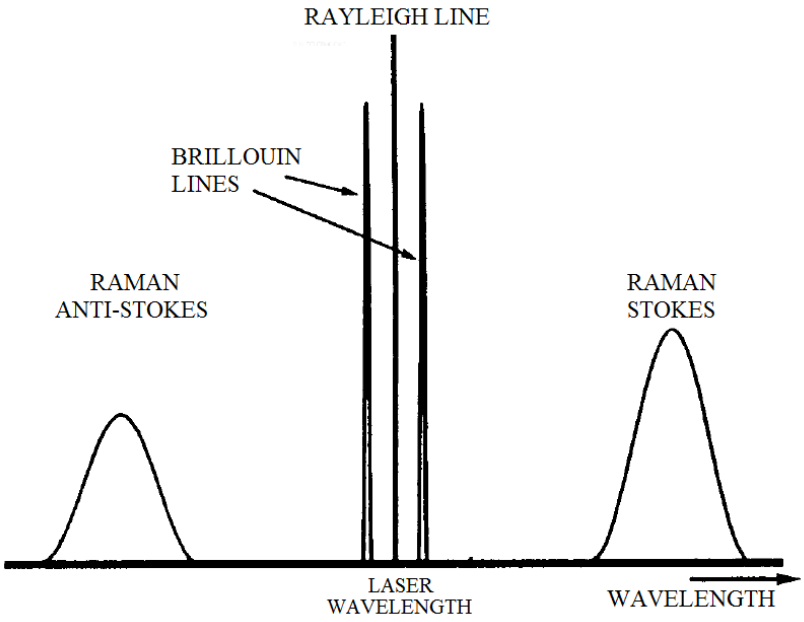

Figure 2.2: Spectrum of all the scattered signals [28].

Sensors based on the measurement of these signals are named distributed because they allow to determine the temperature all along the fiber length.

2.2.1 Rayleigh sensor

Rayleigh scattering is known as the strongest scattering that occurs in a fiber. It is an elastic scattering caused by random fluctuations in the refractive index profile, due to

variations in density or dopants concentration. For a given fiber, the scattered amplitude as a function of distance is a random but static property of the fiber: an external stimulus, as temperature or strain, causes changes in the locally reflected spectrum. Then, by comparing the Rayleigh signal profile with that recorded at a reference temperature, as room temperature (RT), the temperature changes can be estimated.

There are different techniques to measure the Rayleigh backscattered signal.

The simplest technique to measure the scattered intensity is the *Optical Time Domain Reflectometer* (OTDR) [28]: a pulsed signal is transmitted in a fiber end and the backscattered signal is recovered from the same end, as a function of position along the fiber, as shown in fig. 2.3.

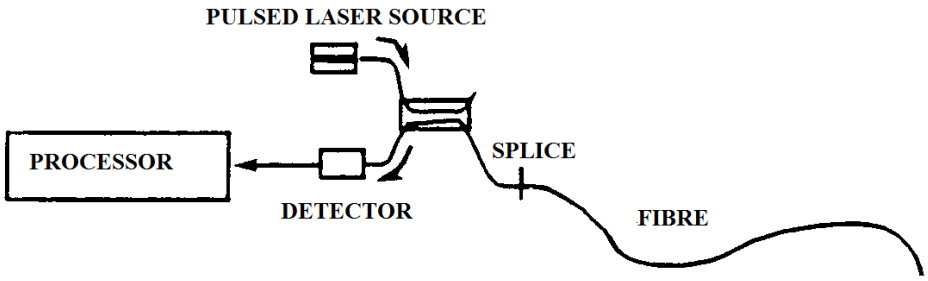

Figure 2.3: Basic optical arrangement of an OTDR [28].

The position z is obtained by the two-way propagation delay, $2t$, through the expression:

$$z = v_g \cdot t \tag{2.4}$$

where v_g is the group velocity of light in the fiber. Therefore, the spatial resolution depends on the pulse width: a 10 ns pulse implies a spatial resolution of 1 m.

The temperature sensor using the OTDR is based on intensity measurements [29]: the temperature is obtained from the ratio of the scattered intensity recorded at a reference temperature and that after heat was applied at some point along the fiber length. This ratio depends linearly on temperature in the range between RT and ∼800°C with a sensibility of about 0.015 %/°C. The temperature resolution is around 15°C. The measurement time is less than 1 minute.

Another technique often used is the *Swept Wavelength Interferometry* (SWI) [30], shown in fig. 2.4. The light of a tunable laser source (TLS) is split between the reference and measurement arms of an interferometer: while the reference light is split between the two orthogonal polarization states, the light in the measurement arm is reflected from the fiber under test (FUT); the interference between the measurement light and the two

polarization states is recorded by detectors. The analysis of these interference patterns lets obtain the complex reflection coefficient of the FUT as a function of wavelength and, finally, the Rayleigh scatter as a function of length is calculated via the Fourier transform.

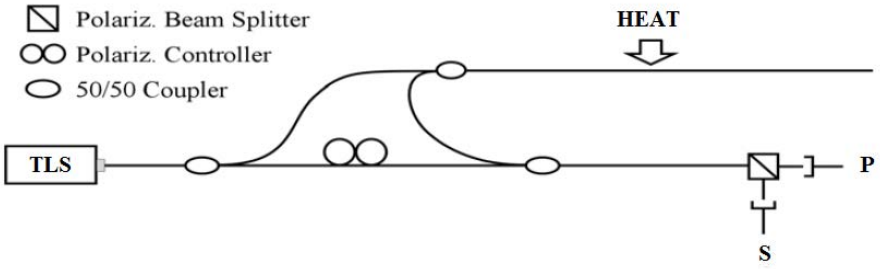

Figure 2.4: Optical arrangement of a SWI [30].

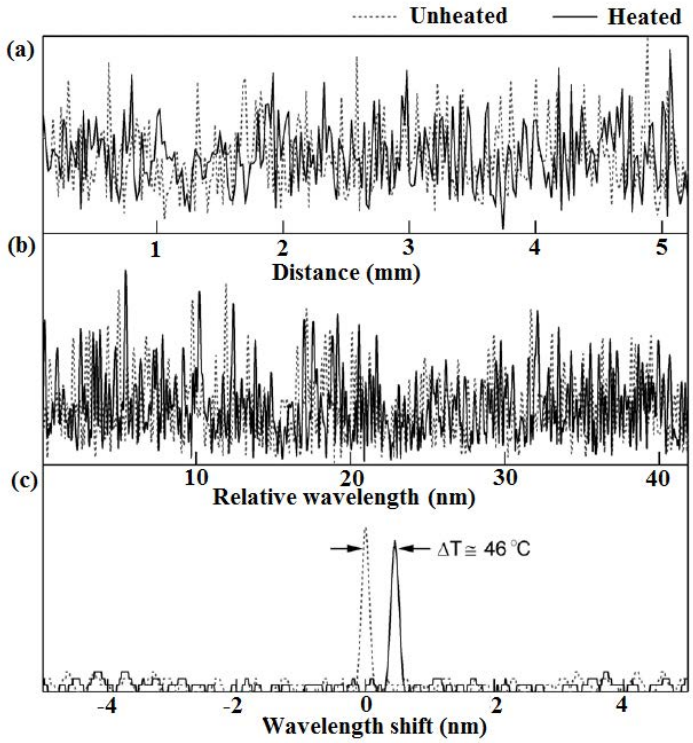

Figure 2.5: SWI as temperature sensor: (a) scatter amplitudes along a 5 mm fiber segment before and after heating; (b) corresponding wavelength spectra; (c) cross-correlation of these spectra [30].

The temperature sensor using a SWI is realized by comparing, on short fiber length Δx of order of magnitude of mm, the Rayleigh scatter signature of the FUT with that of reference, recorded at RT, as illustrated in fig. 2.5 [30]: a temperature change in one of these fiber segments induces a shift in the Rayleigh signal spectrum corresponding to that Δx (fig. 2.5(a)); the spectra are Fourier transformed in the frequency domain (fig. 2.5(b))

and finally the calculated complex cross-correlation between reference and measured data shows a peak that shifts proportionally with the temperature variation (fig. 2.5(c)).

For a sensor realized with a SWI and a standard fiber, the temperature range is from RT to ∼850°C and the sensibility, that is related to the correlation-peak shift for a temperature change, is around 10 pm/°C and it depends on the fiber composition, for example it increases with a high concentration of germanium in the fiber core. The segment Δx size corresponds to the spatial resolution and, together with the signal-noise ratio, it determines also the temperature resolution: if $\Delta x = 5$ mm, the temperature resolution is around 0.3°C, but it improves up to 0.1°C, by increasing Δx to 10 mm [30]. The measurement time is tens of seconds, for example it is 5 s for a fiber length of less than 40 m and the scan range of the laser wavelength is about 40 nm [31].

Under radiation

A Rayleigh sensor using the SWI technique was tested under a neutron flux of $1.2 \cdot 10^{13}$ n cm^{-2} s^{-1} and γ-dose-rate of 1 MGy/h: it worked well, at least for 13 hours [31].

2.2.2 Raman sensor

Raman scattering is an inelastic scattering of a photon on molecules with the creation or the annihilation of an IR phonon [32], it is illustrated in fig. 2.6 for a system having two vibrational levels of energy E_1 and E_2 (where $E_2 > E_1$). The system is excited by an incident photon of frequency ω_0 from the initial state, not necessarily the ground, to a virtual state, before coming back to another state, different from the initial one:

- if the system absorbs energy from the incident photon, the first will be in a higher vibrational level, whereas the scattered photon will have frequency ω_S lower than ω_0 (Stokes Raman scattering);
- if the emitted photon absorbs energy from the system, its final vibrational state will be lower than the initial one, whereas the scattered photon will have frequency ω_{AS} higher than ω_0 (anti-Stokes Raman scattering).

The phonon that is emitted or absorbed, respectively in the Stokes and anti-Stokes scattering, has frequency $\Delta\nu \sim 1.3 \cdot 10^{13}$ Hz for the fused silica.

The differential cross section $(\mathrm{d}\sigma/\mathrm{d}\Omega)$ for Stokes and Anti-Stokes scatterings depends differently on the temperature T [33]:

$$\frac{\mathrm{d}\sigma_S}{\mathrm{d}\Omega} \simeq \frac{{\nu_S}^4}{1 - \exp\left(-h\,\Delta\nu / K_B\,T\right)} \tag{2.5}$$

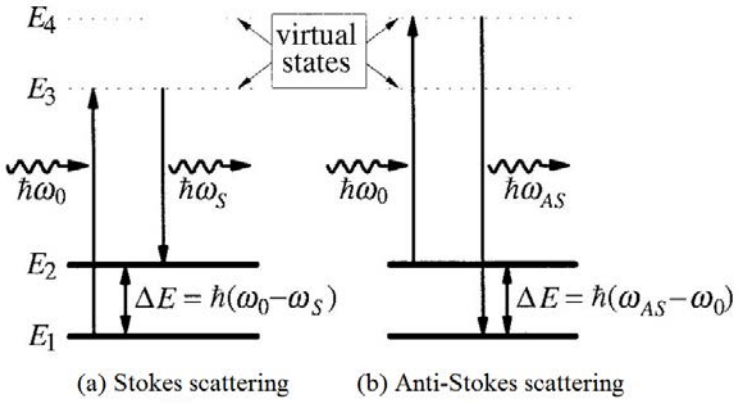

Figure 2.6: Schema of Raman scattering for a system with two vibrational levels: the arrows show the transitions induced by the absorption and the emission of photons, which are represented by waves.

$$\frac{\mathrm{d}\sigma_{AS}}{\mathrm{d}\Omega} \simeq \frac{{\nu_{AS}}^4}{\exp\left(h\,\Delta\nu/K_B\,T\right)-1} \tag{2.6}$$

As the pulses, both the laser light and the scattered signals, propagate through the fiber, they are attenuated. If P_0 is the pump power at the wavelength λ_0, the intensity of the anti-Stokes and Stokes signals scattered in a point z of the fiber can be expressed by [33]:

$$I_S(z,T) = P_0\,A_S(T)\exp\left(-\int_0^z\left(\alpha(\lambda_0,u)+\alpha(\lambda_S,u)\right)\mathrm{d}u\right) \tag{2.7}$$

$$I_{AS}(z,T) = P_0\,A_{AS}(T)\exp\left(-\int_0^z\left(\alpha(\lambda_0,u)+\alpha(\lambda_{AS},u)\right)\mathrm{d}u\right) \tag{2.8}$$

where A_S and A_{AS} are the Raman scattering cross sections, dependent on T and proportional to the differential cross sections averaged over the capture fraction. $\alpha(\lambda,u)$ is the attenuation of a point u of the fiber, at the wavelength λ.

The Raman sensor working is based on the intensity ratio of the anti-Stokes signal to the Stokes one (sometimes, the Rayleigh signal is used instead of the Stokes one) [34]:

$$R(T,z) = \frac{I_{AS}(z,T)}{I_S(z,T)} = \left(\frac{\nu_{AS}}{\nu_S}\right)^4\cdot\exp\left(-\frac{h\,\Delta\nu}{K_B\,T}\right)\exp\left(-\int_0^z\left(\alpha(\lambda_{AS},u)-\alpha(\lambda_S,u)\right)\mathrm{d}u\right) \tag{2.9}$$

This ratio is unaffected by the power fluctuations but it depends on the differential loss $\int_0^z\left(\alpha(\lambda_{AS},u)-\alpha(\lambda_S,u)\right)\mathrm{d}u$ that can be not constant with time or uniform along the fiber in harsh environments.

In absence of ionizing radiation, by neglecting the differential loss, the temperature can be easily calculated by comparing the ratio $R(T,z)$ with that recorded at a reference temperature (T_0):

$$T = \left(\frac{1}{T_0} - \frac{K_B}{h\,\Delta\nu} \cdot \ln\left(\frac{R(T)}{R(T_0)} \right) \right)^{-1} \tag{2.10}$$

However, several solutions have been already proposed to correct for the attenuation losses [33, 35].

The most used technique to measure the scattered intensity is the Optical Time Domain Reflectometer (OTDR), discussed in the previous section.

For a Raman distributed temperature sensor using an OTDR and commercial fibers [36–39], the temperature resolution can reach 0.1°C and the temperature accuracy is around ±(1-2)°C, whereas the spatial resolution is mainly governed by the laser pulse and the detector response time and it varies from 10 cm [40] to few meters; the maximum distance range is 2 km [37, 41]. The temperature range, instead, depends mainly on the fiber coating [38]: there is no example reported in literature at temperature higher than 550°C. The measurement time is closely linked to the OTDR performances: it is few seconds [41] but it can reach ∼6 min for the ultra high resolution sensor [40].

The most suitable fibers for sensors based on the Raman scattering are fibers with a large core and/or a large numerical aperture because of its larger Raman scattering efficiency [37].

Under radiation

Under radiation, as previously announced, the main cause of errors is the radiation-induced attenuation, since the Raman systems rely on optical intensity measurements. For example, an attenuation difference between the Stokes and anti-Stokes signals of 0.1 dB/km causes, at the end of 1 km long fiber, a temperature error of about 2°C if the fiber is γ-irradiated at 300°C [41] and of about 7°C when it is is γ-irradiated at 80°C [42].

Different solutions have been found to correct these errors caused by the losses:

1. Method with thermocouple data, when the radiation-induced loss distribution is uniform [43]: by measuring with two thermocouples the true values of the temperature at the two ends of the fiber and by measuring with the Raman technique the values obtained at the two ends and in a point along the fiber, the true value at this point can be extrapolated.

2. Method with loop arrangement, valid even when the losses are not uniform [43]: the fiber is arranged like a loop in order to have two parts set as close as possible so that the temperature and the radiation conditions can be assumed to be the

same; by comparing the measured intensity in two points in the first part and their corresponding in the second part, the induced loss between the two parts can be calculated and so the true value of the temperature in the second point can be obtained, if the true temperature in the first point is known.

3. Method with double ended measurement [34]: in contrast with the previous methods, the sensing fiber is probed first from one end and then the laser source is switched into the other end for a second measurement; the geometric mean of the two signals eliminates the errors linked to bending and RIA.

Single-ended arrangements can hardly perform accurate distributed temperature measurements in nuclear environments, without a compensation technique. The double-ended systems, instead, show good radiation-tolerance up to an accumulated γ-dose of 0.3 MGy [34].

2.2.3 Brillouin sensor

The Brillouin scattering is the inelastic scattering of a photon from fluctuations in the density of the medium, with emission (Stokes component) or absorption (anti-Stokes component) of a phonon, in particular an acoustic one. The frequency of the scattered light is shifted with respect to the excitation line by a quantity named Brillouin frequency and defined as [44]:

$$\nu_B = \frac{2\, n_{eff}\, v_a}{\lambda_0} \tag{2.11}$$

where n_{eff} is the the effective refractive index of the propagating mode, v_a is the speed of sound in glass ($\sim$5800 m/s) and λ_0 is the wavelength of the incident light. Generally, by exciting at 1300 nm, for a silica fiber, the Brillouin frequency ranges from 9 to 13 GHz, depending on the fiber composition and refractive index profile [45].

The Brillouin scattering can be [46]:

- spontaneous, if the amount of light scattered by thermal fluctuations is too small to excite further fluctuations in the density;
- stimulated, if the incident light (pump light) interacts with a counter-propagating light (Stokes wave), in order to create a beat pattern that causes the periodic fluctuations in the density and so an acoustic wave. The Stokes wave can be:
  - the back-scattered light from the thermal fluctuations,
  - a light injected into the opposite fiber end to that of the pump signal and having a frequency such that $\nu_{pump} - \nu_{Stokes} = \nu_B$.

The Brillouin frequency depends on temperature through the acoustic speed, determined by the temperature-depending material density ρ [44]:

$$v_a = \sqrt{\frac{K}{\rho}} \tag{2.12}$$

where K is the bulk modulus. By comparing the Brillouin scatter profile with the one recorded at RT, the Brillouin frequency shift allows to determine the temperature change along all the fiber. There are different techniques to measure the Brillouin signal, spontaneous or stimulated. In all the cases, the spatial resolution is limited to 1 m, which is equivalent to the relaxation time of an acoustic wave (∼10 ns); however, it depends on the laser pulse width.

The techniques based on the Spontaneous Scattering are the direct detection, using the BOTDR, and coherent detection.

- The *Brillouin Optical Time-Domain Reflectometry* or BOTDR, is based on the direct measurement of the Brillouin backscattered intensity and not of the Brillouin frequency, as a function of time [29]: the ratio of the scattered intensity to that recorded at a reference temperature depends linearly on temperature in the range between -30°C and ∼850°C with a sensibility of about 0.26 %/°C. The temperature resolution is around 10°C but it can be enhanced using amplification techniques [47]. The measurement time is few minutes.

- The *coherent detection* is based on a combination of optical and electronic filters [48]: the backscattered signal is mixed optically with an optical local oscillator and then amplified. The temperature sensitivity is ∼1 MHz/°C in the range from RT to ∼150°C and the temperature resolution depends on the fiber distance, from 0.5°C at 60 km to 8°C at 100 km. For the measurement time of a 100 km sensor, the theoretical time limit is around 8 min but it can reach 100 min, because of the repetition rate of the laser pulse and the acquisition system.

The most used technique is based on the Stimulated Scattering and it is the *Brillouin Optical Time-Domain Analysis* (BOTDA) [49]. It uses the interaction between a pulsed light and a continuous light counter-propagating in the fiber. By scanning one of the two frequencies, one of the beams will be amplified when the characteristic Brillouin frequency of a point and the frequencies of the two beams satisfy the condition:

$$\Delta\nu = \nu_B \tag{2.13}$$

So by monitoring the cw beam intensity, as a function of time, the Brillouin frequency of every point of the fiber can be determined and so its temperature.

For a temperature sensor based on this technique, the temperature sensitivity coefficient is ∼1 MHz/°C in the range from RT up to ∼100°C, to our knowledge, [50]. The temperature resolution is about 1°C [51], but it can enhanced up to 0.25°C with a setup that uses a single source [45]. The measurement time, generally, is few minutes, for a tens km long fiber, but it can reach few seconds, by employing pulse coding techniques [47].

Under radiation

The Brillouin sensor using the BOTDA was tested under γ-radiation: ν_B increases nonlinearly with the dose, indicating a change in the silica density, in particular a dilatation [52]. The frequency shift depends on the fiber composition: at a dose of 10 MGy, the temperature error associated with the frequency shift is only 2°C for a F-doped cladding and pure silica core fiber, whereas it increases for a Ge-doped core fiber, up to ∼18°C for a highly Ge-doped fiber ($[GeO_2] = 28\%$mol) [53]. The sensitivity does not change because of the radiation for the Ge-doped fibers, whereas a decrease of about 6% is observed for the F-doped one [53].

2.3 Fiber Grating Sensors

Fiber gratings consist of a periodic perturbation of the optical fiber properties, generally of the core refractive index, and fall into two general classifications based upon the period of the grating (Λ) [54]:

- Fiber Bragg Grating (FBG), if Λ is of the order of μm,
- Long Period Grating (LPG), if Λ is several hundreds of μm.

Their working is based on the coupling of a propagating core mode and other modes of the core or the cladding. The phase-matching condition to be satisfied is given by [55]:

$$\Delta\beta = \frac{2\pi}{\Lambda} m \tag{2.14}$$

where $\Delta\beta = \beta_1 - \beta_2$ is the difference between propagation constants of the involved modes, referred to as 1 and 2, and m is an integer number, called order. Because of this coupling, their transmission spectra show one or more attenuation peaks, whose position depends on the grating characteristics but also on temperature. So, at the basis of the Fiber Grating Sensors there is a wavelength (or frequency) measurement.

2.3.1 Fiber Bragg Grating

A Fiber Bragg Grating (FBG) couples light from a forward-propagating mode to the backward, counter-propagating mode, in the core. In this case, $\beta_2 = -\beta_1$ and $\Delta\beta = 2\beta_1$ results in a period Λ of the order of magnitude of μm [55]. The coupling occurs at a specific wavelengths, named Bragg wavelengths and defined as [56]:

$$\lambda_{Bragg} = 2 \cdot n_{eff} \cdot \Lambda/m \tag{2.15}$$

where n_{eff} is the effective refractive index of the propagating core mode and m is the order. So, the transmission or reflection spectra of a FBG show a narrow dip or peak centered at λ_{Bragg}, respectively [56].

The Bragg wavelength is a function of temperature [57]:

$$\frac{\Delta\lambda_{Bragg}}{\lambda_{Bragg}} = \frac{1}{n_{eff}}\left(\frac{\partial n_{eff}}{\partial T}\right)\Delta T + \frac{1}{\Lambda}\left(\frac{\partial \Lambda}{\partial T}\right)\Delta T \tag{2.16}$$

where the first term is the thermo-optic coefficient and the second is the thermal expansion coefficient. The temperature sensitivity depends on the fiber composition and also on the fiber coating, indeed it can be enhanced by embedding the FBG in a metal plate or by using a metal coating: the thermal expansion of the metal transfers a strain to the fiber core, which affects the period and also the refractive index because of a photo-elastic effect [58]. Generally, the sensitivity is about 10 pm/°C and the dependence of λ_{Bragg} on temperature is linear only in small range (∼100°C) around RT.

The temperature resolution depends on the temperature sensitivity and on the wavelength resolution of the Optical Spectrum Analyzer used to record the spectra: for example, it is about 0.2°C if the OSA wavelength resolution is 1 pm [58]. However, it can decrease by an order of magnitude if the information is decoded in intensity, through the use of a LPG (see next section) [59], and it can even reach ∼0.005°C with a particular sensor using more FBGs (in this case the temperature range is only 20°C) [60].

The optimum measuring temperature range depends on the fiber composition and the conditions of the grating inscription: it is between RT and ∼500°C for a standard FBG written in a standard telecommunication fiber [61], but the Regenerated Bragg gratings, that are gratings grown through thermal processing at high temperatures, can withstand higher temperature, up to ∼1000°C if the FBG is written in a silica fiber, and ∼1500°C in a sapphire fiber [62].

The measurement time is around tens of ms.

Under radiation

Among all the temperature sensors, presented here, the FBGs are the ones that have attracted more attention for the use under irradiation (see paper review [20]). The radiation can induce changes in both the refractive index (Δn_{eff}) and the period ($\Delta\Lambda$) and so a Bragg wavelength shift:

$$\frac{\Delta\lambda_{Bragg}}{\lambda_{Bragg}} = \frac{\Delta n_{eff}}{n_{eff}} + \frac{\Delta\Lambda}{\Lambda} \tag{2.17}$$

Generally, under γ-radiation, the Bragg wavelength shifts towards the red and it saturates at different values and at different accumulated doses, according to the fiber chemical composition and the conditions of the grating inscription. An exception is the N-doped silica fiber: its Bragg wavelength does not show a saturation effect, at least up to a 1.5 MGy dose [63]. The H_2-loading used to make easier the grating inscription causes a higher sensitivity to radiation.

Among the standard gratings written with UV light, the FBG that possesses the lowest radiation sensitivity is the one written in a photo-sensitive 10 mol% Ge-doped silica fiber [64]: $\Delta\lambda_{Bragg}$ saturates, with an accumulated dose of 0.1 MGy, at a level of 20 pm, corresponding to a temperature change of $\sim$2°C. Similar gratings were also tested under a mixed flux of γ-rays and neutrons for a long period: in about four years, with an accumulated γ-dose of $\sim$4 MGy and a total flux of neutrons of $\sim 10^{18}$ n/cm^2, the error on the temperature measurement is about 3°C [65].

Recent studies showed that the most resistant gratings under γ-radiation are the FBGs written in fluorine-doped fibers with the more recent technique that uses femto-second radiation at 800 nm [66]: $\Delta\lambda_{Bragg}$ saturates around 5 pm at low γ-doses, $\sim$5 kGy. However, they have been never tested yet under mixed γ-neutron radiation.

2.3.2 Long Period Grating

A Long Period Grating (LPG) contributes to couple light of a propagating core mode (the fundamental one) with discrete co-propagating cladding modes (indicated by their order n); in this case, $\beta_2 = \beta_{cl}^{(n)} > 0$ and $\Delta\beta$ is small, resulting in a period Λ of some hundreds of micrometers [55, 67]. As the cladding modes are quickly attenuated, the transmission spectrum of the grating contains a series of attenuation bands: each band corresponds to the coupling to a different cladding mode and it is centered at a wavelength defined as [67]:

$$\lambda^{(n)} = \delta n_{eff} \cdot \Lambda \tag{2.18}$$

where $\delta n_{eff} = \left(n_{eff} - n_{clad}^{(n)}\right)$ and n_{eff} and $n_{clad}^{(n)}$ are the refractive indices of the propagating core mode and of the n^{th} cladding mode.

The wavelength of the attenuation bands depends on several external parameters, such as temperature, strain and refractive index of the medium around the cladding [54,55,68]. The following expression explains the dependence on temperature, that is of our interest:

$$\frac{\Delta\lambda^{(n)}}{\lambda^{(n)}} = \frac{1}{n_{eff} - n_{clad}^{(n)}} \left(\frac{\partial n_{eff}}{\partial T} - \frac{\partial n_{clad}^{(n)}}{\partial T} \right) \Delta T + \frac{1}{\Lambda} \left(\frac{\partial \Lambda}{\partial T} \right) \Delta T \tag{2.19}$$

where the first term is the material contribution, related to the thermo-optic effect on the refractive indices of the core and the cladding, whereas the second term is the waveguide contribution depending on the period change with temperature. Generally, the relation between $\lambda^{(n)}$ and T is linear, at least in a range from RT to more than 100°C. The temperature coefficient depends on the grating period, the fiber composition and the cladding mode order. It can assume positive, negative (see reference [69] as an example of a LPG with negative sensitivity) and null values: if the sensitivity is null, the LPG is temperature insensitive. For LPGs fabricated in standard telecommunication fibers, the sensitivity varies between 0.03 nm/°C and 0.1 nm/°C, that is one order of magnitude larger than the FBG sensitivity, and it can be further enhanced by loading the germanosilicate fiber with hydrogen (0.15 nm/°C) [68] or by inscribing the LPG in special fibers: it reaches 2.75 nm/°C with a photosensitive B/Ge co-doped fiber [54].

The temperature resolution depends on the temperature coefficient and the wavelength resolution of the detector: generally, it is about 1°C, if the wavelength resolution is 0.1 nm and the sensitivity is 0.1 nm/°C, but it can improved up to 0.1 - 0.2 °C by using different techniques, based on intensity measurements [70] or modulated laser source [71].

Typically, LPGs are used in temperature range from RT to more than 200°C, but, as for all the OFSs, their good working is limited by the fiber coating material.

Under radiation

In contrast with FBGs, only few studies have been published about the radiation effects on LPGs. As for FBGs, the radiation induces a peak shift due to the refractive indices change (Δn_{eff} and $\Delta n_{clad}^{(n)}$) and to the period change ($\Delta\Lambda$):

$$\frac{\Delta\lambda^{(n)}}{\lambda^{(n)}} = \frac{\Delta n_{eff} - \Delta n_{clad}^{(n)}}{n_{eff} - n_{clad}^{(n)}} + \frac{\Delta\Lambda}{\Lambda} \tag{2.20}$$

Under γ-radiation up to the accumulated dose of 9.3 kGy (dose-rate of 6.6 Gy/s) [72], standard LPGs written in N-doped or Ge-doped fibers did not reveal any radiation induced

change, within experimental error, that is ±3 nm. Other types of LPGs show a different response under radiation.

- The turn-around-point long period grating (TAP-LPG) [73, 74] is a grating characterized by dual resonant peaks, due to coupling to higher order cladding modes. Under radiation, both peaks shift in different directions with high sensitivity and indeed they are good candidates as dosimeters. The TAP-LPGs written in a B/Ge co-doped fiber show a radiation-induced shift of more than 35 nm for each of the dips, after a γ-dose of 6 kGy, and of 80 nm after a futher exposure to a dose of 65 kGy.

- The chiral long period grating (CLPG) [75] is characterized by a periodic modulation of the optical properties of the fiber achieved by twisting the fiber as it passes through a miniature oven. The period greatly exceeds the optical wavelength so that core and cladding modes can be coupled to produce several narrow dips in the transmission spectrum. Even if their radiation sensitivity depends on the fiber composition, peak shifts of 10 nm were observed after a γ-dose of 100 kGy.

2.4 Summary of the temperature sensors and multiplexing

Table 2.1 reports briefly the main characteristics of temperature sensors based on silica fibers.

A very important property that the OFSs studied here have (except for the blackbody sensor) is their possibility to be multiplexed: a large number of sensors can be supported by a single optical fiber [76].

All the distributed sensors, based on the Rayleigh, Raman and Brillouin scatterings, are multiplexed by their nature: the fiber length can be considered as the sum of sensing elements, whose size depends on the spatial resolution. Generally, these sensors employ the time division multiplexing: the discrimination between two elements is based on the time delay between the pulse light transmission into the fiber and the backscattered signal arrival at the detector (according to the expression in Eq. 2.4).

The technique of multiplexing employed for the fiber grating sensors is the wavelength division multiplexing: several of these sensors can be written in series in the same fiber and investigated with a broadband light source. Their main limitation is their bandwidth: their peak positions have to be different and their spectral ranges of variation should

Sensor	Technique	T. range (°C)	T. sensitivity	T. resolution	Spatial resolution	measurement time
Blackbody		300 → 1000		0.05%	/	< 20 ms
Rayleigh	OTDR	RT → 800	0.015 %/°C	15°C	1 m	< 1 min
	SWI	RT → 850	10 pm/°C	0.3°C (0.1°C)	5 mm (10 mm)	∼10 s
Raman	OTDR	RT → 550		0.1°C	∼1 m	few seconds
Brillouin	BOTDR	-30 → 850	0.26 %/°C	10°C	∼1 m	few minutes
	coherent detection	RT → ∼150	1 MHz/°C	≥ 0.5°C		> 8 min
	BOTDA	RT → ∼100	1 MHz/°C	1°C		few minutes
FBG		RT → < 1000°C	10 pm/°C	0.2°C	/	∼10 ms
LPG		RT → > 200°C	(0.03 - 3) nm/°C	∼1°C	/	∼10 ms

Table 2.1: Summary of the main characteristics of the fiber optic temperature sensors.

not overlap. It is possible to multiplex about 15 gratings in a fiber, without increasing excessively the measurement time.

2.5 Development of a temperature sensor in a recent nuclear reactor: the SFR

In comparison with all the other radiative environments, the nuclear reactor is characterized by the highest γ-rays dose, as well as by a neutron flux. Nowadays, the operational reactors are II or III generation systems, whereas most of the I-generation has been already retired. The IV generation rectors are the last field the research is working on, to make them more economical and safer and to minimize the waste. These reactors can be distinguished in fast and thermal, depending on the used neutrons.

The French group AREVA, with CEA and EDF, is working on the Sodium-cooled Fast Reactor (or SFR) technology [77], whose schema is shown in fig. 2.7.

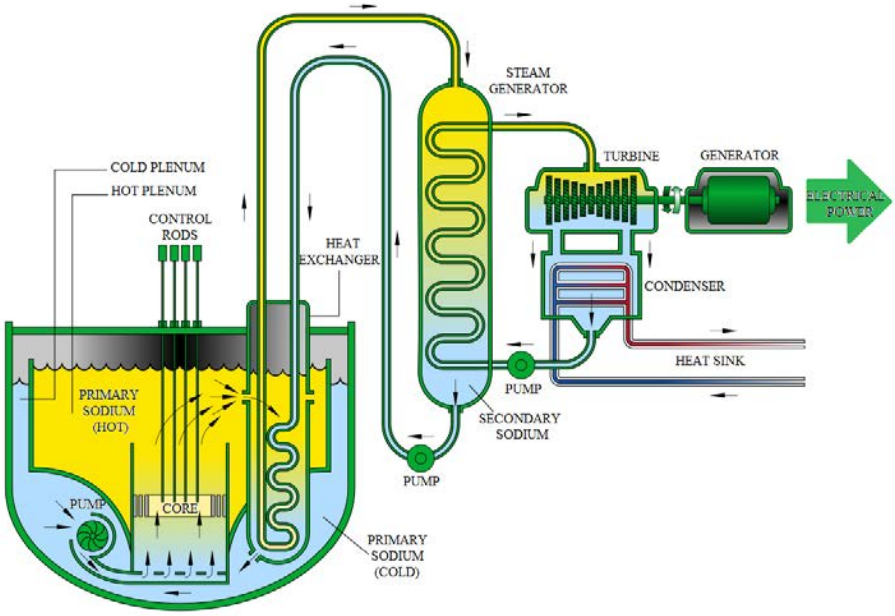

Figure 2.7: Schema of a Sodium-cooled Fast Reactor (or SFR) [77].

The SFR reactor is fueled by a metallic alloy of uranium and plutonium and cooled by liquid sodium. It allows to increase the efficiency of uranium usage by breeding plutonium, so the reactor can work for a long period (about 2 years) without any external operation. The liquid sodium has a high heat capacity, it does not slow down the fast neutrons into thermal neutrons, as water does, and it allows the system to work at atmospheric pressure, since its boiling point, at 883°C at atmospheric pressure, is much higher

than the reactor operating temperature. Indeed, in comparison with other reactors, the temperature is not particularly high: it is generally around 550°C (hot sodium plenum) during the reactor operation and it is only 180°C during the maintenance and the outage. The pressure in the primary circuit is much lower than in pressurized reactors (around 4 bars).

Regarding the radiation dose, that is higher near the core than in the rest of the reactor, for the SFR the γ-dose rate is 10 kGy/h and the neutron flux is $2 \cdot 10^{11}$ n cm^{-2} s^{-1}; if the maintenance is realized each two years, the accumulated γ-dose is around 175 MGy and the neutron fluence is about $1.3 \cdot 10^{19}$ n cm^{-2}.

A temperature sensor to be used in the very harsh environment near the SFR core should have all the characteristics reported in table 2.2, not only to work inside the reactor but also to be able to follow rapid temperature changes. Even if the operation temperature limit is only 600°C, the sensor should withstand temperatures up to 750°C, that can be reached in accidental conditions.

Operational range	(120 - 600)°C
Tolerance max	±1.5°C
Temperature resolution	< 0.5°C
Measurement time response	0.5 s

Table 2.2: Measuring characteristics of the temperature sensors.

The comparison between the characteristics of all the temperature sensors, reported in table 2.1, and of the ideal one leads to the conclusion that the sensor that best suits the Areva application seems to be the Fiber Bragg Grating.

To summarize, among all the OFSs, the FBG seems to be the most suitable temperature sensor to work for two years at about 550°C, under a mixed radiation up to a γ-dose of $\sim$175 MGy and a neutron fluence of $\sim 1.3 \cdot 10^{19}$ n cm^{-2}, with a temperature resolution lower than 0.5°C and a measuring time response of 0.5 s. In this thesis, the potential of this technology in terms of radiation hardness will be investigated with the following irradiation characteristics as a first preliminary work:
γ-dose $\approx$ 4 MGy, irradiation temperature $\approx$ 300°C.

En résumé, l'étude bibliographique sur les diffrents capteurs à fibre optique a montré que le capteur de température à réseau de Bragg est celui qui présente le potentiel le plus élevé pour travailler pendant deux ans à environ 550°C, sous un rayonnement mixte jusqu'à une dose de radiation gamma de ∼175 MGy et une fluence de neutrons de $\sim 1.3 \cdot 10^{19}$ n cm^{-2}, avec une résolution de température inférieure à 0.5°C et un temps de réponse permettant une mesure chaque 0.5 s. Dans cette thèse, le potentiel de cette technologie en termes de durcissement sera étudié avec les caractéristiques ci-après comme un premier objectif :
dose $\gamma \approx 4$ MGy, température de fonctionnement ≈ 300°C.

Fra i sensori a fibre ottiche (OFS) studiati in letteratura, il FBG sembra essere il più adatto a lavorare per due anni a circa 550°C sotto irraggiamento, fino a una dose gamma di ∼175 MGy e un flusso totale di neutroni di $\sim 1.3 \cdot 10^{19}$ n cm^{-2}, con una risoluzione di temperatura inferiore a 0.5°C e un tempo di risposta di 0.5 s. In questa tesi, il potenziale di questa tecnologia in termini di resistenza alle radiazioni saranno studiati preliminarmente con le seguenti caratteristiche d'irraggiamento:
dose $\gamma \approx 4$ MGy, temperatura di irraggiamento ≈ 300°C.

Chapter 3

Fiber Bragg Gratings

In the previous chapter the radiation effects on the fiber optic temperature sensors were reported. As the FBG was chosen as a good candidate for the applicative aim studied in this thesis, further attention has to be given to this sensor. This chapter is focused on the temperature and radiation limitations of the different types of FBGs. Because of the wide literature on the temperature effects on Bragg gratings, only few works will be cited here. A particular type of gratings will be neglected: the Chemical Composition Fiber Grating. It is generally very stable at high temperatures but not at all under mixed γ-neutron radiation [78].

3.1 A little of theory

A Fiber Bragg Grating [56, 79, 80] consists of a periodic modulation of the refractive index in the fiber core formed by its exposure to an intense light interference pattern. At each index variation a small amount of light guided along the fiber core is reflected and all the reflections add coherently at a well determined wavelengths, called Bragg wavelengths and defined in Eq. 2.15. So, a FBG is a wavelength selective filter, which acts as a pass-band in reflection and as a rejection band in transmission. In the following, only gratings written in single-mode fibers will be presented. However, it is worth noting that Bragg gratings can also be written in multi-mode fibers, depending on the aimed applications [81].

Several theoretical works have been trying to determine the optical properties of gratings, depending on:

- magnitude of effective refractive index (n_{eff}),
- period of the refractive index perturbation (Λ),

- grating length (L),
- number of grating periods (N), defined as L/Λ,
- refractive index modulation amplitude (Δn^{mod}), defined as the difference between the refractive index of the zones illuminated and not,
- modal overlap factor (η), which defines the amount of the power guided by the core and can be calculated as [82]:

$$\eta = \frac{\pi^2 \phi_{core}^2 NA^2}{\lambda^2 + \pi^2 \phi_{core}^2 NA^2} \tag{3.1}$$

  where ϕ_{core} is the core diameter.

From the well-known *coupled-mode theory*, the reflectivity (R) of uniform gratings, as a function of wavelength, can be expressed as [83, 84]:

$$R = \frac{\sinh^2\left(\kappa L\sqrt{1-\left(\frac{\delta}{\kappa}\right)^2}\right)}{\left(1-\left(\frac{\delta}{\kappa}\right)^2\right)\cosh^2\left(\kappa L\sqrt{1-\left(\frac{\delta}{\kappa}\right)^2}\right)+\left(\frac{\delta}{\kappa}\right)^2\sinh^2\left(\kappa L\sqrt{1-\left(\frac{\delta}{\kappa}\right)^2}\right)} \tag{3.2}$$

where $\kappa = \pi/\lambda_{Bragg} \cdot \eta \cdot \Delta n^{mod}$ is known as the coupling coefficient, $\delta = \frac{2\pi n_{eff}}{\lambda} - \frac{\pi}{\Lambda}$ and δ/κ is the detuning ratio, depending on λ/λ_{Bragg}. Fig. 3.1 shows, as example, the profile obtained for an uniform grating with $\kappa L = 2$.
The maximum value of R occurs at λ_{Bragg} (i.e. $\delta = 0$) and is [85]:

$$R_{max} = \mathrm{tgh}^2(\kappa L) \tag{3.3}$$

Another important parameter is the grating width, in particular the full width, defined as the distance between the first two minima, is given by [85]:

$$width = \lambda_{Bragg}\sqrt{\left(\frac{\Delta n^{mod}}{n_{eff}}\right)^2 + \left(\frac{\lambda_{Bragg}}{n_{eff}L}\right)^2} \tag{3.4}$$

In the weak grating case $\left(\Delta n^{mod} << \frac{\lambda_{Bragg}}{L}\right)$, the filter bandwidth is limited by the FBG length, whereas in the strong grating case $\left(\Delta n^{mod} >> \frac{\lambda_{Bragg}}{L}\right)$, the light does not penetrate the full length of the grating and the bandwidth is dependent only on the refractive index modulation amplitude.

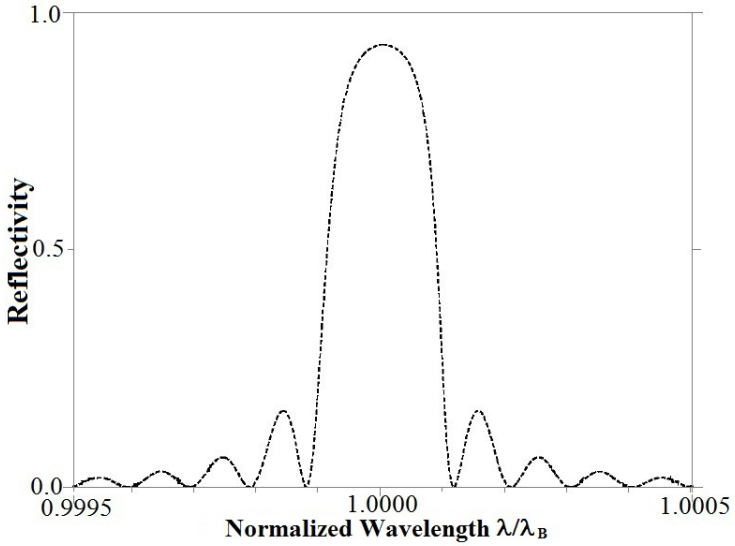

Figure 3.1: Reflection spectrum versus normalized wavelength for an uniform Bragg grating with $\kappa L = 2$ [85].

FBG as a sensor

The FBG response is sensitive to environmental factors; indeed, any change which varies the refractive index or grating period, such as strain and temperature, will change the Bragg wavelength, making the grating a very good intrinsic sensor, with the information wavelength-encoded and independent of the signal intensity [56].

When a force ΔF is applied to the grating [57],

$$\frac{\Delta\lambda_{Bragg}}{\lambda_{Bragg}} = \left(1 + \frac{1}{n_{eff}}\frac{\partial n_{eff}}{\partial S}\right)\left(\frac{1}{\Lambda}\frac{\partial\Lambda}{\partial F}\right)\Delta F \tag{3.5}$$

where S is the strain. The strain response is linear with no evidence of hysteresis; a typical value for the sensitivity to an applied axial strain is 1 nm/millistrain, for a grating at 1300 nm [56].

A temperature change ΔT causes a shift [57]:

$$\frac{\Delta\lambda_{Bragg}}{\lambda_{Bragg}} = \frac{1}{n_{eff}}\left(\frac{\partial n_{eff}}{\partial T}\right)\Delta T + \frac{1}{\Lambda}\left(\frac{\partial\Lambda}{\partial T}\right)\Delta T \tag{3.6}$$

where:

- $\frac{\partial n_{eff}}{\partial T}$ is the thermo-optic coefficient, about $10^{-5}/°\mathrm{C}$ [86],
- $\frac{1}{\Lambda}\left(\frac{\partial\Lambda}{\partial T}\right)$ is the thermal expansion coefficient, about $0.5 \cdot 10^{-6}/°\mathrm{C}$ at RT [23].

A typical value of the temperature coefficient of a bare grating at 1550 nm is about 0.01 nm/°C and it is primarily due to the thermo-optic effect [57]. However, it depends strongly on the fiber coating, particularly on its material and thickness, indeed it increases by increasing the coating thickness with a saturating trend [87]. The temperature sensitivity also decreases if the grating peak is at shorter wavelengths [88]. The FBG temperature response is not linear over a wide range and there is hysteresis [57]: this issue will be discussed later.

3.2 Grating fabrication techniques

Since 1978, when for the first time a FBG was observed by Hill and al. [57], several techniques have been developed for the grating fabrication. This section deals with the principles of the different techniques, holographic (internal, transverse writing and phase mask) and non (point by point). For short pulse lasers, such as femtosecond systems, interferometric setups are nontrivial to align, since path lengths need to be matched to within the spatial location of the pulse, for example within 36 μm for a 120 fs beam [89].

Internal writing (Hill 1978)

The fiber core is exposed to coherent contra-directional beams, which originate an interference pattern and so the refractive index periodic structure. A laser beam at 488 nm is injected in a photosensitive fiber end and partially back-reflected at the other end, initially only because of the Fresnel reflection (4%); the interference between these beams start to originate the grating, increasing the back-reflected signal and making easier the grating writing [57]. The Bragg wavelength coincides with that of the laser used for the inscription, i.e. $\lambda_{Bragg} = \lambda_{laser}$. Therefore, to change λ_{Bragg}, it is necessary to have a laser source at the chosen wavelength. Moreover, the grating length is the all fiber length, because it is all exposed to the laser light.

Transverse holographic technique (Meltz 1989)

This method was the first consisting of exposing the fiber core to a two beams interference pattern from a side of the fiber. The UV light is split into two equal-intensity beams and then recombined to produce an interference pattern, normal to the fiber axis, focused within the core of the bare photosensitive fiber [90]. The grating period, and then λ_{Bragg}, depends on the laser wavelength and the angle between the beams.

Point by point (Malo 1993)

In this technique, briefly referred to as PbP, each grating fringe is produced one after the other [91]: the laser light is focused in a point of the core, increasing locally the refractive index, then either the fiber or the laser beam is translated through a distance corresponding to the grating period Λ, in parallel direction to the fiber axis; this process is repeated N times, until all the grating length, $L = N\Lambda$, is written. The laser spot determines the dimension of the illuminated zones.

Phase mask technique (Hill 1993)

The basis of this technique is the phase-mask grating (PM), an one-dimensional surface relief structure fabricated in a material transparent to the laser radiation. When it is placed between the light source and the optical fiber, the beam passes through it at normal incidence and originates an interference pattern [92]. The grating period is half that of the phase mask and is independent on the laser wavelength. As this technique was used to fabricate our gratings, more details will be presented in the following chapter.

3.3 Types of Gratings

The gratings can be distinguished according to the laser source used for their writing: the UV laser can be pulsed or continuous wave, whereas the IR source has to be ultrashort pulsed, because the phenomena originating the gratings can only be multi-photons, due to the small energy of the IR photons.

3.3.1 UV-FBGs

The phenomenon behind the UV-FBG formation is the photo-sensitivity of silica doped with specific elements, primarily the germanium.

In the past decades, gratings were written with all types of lasers, continuous wave or pulsed, emitting light at different wavelengths. The use of high pulse energy laser was proposed for the first time by Askins et al. [93], to reduce the writing time down to few tens of nanoseconds, the duration of a single pulse.

Nowadays, the most commonly used light sources are KrF and ArF excimer lasers emitting, respectively, 248 and 193 nm pulses with a duration of $\sim$10 ns at repetition rates of 50-75 Hz. The exposure of a Ge-doped fiber to UV light for few minutes at intensities of 100-1000 mJ/cm^2 causes an increase of the refractive index ranging between 10^{-5} and 10^{-3} but it can reach 10^{-2} by loading the fiber with H_2 [56].

During inscription n_{eff} and Δn^{mod} increase, indeed the peak position shifts towards longer wavelengths, while the peak width and reflectivity increase [94]. It was observed that [94]:

1. the laser repetition rate does not influence much the reflectivity, that becomes slightly higher as the laser repetition increases by a factor 10, without degrading the spectra quality;

2. R increases with increasing fluence, at constant total exposure dose;

3. at each fluence, R shows a saturating tendency as a function of writing time, but the maximum R value and the total dose at which the saturation is reached increase with the exposure fluence.

The relation between Δn^{mod} and the incident fluence (I) depends on the excitation photon energy. For the gratings writing with an ArF excimer laser, Malo et al. found a dependence of the growth rate on I^2, indicating a two-photon process, in which the carriers are generated by direct excitation in the silica bandgap and then they are trapped at Ge-related defects [95].

The thermal stability of gratings depends on the fiber composition and the inscription conditions but, generally, they do not withstand 600°C. This is related to the defects originating Δn^{mod}: studies about the fluence dependence of the Ge-related defects and Δn^{mod} and their thermal stability showed that the grating formation is mainly associated with the generation of GeE′ and GeH centers and indeed it is the much higher formation efficiency of these centers that gives rise to the much higher photosensitivity of H_2-loaded fibers [61].

Type II FBGs

By increasing the pulse energy beyond a threshold value the induced refractive index modulation does not grow anymore linearly with the pulse energy but increases very quickly up to saturate around $5 \cdot 10^{-3}$. The gratings written in this regime are labeled as type II FBGs, to distinguish from the previous, called type I gratings [96]. They exhibit high reflectivity and large bandwidth and they withstand temperatures up to 800°C: they decay quite slowly at 900°C, whereas at 1000°C a treatment of few hours is sufficient to make them disappear. However, their use is limited by their poor quality spectra.

Studies with optical microscope show that laser damage, responsible for the index change, is limited to the core-cladding interface [96].

Type IA FBGs

Type IA FBGs are regenerated gratings written in hydrogenated Ge-doped or B/Ge co-doped optical fibers after a prolonged UV exposure. During inscription they exhibit a large red-shift of the central wavelength, that means a large increase in the mean refractive index of the core [97]. This red-shift occurs in three phases [98]: an initially rapid increase of the Bragg wavelength, followed by a slower growth up to reach a plateau at a saturation value that depends on fiber type, hydrogenation and irradiation conditions. Typically, $\Delta\lambda_{Bragg}$ is around 20 pm and entails $\Delta n_{eff} \sim 2 \cdot 10^{-2}$ [97,98]. With increasing laser intensity, the grating formation is more rapid but the stabilization λ_{Bragg} value is lower [98].

Type IA gratings show lower temperature stability than type I [99]. Moreover, they exhibit also the lowest thermal sensitivity of all the FBG types [97,99], whereas the strain response does not change particularly [99].

Type IIA FBGs

Type IIA FBGs are also called negative index gratings, because the UV light induced refractive index change is negative [100]. Their inscription is characterized by a non-monotonic evolution in both modulation and effective index, with three phases. Initially, n_{eff} and Δn^{mod} increase and a type I grating is written. Then, by increasing the accumulated laser energy [101] or by subjecting the grating to a thermal treatment at high temperature, as 700°C, [102] the type I grating is erased and n_{eff} and Δn^{mod} decrease, until the starting point of the regeneration process is reached: Δn^{mod} starts to increase again, while n_{eff} decreases, implying the blue-shift of the initial central wavelength. Physically, the type I regime is based on the exhaust of pre-existing precursors, while the type IIA regime on the formation of UV-induced structural changes, such as compaction or core-cladding stress relaxation [100, 101]. These gratings are written in highly Ge-doped, B/Ge or Sn/Ge co-doped fibers, with or without H_2-loading [101].

Type IIA gratings exhibit a better stability at high temperatures than type I [100]. If as example is considered a type IIA FBG written in an unloaded highly Ge-doped fiber and pre-annealed at 700°C for two days, a thermal treatment at 1000°C causes the reduction of $2.5 \cdot 10^{-3}$% reflectivity and 1 pm wavelength shift per hour; however, it is the pre-treatment at 700°C that strongly affects the Bragg peak [102].

Type IIA gratings can be written also by UV femtosecond laser, as observed by Violakis et al. [103]: they show similar features to the other type IIA gratings but enhanced thermal stability.

3.3.2 IR fs-FBGs

This section will deal with FBGs made with 800 nm femtosecond radiation.

The grating formation is characterized by a threshold for the pulse peak intensity, which depends on:

- the temporal and spatial qualities of the laser light and the accuracy of the alignment of the incident beam onto the fiber core [104];
- the fiber dopants: with the PM technique, the threshold is about $3 \cdot 10^{13}$ W/cm^2 for all-silica core fibers [105], as for observing fs-induced modifications in silica bulk [106], but it decreases down to $2 \cdot 10^{13}$ W/cm^2 for Ge-doped core fibers [105];
- the used technique: the threshold for a Ge-doped fiber is one order of magnitude higher with the PbP technique than with the phase mask [105, 107];
- the H_2-loading, which reduces the threshold but only in the Ge-doped fibers and not in the all-silica core fibers [105, 108].

Above this peak intensity threshold, a grating will be written, but increasing the peak intensity two regimes of induced index change are observed: in analogy with the UV-FBGs, the two types gratings are referred to as type I-IR and type II-IR [109].

Type I-IR FBGs

Type I-IR FBGs can be made with multiple-pulse exposures: the reflectivity shows a linear growth with the number of incident pulses, indicating that Δn^{mod} does not saturate, while the Bragg peak shifts towards longer wavelengths with a saturating tendency [89, 104]. Fig. 3.2 shows, as example, the variations of R and λ_{Bragg} with the number of incident IR pulses (having energy of 300 μJ) in a standard Ge-doped Corning SMF-28 fiber: after 15000 pulses, λ_{Bragg} shifts by about 0.2 nm, corresponding to Δn_{eff} of $1.8 \cdot 10^{-4}$ [89].

One of the most important features of IR gratings is that the refractive index modulation amplitude is one order of magnitude larger than the average index change [89].

Type I-IR FBGs show similar annealing properties to type I-UV gratings of comparable strength, as shown in fig. 3.3. Consequently, the mechanism for fabrication of type I-IR gratings may result from color center formation, induced from multi-photon absorption processes, as demonstrated by Smelser et al. [105] with a study about the growth of the index modulation as a function of interference field intensity.

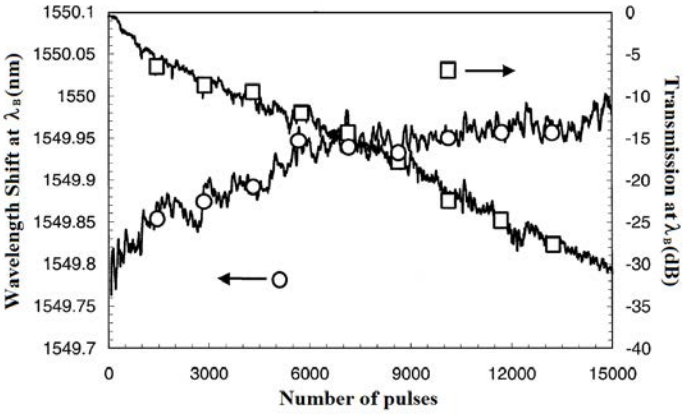

Figure 3.2: Variations of reflectivity and peak wavelength with the number of incident IR pulses (with energy of 300 μJ/pulse) in a standard Ge-doped Corning SMF-28 fiber [89].

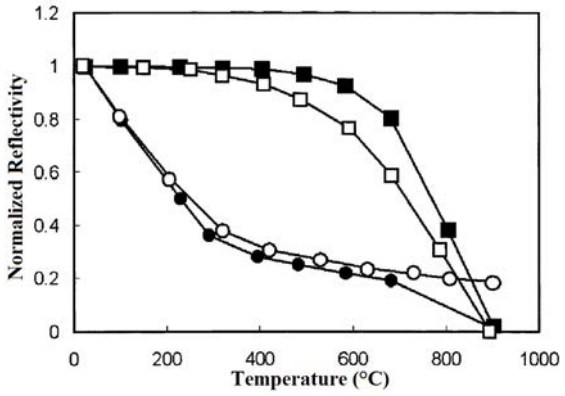

Figure 3.3: Annealing for fs IR (filled circles and squares) and cw UV (open circles and squares) gratings: the lower annealing curves are referred to gratings with an initial Δn^{mod} of 10^{-5}, whereas the upper curves are referred to gratings with an initial Δn^{mod} of 10^{-3} [105].

Type II-IR FBGs

In a Ge-doped fiber, a type I-IR grating is written with a pulse peak intensity of $2 \cdot 10^{13}$ W/cm^2, whereas for intensity above $\sim 5 \cdot 10^{13}$ W/cm^2 a type II-IR grating is obtained [109]. These FBGs are characterized by several differences with respect to the type I:

- the growth rate is more rapid [109];
- the bandwidth increases, likely resulting by a reduction in the effective grating length, because, where the laser beam profile tapers to zero, the peak intensity is not above the threshold and grating lines can miss [109];
- the reflection spectra have lower quality, resulting from the strong coupling into the

cladding modes due to the non-uniform refractive index change across the core [109]: the H_2-loading improves the spectra quality, probably because of the enhanced photosensitivity of the fiber core and the lower laser intensity employed [108].

The most important difference lies in the annealing behavior of these gratings: they show the same thermal stability of type II UV-induced damage gratings. For example, a 16 h annealing at 950°C stabilizes the fs-FBG written in a Ge-doped fiber at ∼75% of the initial strength [104]. However, the grating behavior under thermal treatment depends on the grating itself, that is its writing parameters and history. Some authors, as Marshall et al. with the PbP technique [107] or Smelser et al. with the phase-mask technique [109], noticed a slight increase of the strength as the annealing temperature increases up to 1000°C. This increase may be a result of two kinds of index change. In the peaks of the interference pattern, enough intensity exists to ionize the fiber glass producing an index change durable with temperature. In the valleys of the interference pattern the peak intensity is below the type II-IR threshold and only type I-IR index changes may occur. During the thermal treatment the annealable type I-IR component is erased, while the permanent type II-IR component remains fixed. This causes an increase of Δn^{mod}. When the annealing temperature exceeds 1000°C, the gratings are gradually erased, more rapidly in fibers loaded with H_2 than in the unloaded ones [108].

Moreover, Grobnic et al. [110] studied the Bragg wavelength behavior under temperature cycling. For a grating written in a Ge-doped fiber no hysteresis for cycles at 1000°C was observed, whereas around 1040°C the Bragg peak becomes unstable and starts drifting towards longer wavelengths at a rate depending on the annealing temperature and the grating history. Instead, for a grating written in an all-silica core fiber the peak shift was observed towards longer wavelength during a treatment at 1060°C, but towards shorter wavelengths at 1000°C. In conclusion, the shift rate and its direction depend on the grating history and on the annealing temperature. Neglecting the contribution of the variation of Λ with the temperature to the Bragg drift, a reduction in n_{eff} due to a reduction in Δn^{mod} can explain only a blue-shift. The red-shift can be attributed to an irreversible change in the unperturbed refractive index of the core and the cladding. An increase of the core index of an all-silica core fiber was observed through thermal relaxation of residual stress under treatments at 900°C [111].

3.4 Grating stability

The possibility of using FBGs in real applications depends strongly on their effective lifetime, above all for applications at high temperatures. The grating thermal degradation

manifests itself with a reduction in the peak reflectivity and bandwidth: during a treatment the decay is rapid at first and followed by a decreasing rate decay.

Erdogan et al. [112] proposed a model to explain this degradation: if R is the grating reflectance, the integrated coupling coefficient (ICC), defined as

$$ICC = \text{tgh}^{-1}\left(R^{1/2}\right) \tag{3.7}$$

is proportional to Δn^{mod} and, if normalized to the value assumed before the treatment start (ICC_0), it follows a power law as a function of duration t of the thermal treatment at temperature T:

$$\frac{ICC}{ICC_0} = \frac{1}{1 + A \cdot (t/t')^B} \tag{3.8}$$

where t is expressed in minutes and t' is 1 min, in order to have all the parameters dimensionless. A plotted on logarithmic scale varies linearly with temperature in K:

$$A = A_0 \cdot \exp(aT) \tag{3.9}$$

and B varies linearly with temperature in K, passing through zero at 0 K:

$$B = T/T_0 \tag{3.10}$$

This approach assumes that the grating inscription causes a broad distribution of the activation energy of thermodynamically unstable traps and the thermal treatment releases electrons involved in the traps with energy lower than the demarcation energy, defined as

$$E_d = K_B T \cdot \ln(\nu t) \tag{3.11}$$

where K_B is Boltzmann's constant and ν is a frequency that has to be calculated from data and is about 10^{13} Hz for H_2-free Ge-doped FBGs [113]. The E_d distribution is bell-shaped with the peak at $\Delta E \approx -K_B T_0 \cdot \ln(A_0)$ and FWHM of about $3K_B T_0$.

Erdogan's model does not apply for gratings made of hydrogenated fibers, because these gratings have a broader distribution of activation states, that extends to low energy, so treatments at low temperature, around 100°C, are enough to start the detrapping process and the decay is rapid. Baker et al. proposed a new model for these gratings, known as 'log time model' [114], according to which the normalized ICC as a function of t can be expressed as:

$$\frac{ICC}{ICC_0} = \begin{cases} 1 - C \cdot \log\left(\frac{t}{\tau}\right) & \text{for } t > \tau \\ 1 & \text{for } t < \tau \end{cases} \tag{3.12}$$

where C is a constant and τ depends on the temperature according to the Arrhenius relation:

$$\tau = A \cdot \exp\left(\frac{E_a}{R \cdot T}\right) \tag{3.13}$$

where R is the universal constant.

To stabilize a FBG in order to obtain stable performances over an operating time t_O at the temperature T_O, after inscription it has to undergo to an annealing at a temperature T_A, higher than T_O, with duration t_A defined as [114]:

$$t_A = \begin{cases} \exp\left[aT_0\left(\frac{T_A}{T_O} - 1\right)\right] t_A^{T_A/T_O} & \text{for the Erdogan model} \\ \\ t_O\left(\frac{\tau_A}{\tau_O}\right) & \text{for the log time model} \end{cases} \tag{3.14}$$

where all the parameters are related to the data fit.

3.5 Effects of γ-radiation

This section will deal with the radiation effects on the grating types reported in section 3.3.

3.5.1 UV-FBGs

As already said, gratings can be written with UV lasers only in photosensitive fibers. As radiation induces losses in fiber transmission, it is preferable to splice small lengths of photosensitive fibers, including Bragg gratings, with radiation-resistant fibers, in order to reduce the total induced losses and to keep an acceptable signal-noise ratio [115].

The radiation influences the position, amplitude and FWHM of the Bragg peak, depending on the grating parameters and the writing conditions as well as the used fiber.

In most of cases, the radiation causes a Bragg wavelength shift (hereafter referred to as BWS) *towards longer wavelengths* with a saturating tendency. This red-shift means an increase of the average effective index n_{eff} and, as a consequence of the Kramers-Krönig relations (Eq. 1.5), an increase of absorption at wavelengths shorter than the Bragg one [116]. For example, for the germanosilicate fibers, as demonstrated by Neustruev et al. [117], the γ-irradiation creates the same paramagnetic defects, Ge(1), Ge(2) and GeE′, as the UV-light does. Moreover, the γ-radiation should affect only the mean value of n_{eff} and not the modulation amplitude Δn^{mod} [64]. The saturating behavior can result from two reasons [118]: one is the limited concentration of precursor defects responsible for the refractive index change and the other is the competition between defect generation

and annealing [119]. In the first case, the saturation level is independent of the dose-rate, whereas in the latter case it depends on the radiation dose-rate and the annealing rate.

The BWS depends mainly on the chemical composition of the fiber and the photosensitization technique used for writing FBGs.

As demonstrated by Henschel et al. [120], it is not possible to determine the influence of the fiber composition on the BWS. As example, fig. 3.4 shows the BWS of gratings made of several fibers doped with different elements, as germanium, boron, phosphorous, cerium and nitrogen, to make the fiber core photosensitive. Despite the fiber composition, the BWS behavior is the same within 70 pm.

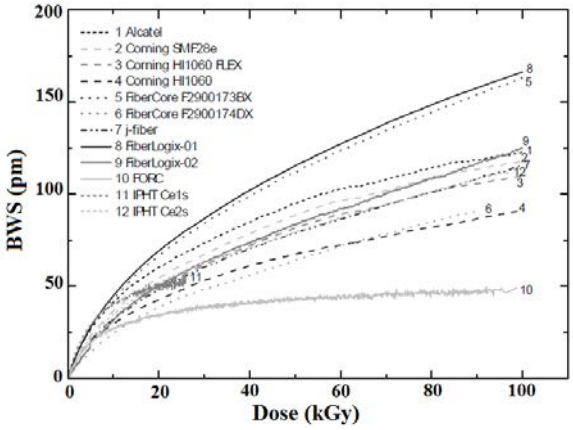

Figure 3.4: Bragg wavelength shift of gratings made of different fibers, during γ-irradiation at RT up to 0.1 MGy, with dose-rate of 0.9 Gy/s [120].

Therefore, fibers that show higher radiation induced attenuation do not give rise to gratings with higher radiation sensitivity. The cause is that the grating inscription with high UV light intensity changes the fiber properties so much that the resulting material can no longer be compared with that of the initial fiber and even the defect generation by ionizing radiation in this new material will be different [120]. However, Lin et al. observed in B/Ge co-doped fibers that the higher the GeO_2 concentration, the higher the FBG radiation sensitivity, easy to explain as the formation of more Ge-related color centers [121].

In addition of the core doping, another method used to enhance the fiber photosensitivity is the *H_2-loading* before the grating writing; to accelerate the hydrogen out-diffusion and stabilize the grating, an annealing has to be performed after the writing. As the hydrogen increases the fiber sensitivity to UV light, it increases also the radiation sensitivity of gratings. Indeed, BWS saturates at higher shift levels and at higher doses for gratings written in loaded fibers than in the unloaded [63, 121, 122]. A probable reason of the high radiation-sensitivity of gratings written in hydrogen-loaded fibers is the radiolytic rupture

of the OH-bonds, whose concentration increases with the H_2-loading [122]. Moreover, it seems that the higher the hydrogen loading pressure, the higher the radiation induced BWS [120].

A thermal pre-treatment increases the radiation sensitivity: the higher the annealing temperature the higher the BWS [116, 120]. The centers generated during the grating inscription recombine during the annealing, restoring the precursors.

Except special *fiber coatings*, it is not possible to write gratings with UV light without removing it, because it is not transparent at such wavelengths. So, gratings have to be inscribed in a bare fiber and then a coating has to be applied. Most of results here reported have been realized on bare gratings and they have to be attributed to the radiation effects on the glass. However, the coating influences the grating radiation-sensitivity [123]: the radiation modifies the coating, which can shrink or swell, causing a stress on the fiber and so a Bragg wavelength shift, for example a red-shift if the stress along the grating is symmetric and uniform. The grating radiation sensitivity increases by increasing the coating thickness or if the coating is in polymer and not in acrylate. However, it can be thought that the coating could shield rays, in fact this effect has to be considered only with UV light or X-rays of very low energy, but not for γ-rays with an energy of about 1 MeV [124].

Besides the fiber, the conditions of writing and using could also influence the grating response under radiation. The grating radiation sensitivity does not depend on the writing UV laser light, for example its wavelength, whether it is cw or pulsed [125]. It depends on the Bragg wavelength initial value and it increases with increasing λ_{Bragg} [88], whereas it depends slightly on the fiber tension during the grating inscription, indeed the BWS decreases by increasing the tension [124].

Even if the light power increasing reduces the fiber RIA, by the phenomenon known as photo-bleaching, the grating response is independent of the light power used for measuring the spectra [125].

Finally, a dependence of the grating radiation sensitivity was found on the irradiation conditions, in particular on:

- dose-rate: by increasing the dose-rate, the BWS still continues saturating but at higher shift levels and at higher doses [126];
- irradiation temperature: the BWS decreases with increasing temperature, because it facilitates the defect annealing [124].

It was also observed that a *pre-irradiation* could reduce the radiation sensitivity, because during the pre-irradiation most of the precursors is converted [121]; however, this effect

depends on the post-irradiation recovery [116].

Before concluding this discussion on BWS, it has to be highlighted that a shift of the Bragg peak *towards shorter wavelengths* was also observed in few cases. This was noticed for the first time by Niay et al. [115], but the grating transmission spectra were recorded only several days after irradiation. Gusarov et al. [127] focused their attention on this atypical behavior in type I-FBGs written in a photosensitive fiber doped with ∼8 mol% of GeO_2. As shown in fig. 3.5, at the beginning of the exposure, the BWS increases, as expected, but at the moment when it seems to start to saturate, the direction of the shift is inverted and the peak shifts towards shorter wavelengths. The authors proposed the existence of two different types of defects: one responsible for the refractive index increase and the other for the index decrease.

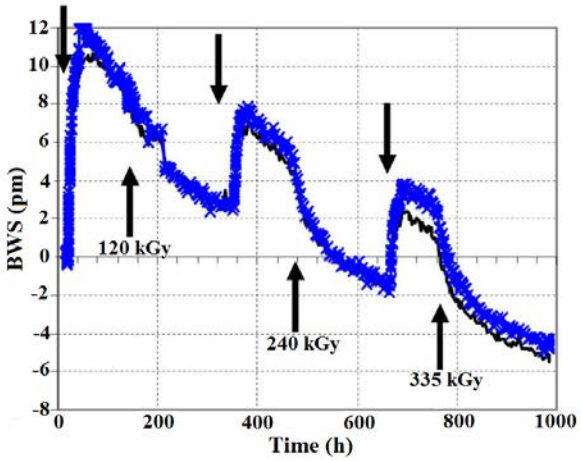

Figure 3.5: Bragg wavelength shift of two gratings written in the photosensitive fiber PS-1550-Y3 from Stocker-Yale by a 248 nm pulsed laser, during the annealing-interrupted γ-irradiation at ∼33°C, with dose-rate of 1 kGy/h. The down/up arrows indicate the start/end of the irradiations, with the total accumulated dose values. Lines without marking–grating with peak at 1537 nm; lines with crosses–grating with peak at 1550 nm [127].

Beyond the Bragg wavelength, the peak is characterized by its width and amplitude, which generally have similar dependence on dose. In most of works about gratings under radiation, these parameters do not change, above all for gratings made of unloaded fibers, whereas for gratings written in H_2-loaded fibers they initially increase and then decrease [63, 122]. This non-monotonous behavior can be explained with a non-monotonous change of Δn^{mod}. At the beginning of the irradiation, the refractive index at the maxima of the UV-fringe pattern grows faster than at the minima, increasing Δn^{mod}. At an irradiation time, the refractive index at the maxima starts to decrease slowly, while the

refractive index at the minima continues to grow, giving rise to a decrease of Δn^{mod} [122].

By increasing the annealing temperature, in contrast with the BWS increase, the amplitude decreases [116].

Finally, several works show that the temperature sensitivity is not influenced by radiation [63, 64, 120, 128].

UV fs-FBGs

A study about the radiation effects on FBGs written by fs UV laser in Ge-doped fibers was recently published by Gusarov et al. [118]. The Bragg wavelength of these gratings red-shifts with a saturating tendency at a level independent of the fiber composition, the hydrogen loading or the initial strength, whereas the post-irradiation recovery is significant and slightly dependent on the fiber type. As a consequence of the dependence of the annealing rate on the fiber type and the independence of the saturation level, it can be highlighted that the saturation has to be due to a limited concentration of precursors sensitive to the ionizing radiation. The amplitude slightly decreases, with a saturating tendency dependent on the fiber type.

As shown in fig. 3.6, for gratings written in different fibers with or without H_2-loading, the BWS saturates after a total dose of 30-40 kGy (dose rate of 0.3 Gy/s), around 15 pm. This low saturation level can be obtained also for grating written by cw UV laser but under particular writing conditions (for example, using low intensity UV light) and only at higher total doses. However, the behavior of the hydrogen loaded fibers is in contrast with the previous results.

Type IA FBGs

Compared to standard gratings, type IA FBGs are more radiation sensitive [129]. During irradiation the Bragg wavelength red-shifts with a slow saturation tendency: the higher obtained value of $\Delta\lambda_{Bragg}$ is 190 pm at the accumulated dose of 116 kGy (dose rate of 0.2 Gy/s), for a grating written in a hydrogenated B/Ge co-doped fiber. Moreover, the post-irradiation annealing is so strong that a negative BWS is observed at ∼1000 h after the irradiation end. This effect can be easily explained by a model based on the radiation generation of two types of defects, similar to the model proposed by Gusarov et al. to explain the λ_{Bragg} blue-shift [127].

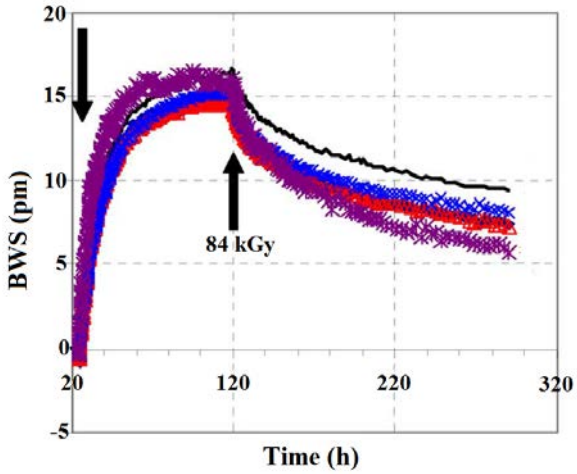

Figure 3.6: Bragg wavelength shift of gratings written in Ge-doped fibers by a fs UV laser (λ = 264 nm, τ_{pulse} = 220 fs), during the γ-irradiation at ~35°C up to a total dose of 84 kGy, with dose-rate of 0.84 kGy/h. The down/up arrows indicate the start/end of the irradiation. With the exception of the violet asteriks, associated with a grating written in the hydrogen loaded SMF-28, all the other curves are associated with FBGs written in the unloaded photo-sensitive Fibercore Ltd. PS1250/1500 with different laser fluence (and initial grating strength): red triangles–0.73 kJ/cm^2 (14.1 dB), black line–0.75 kJ/cm^2 (15.2 dB), black diamonds–1.38 kJ/cm^2 (19.2 dB), blue crosses–2.91 kJ/cm^2 (17.5 dB). [118].

Type IIA FBGs

If type IIA gratings are made of only Ge-doped fibers [116], the Bragg peak shifts towards longer wavelengths, with a saturating behavior and no significant post-irradiation recovery, whereas the peak amplitude change is rather small. In contrast to the results on type I gratings, it was observed no dependence of the BWS on the GeO_2 concentration or monotonic behavior as a function of the annealing temperature, even if the shift is larger for the grating annealed at the highest temperature than for the others. The best result was obtained for a grating made of an unloaded SM310 fiber (75 mol% GeO_2): the BWS saturates around only 12 pm, after a dose of 30 kGy (dose rate of 0.1 Gy/s).

If gratings are made in B/Ge co-doped fibers [130], the initial increase of the Bragg wavelength is followed by a marked decrease, with no significant recovery after irradiation. The authors conclude that the original UV induced reduction of the average refractive index leading to the peak blue shift during inscription is continued by the high energetic γ-radiation. The peak amplitude is reduced; moreover, the strongest the grating, the lower the amplitude reduction.

3.5.2 IR fs-FBGs

The radiation effects on the IR fs-FBGs were studied for the first time by Grobnic et al. [66]. Fig. 3.7 shows the γ-radiation-induced BWS in FBGs written in the standard Ge-doped fiber Corning SMF-28, with a dose-rate of 0.94 Gy/s up to 0.1 MGy at RT. From this graph it is clear that the H_2-loading increases the radiation sensitivity, especially for type I-IR gratings, that have higher BWS than the type II-IR gratings.

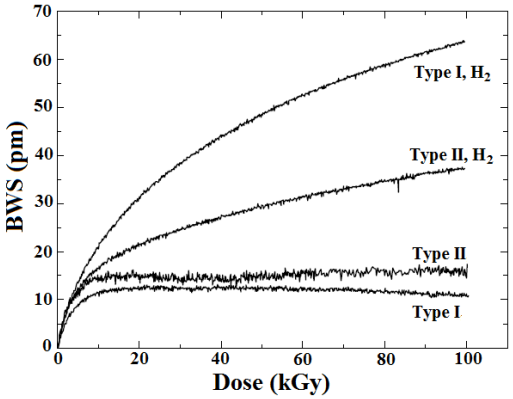

Figure 3.7: Bragg wavelength shift of type I-IR and type II-IR gratings made of a hydrogen loaded and unloaded standard Ge-doped Corning SMF-28 fiber, during γ-irradiation at RT up to 0.1 MGy, with dose-rate of 0.94 Gy/s [66].

Only for the gratings made in unloaded fibers the BWS shows a saturating behavior, at levels that are similar for both grating types and depend on the fiber composition: the radiation-induced BWS is larger in the fiber with higher RIA at λ_{Bragg}, however a RIA difference of more than two orders of magnitude leads to a BWS difference of less than a factor 10 [66]. Fig. 3.8 shows the influence of fiber composition on the BWS: the gratings made of radiation-resistant fibers (indicated in the figure with 1,3), doped only with F or GeO_2, result in FBGs more radiation-resistant than those made of radiation-sensitive fibers, doped with CeO_2 and/or P_2O_5 (indicated in the figure with 4,5).

The saturating level depends also on the grating pre-treatments: as for UV-FBGs, exposure to higher temperatures increases the radiation sensitivity. However, the annealings are often necessary to stabilize the gratings, that blue-shift of 1-5 pm/day [131].

As it is clear from curves 1 and 3 in fig. 3.8(b), the BWS decreases for dose higher than 20 kGy. This behavior was confirmed by Henschel et al. in another work realized on similar samples at higher doses, up to 1 MGy [131]: λ_{Bragg} increases at the irradiation start and then it begins to decrease at a dose depending on the fiber composition, around 100 kGy for a F-doped core, 250 kGy for a Ge-doped core and 500 kGy for a pure-silica core. The decrease of the Bragg wavelength can be caused by a decrease of n_{eff} or Λ.

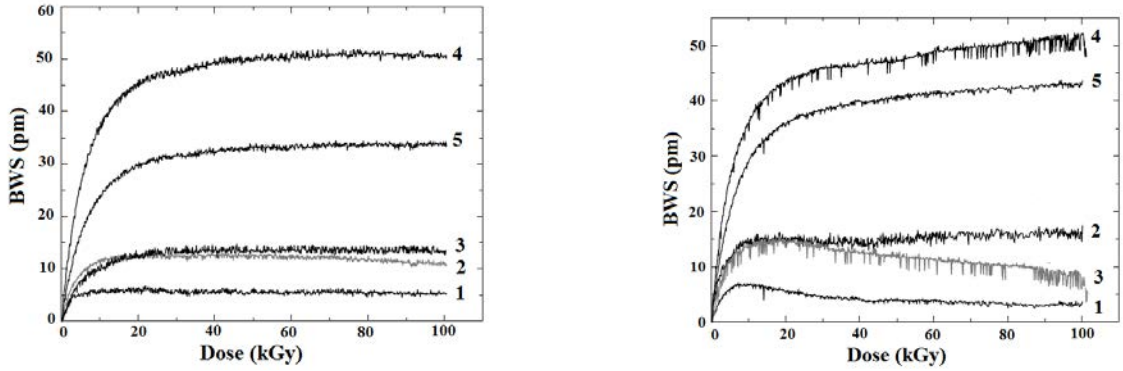

(a) Type I-IR FBGs

(b) Type II-IR FBGs

Figure 3.8: Bragg wavelength shift of (a) type I-IR and (b) type II-IR gratings made of unloaded fibers, during γ-irradiation at RT up to 0.1 MGy, with dose-rate of 0.94 Gy/s. Sample designations: 1–Fujikura RR-C (F), 2–Corning SMF-28e (GeO_2), 3–Fiber-Logix FL-HNA-01 (GeO_2), 4–Forc 141-2 (Al_2O_3, P_2O_5, F), 5–IPHT Jena Ce2s (GeO_2, CeO_2) [66].

Finally, in contrast with the UV-induced gratings, the temperature sensitivity coefficient decreases by 9% after 1 MGy dose [131].

3.6 Effects of mixed γ-neutron radiation

As just seen, a lot of papers have been published until now about the γ-radiation tolerance of the gratings. In contrast, very few tests were performed on the gratings in nuclear reactor cores and all on the standard gratings: type I-UV FBGs. The sensitivity of the Bragg wavelength to mixed γ-neutron radiation is higher than that to pure γ-radiation [132]. λ_{Bragg} red-shifts showing a saturating behavior under a neutron flux lower than $1.5 \cdot 10^{11}$ $\mathrm{n\,cm^{-2}\,s^{-1}}$, with a γ-dose-rate up to 180 Gy/h, whereas under an higher neutron flux (lower than $1.5 \cdot 10^{14}$ $\mathrm{n\,cm^{-2}\,s^{-1}}$), with a γ-dose-rate up to 9 MGy/h λ_{Bragg} increases almost linearly with increasing dose without any saturation and the peak width also increases, indicating the grating erasure.

Annealing at high temperatures and pre-irradiation do not improve the grating radiation stability [133]. As for the γ-radiation, the hydrogenation increases the grating sensitivity: the wavelength shift, the amplitude reduction and the peak broadening are bigger for the grating written in loaded fibers than in the unloaded one [132–134].

The temperature sensitivity does not change because of the radiation [134].

Since their discovery in 1978 several research groups have been interested in the radiation sensitivity of the Fiber Bragg Gratings: this depends on a lot of parameters, such as fiber composition, pre-treatments, writing and irradiation conditions. Due to the radiation, the Bragg wavelength peak shifts towards the blue or the red and sometimes it shows a non-monotonic behavior. This is attributed to the presence of different types of defects.

It is worth noting that the grating response depends strongly on the pre-thermal treatment: the higher is the used temperature, the higher is the resulting radiation sensitivity. However, the annealings are often necessary to stabilize the gratings.

Under γ-radiation, the most radiation-resistant grating at the beginning of this thesis was the FBG written with a femtosecond radiation at 800 nm in a radiation resistant fiber: the radiation induced Bragg wavelength shift saturates around 5 pm after a dose lower than 10 kGy and, at higher doses, the BWS can remain constant or decrease, depending on the fiber and FBG characteristics.

Under mixed γ-neutron radiation, no test has been reported yet on this type of gratings; however, for the UV-FBGs, a saturation behavior of BWS was observed for low neutron flux, around $2 \cdot 10^{11}\ \mathrm{n\,cm^{-2}\,s^{-1}}$, similar to that observed under pure γ-radiation, whereas at higher flux the Bragg wavelength showed a linear dependence on the dose.

Depuis leur découverte en 1978 plusieurs études ont été consacrées à l'évolution des réseaux de Bragg sous rayonnement. Cette évolution dépend de différents paramètres ; la composition des fibres, les prétraitements, les conditions d'inscription et d'irradiation. Sous rayonnement, la longueur d'onde de Bragg se décale vers le bleu ou le rouge et peut aussi présenter une évolution non monotone. Ces résultats vont dans le sens de l'existence de différents types de défauts à l'origine de la formation et de la réponse des réseaux de Bragg inscrits sur fibre.
Il est intéressant de noter que la réponse du réseau dépend fortement du prétraitement thermique. Les résultats publiés montrent que plus la température du pré-traitement est élevée, plus la variation de la réponse du réseau sous rayonnement est importante. Les recuits sont souvent nécessaires pour stabiliser les réseaux.
Sous rayonnement γ, l'état de lart au début de la présente thèse montrait que le réseau de Bragg le plus résistant aux radiations était le FBG inscrit par laser à impulsion femtoseconde à 800 nm dans une fibre résistante au rayonnement : le décalage induit par le rayonnement de la longueur d'onde de Bragg (BWS) commence par saturer autour de 5 pm après une dose inférieure à 10 kGy et, à fortes doses, le BWS peut rester constant ou évoluer à nouveau en fonction des caractéristiques de la fibre et du FBG.
Sous rayonnement mixte, gamma et neutrons, aucun test n'avait encore été réalisé sur ce type de réseau. En revanche pour les FBG inscrits par insolation UV, un comportement de saturation du BWS a été observé pour de faible flux de neutrons, autour de $2 \cdot 10^{11}$ n cm^{-2} s^{-1}, similaire à celui observé sous rayonnement gamma seul, tandis que à plus haut flux la longueur d'onde de Bragg a montré une dépendance linéaire de la dose.

Fin dalla loro scoperta nel 1978 diversi gruppi di ricerca si sono interessati alla fotosensibilità dei reticoli di Bragg: questa dipende da molti parametri, come la composizione della fibra, i pre-trattamenti, le condizioni d'iscrizione e irraggiamento. A causa della radiazione, il picco di Bragg si sposta verso il blu o rosso e, in alcuni casi, mostra un andamento non monotono. Questo comportamento è stato attribuito alla presenza di diversi tipi di difetti a l'origine della formazione e risposta dei reticoli di Bragg iscritti in fibra.
È importante notare che la risposta dei reticoli dipende fortemente dal pre-trattamento termico: più alta è la temperatura utilizzata, maggiore è la sensibilit risultante alla radiazione. Tuttavia, i trattamenti sono spesso necessari per stabilizzare i reticoli.
Sotto irraggiamento γ, il reticolo più resistente alla radiazione all'inizio della presente tesi era quello iscritto con radiazione al femtosecondo a 800 nm in una fibra resistente alle radiazioni: lo spostamento della lunghezza d'onda di Bragg indotto dalla radiazione

(BWS) satura intorno ai 5 pm dopo una dose inferiore a 10 kGy e, a dosi più elevate, esso rimane costante o evolve, a seconda delle caratteristiche della fibra e del reticolo.
Sotto irraggiamento con raggi γ e neutroni, nessun test era stato ancora effettuato su questo tipo di reticoli; tuttavia, per i FBG iscritti con radiazione UV, la saturazione del BWS è stata osservata per bassi flussi di neutroni, circa $2 \cdot 10^{11}$ $\mathrm{n\,cm^{-2}\,s^{-1}}$, comportamento analogo a quello osservato sotto radiazione gamma, mentre a flussi più elevati la lunghezza d'onda di Bragg ha mostrato una dipendenza lineare dalla dose.

Chapter 4

Materials, treatments and experimental-setups

This chapter is focused on the description of the samples, treatments and techniques used to select the most radiation resistant optical fiber and the Fiber Bragg Grating most suitable for the application aimed in this thesis. It starts with the description of the tested samples; then, it continues with the FBGs: the used fabrication technique and the measurement setups employed to monitor the Bragg wavelength during inscription, thermal treatments and irradiations. The following section is devoted to the spectroscopic techniques employed to identify the point defects in pristine and irradiated samples. Finally, it ends with the thermal treatments and irradiation sources.

4.1 Samples

The fibers studied in this thesis are made of silica glass, doped with Ge and/or F [1].

For some of the studied fibers the dopants concentration along the fiber diameter has been obtained by the *Electron MicroProbe Analysis* (EMPA), performed by the Bureau Veritas [135]. This technique allows to determine the concentrations of the different dopants present in the fiber, by studying the signals emitted from the sample when exposed to an electron beam. The spatial resolution, around 2 μm in our case, depends on the used beam diameter.

The most important characteristics of all the used fibers are reported in table 4.1.

Ge-doped fibers

- *Std-SMF* is a step-index single-mode fiber, doped only with germanium in the core and widely used in the telecom and sensor markets.

	Sample	Fiber type	$\phi_{core}(\mu m)$	$\phi_{clad}(\mu m)$	$\phi_{coat}(\mu m)$	NA
Germanium	Std-SMF	SM	8.2	125	245	0.14
	Ge-SMF	SM	9	125	242	
	Ge-MMF	MM GI	50	125	242	0.2
Fluorine	PSC-SMF	SM	8.2	125	240	0.12
	F-SMF1	SM	9	125	242	
	F-SMF2					
	F-MMF1	MM GI	50	125	242	0.2
	F-MMF2					
	F-MMF3					

Table 4.1: The most important parameters characterizing the used fibers.

- *Ge-SMF* is a single-mode fiber, doped with germanium and fluorine.
- *Ge-MMF* is a graded-index multi-mode fiber and, as Ge-SMF, it is mainly doped with germanium and fluorine, as shown in fig. 4.1: the Ge profile is parabolic with a maximum concentration of 25 wt% in the fiber center, where the F profile has a minimum.

F-doped fibers

- *PSC-SMF* is a step-index single-mode fiber having a pure silica core and a cladding in F-doped silica, surrounded by another layer in pure silica.
- *F-SMF1* and *F-SMF2* are two single-mode fibers both doped with fluorine in the core and in the cladding but with different dopant concentrations.
- *F-MMF1*, *F-MMF2* and *F-MMF3* are graded-index multi-mode fibers, characterized by different parabolic profiles for the fluorine concentration; the dopant profile of F-MMF1 is shown in fig. 4.2.

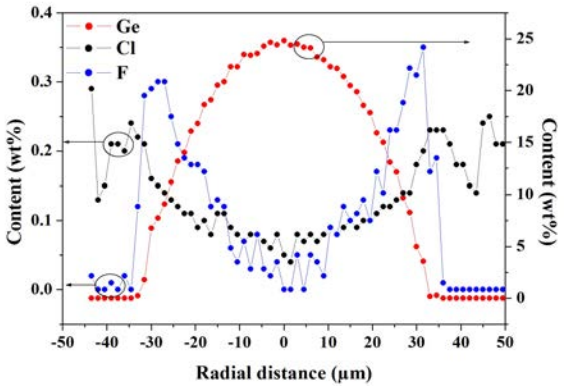

Figure 4.1: Profiles of the dopants concentration obtained with the EMPA technique for the Ge-MMF. The chlorine is an impurity due to the fabrication process.

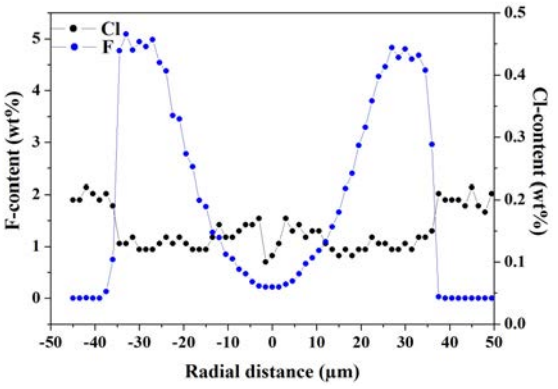

Figure 4.2: Profiles of the dopants concentration obtained with the EMPA technique for the F-MMF1. The chlorine is an impurity due to the fabrication process.

4.2 Fiber Bragg Gratings

4.2.1 Fabrication

As already mentioned, Bragg gratings can be fabricated using different techniques: the FBGs studied in this thesis were realized with the phase-mask technique, which is a simple and not very expensive method for fabricating reproducible gratings of high quality.

The phase mask (PM) [56, 92] is made by a flat slat of silica glass. On one of the surfaces, a 1-dimensional periodic surface-relief structure is etched using photolitographic techniques; the shape of the periodic pattern approximates a square wave in profile. The PM period (Λ_{PM}) determines as well the period of the imprinted grating:

$$\Lambda = \Lambda_{PM}/2 \tag{4.1}$$

and it is independent of the laser wavelength. In contrast, the corrugation depth (A_{PM}) is a function of the laser wavelength (λ_{laser}) and of the refractive index of the phase mask glass at that wavelength ($n_{silica}(\lambda_{laser})$); in order to result in a diffraction pattern with less than 5% of its total intensity in the zero-order and approximately 35% in the diverging +1 and -1 orders:

$$A_{PM} = \frac{\lambda_{laser}}{4(n_{silica}(\lambda_{laser}) - 1)} \tag{4.2}$$

For the inscription, the stripped optical fiber, to which is applied a slight tension using

small weights, is placed almost in contact with the PM, with the grating corrugations normal to the fiber axis, as shown in fig. 4.3. The laser light passes through the PM at normal incidence, it is phase modulated spatially and diffracted, therefore it forms an interference pattern along the fiber axis, which causes the refractive index modulation.

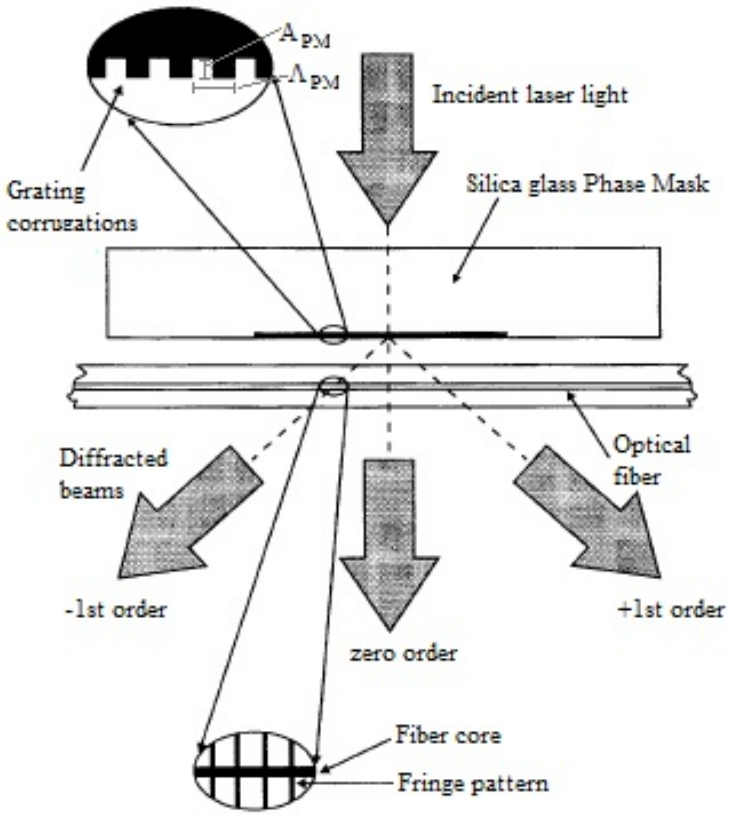

Figure 4.3: Scheme of the apparatus using the phase mask technique [92].

To write a FBG, besides the phase mask, a fused-silica cylindrical lens is required: when its axis is parallel to the fiber axis, it focuses the laser light on a line, in particular on the fiber core, and increases the energy density.

The Bragg gratings have been written by using two different lasers.

- **UV continuum laser**

  FBGs were written in the H_2-loaded standard telecom fibers (Ge-doped ones) by using a frequency doubled CW argon-ion laser (Coherent). This laser, emitting at 244 nm (5.1 eV), has a spot diameter of $\sim$1 mm and it is powerful (maximum power of 250 mW). So, a grating can be realized directly, without moving the fiber, by using a beam expander. It is a system composed by two cylindrical lenses separated by the sum of their focal lengths and it transforms the laser beam with a circular cross section into an elongated beam.

- **IR femtosecond laser**
  Other gratings were written in Ge-doped or Ge-free fibers by a Ti-sapphire laser, emitting 150 fs pulses at 800 nm (1.55 eV) with a repetition rate of 1 kHz. To irradiate all the core, the focusing lens can be translate perpendicularly to the direction of light propagation at a frequency ranging between 10 mHz and 10 Hz. The area of the laser spot is smaller than 3 μm $\times$ 1 cm.

4.2.2 Set-ups for the Bragg wavelength monitoring

The Bragg wavelength monitoring during inscription, thermal treatments or irradiations was realized in the transmission and reflection configurations, by three experimental systems.

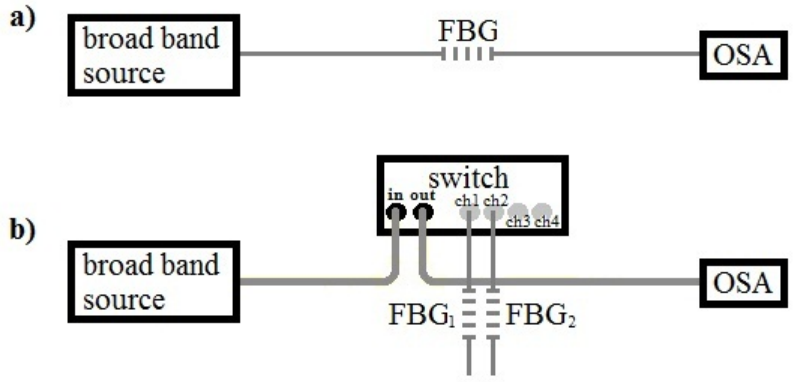

Figure 4.4: Block scheme of the **standard setup** in transmission (a) and reflection (b) configuration. The gray lines represent optical fiber cables.

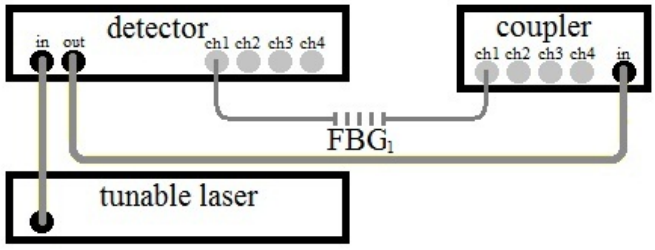

Figure 4.5: Block scheme of the **high-performance setup**. The gray lines represent optical fiber cables.

- The **standard set-up** (fig. 4.4) is realized by a broadband source, as the Erbium doped fiber source Photonetics FIBERWHITE, and the AQ6370C Optical Spectrum Analyzer (from Yokogawa), working in the wavelength range between 600 and

1700 nm with the maximum resolution of 0.02 nm. It can operate in both configurations; moreover, more fibers can be investigated automatically in the reflection configuration, one after the other, by using a switch.

- The **reflection set-up** is made up by the NI PXIe-4844 optical sensor interrogator: a system suitable for FBG optical sensors, with four optical channels that work in the wavelength range between 1510 and 1590 nm, with a resolution of 30 pm; all the channels are simultaneously sampled at 10 Hz.

- The **high-performance set-up** (fig. 4.5) is realized by a coupler, the tunable laser Tunics Plus (from NetTest) and the CT400 high performance optical tester (from Yenista Optics), operating in the wavelength range between 1260 and 1650 nm with a maximum resolution of 1 pm; this setup can realize simultaneously the transmission spectra of up to 4 gratings in few seconds, depending on the sweep range.

Peak analysis

Fig. 4.6 shows a typical transmission spectrum of a FBG and the principal parameters used to define the Bragg peak.

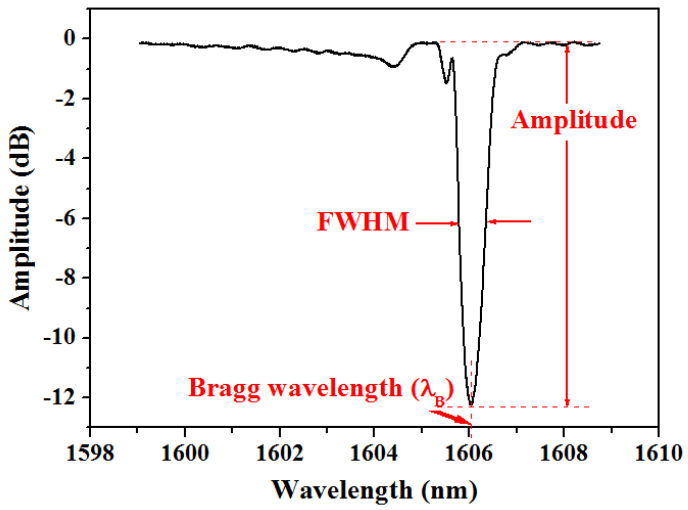

Figure 4.6: Example of the transmission spectrum of a FBG.

- The Bragg wavelength is found using a third order polynomial approximation of the peak, to account for a possible peak asymmetry, on a number N of points in the transmission (or reflection) spectrum near the main dip (or peak). The value of N

is chosen in order to obtain the best fit possible and a variation of the calculated value for λ_{Bragg} lower than 5 pm for N varying by 30% of its value.

- The grating amplitude is calculated as the difference between the value of the measured and the reference spectra, both calculated at λ_{Bragg}. The reference spectrum is the transmission or reflection spectrum of the fiber without FBGs and it is simulated by a high-order polynomial realized over all the spectrum range without the portion of about 10 nm around the peak wavelength. This procedure eliminates the influence of the light source intensity fluctuations and also the effect of the fiber transmission degradation.

- The full width at half maximum, FWHM, is calculated as the distance between two points on the two sides of the central wavelength at which the amplitude is half of the maximum peak value expressed in dB.

4.3 Spectroscopic techniques

In order to study the fiber response, firstly the induced attenuation was evaluated in the visible and infrared regions of the spectrum at room temperature (RT) before and after irradiation, to estimate the permanent losses. Subsequently, thermal treatments were performed on the irradiated samples to evaluate the high temperature treatment effects on the attenuation. To well identify the origin of the observed absorption bands, photo-luminescence measurements were performed, whereas electron spin resonance spectroscopy was used to investigate paramagnetic defects. Structural changes induced by radiation and thermal treatments were investigated by Raman spectroscopy.

4.3.1 Radiation Induced Attenuation

In order to evaluate the changes permanently induced by radiation on the transmission spectrum, RIA measurements at RT were performed by using the *cut-back* technique [17]. It consists of recording the transmission spectrum of a long and a short length of the sample, $I_L(\lambda)$ and $I_l(\lambda)$ respectively. The shorter length is obtained by cutting a fiber length ΔL, without changing injection conditions (fig. 4.7).
The spectral attenuation is defined as:

$$RIA(\lambda) = -\frac{10}{\Delta L} \cdot \log_{10}\left(\frac{I_L(\lambda)}{I_l(\lambda)}\right) \text{ (dB/m)}\,^{1} \tag{4.3}$$

[1]The absorption coefficient in cm^{-1} is equal to $2.303 \cdot 10^{-3}$ times the loss in dB/m.

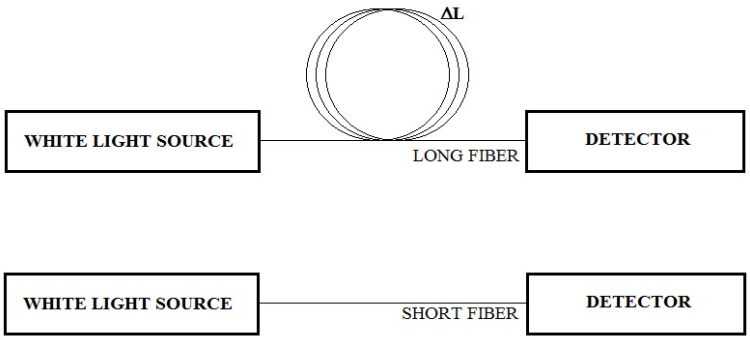

Figure 4.7: Diagram of the cut-back technique

All the transmission spectra were recorded using a halogen (or deuterium) lamp emitting light from ∼400 nm up to over 2000 nm (∼150 nm to 900 nm), coupled to a spectrometer QE65000 from Ocean Optics for the UV-Visible range, between 200 and 750 nm, and to an Optical Spectrum Analyzer AQ6370C from Yokogawa for the IR range, between 750 and 1700 nm.

Annealing effects on the RIA

Depending on the loss level, different lengths of the irradiated samples were heated in air. The fibers were coiled to diameters of around 10 cm and put inside quartz cylinders to avoid contact with the inner surface of the furnace. The acrylate coating of the fibers can not indeed stand temperatures higher than 100°C and it is totally removed by heat treatment, with no additional effect on the transmitted signal. The tested fiber was spliced, at both ends, to fiber pigtails. The optical transmission signal was recorded at room temperature before and after the thermal treatment at the temperature T_{ann}, $I_{NT}(\lambda)$ and $I(\lambda, T_{ann})$ respectively. The as-measured difference spectrum $I(\lambda, T_{ann}) - I_{NT}(\lambda)$ was calculated to monitor the RIA change and so the annealing effect.

Spectral decomposition approaches

To identify the centers responsible for the attenuation, the RIA curves can be decomposed as a sum of Gaussian bands. The difficulty is choosing the number n of bands that have to be used and their characteristics (peak position, E_n, and full width at half maximum, $FWHM_n$) [136]. We have decided to fix the number of absorption bands to be considered for the decomposition on the basis of all the previous studies and not to fix their peak position and FWHM values but to let them change in small ranges centered

on the values reported in literature. However, sometimes a new unknown band has to be added to achieve good results.

The obtained result is a RIA curve expressed as:

$$RIA(E) = \sum_n A_n \exp\left(-(E - E_n)^2/(2\,{\sigma_n}^2)\right) \tag{4.4}$$

where A_n is the amplitude of the Gaussian band and $FWHM_n = 2\sqrt{2\ln(2)}\,\sigma_n = 2.355\,\sigma_n$.

The multi-gaussian decomposition is a procedure based on the fact that most of the absorption bands are Gaussian and the asymmetric ones can be always represented by several Gaussian functions. However, an easy mistake that can be committed is to associate a component of an asymmetric band to a different center. This subject will be discussed later for the NBOHC band.

Smakula's equation: from the absorption to the defect concentration

With the optical absorption technique the absolute concentration N of the absorbing species can be obtained, if the oscillator strength of the respective electronic transition is known. The *oscillator strength* f of an electric dipole transition of energy E between the initial (1) and the final (2) states is defined as [137]:

$$f = \frac{8\pi^2 m_e E}{3h^2e^2}\frac{1}{g_1} \cdot |\langle 2|\vec{p}|1\rangle|^2 \tag{4.5}$$

where g_1 is the degeneracy of the initial state, $\vec{p}$ is the electric dipole operator and $\langle 2|\vec{p}|1\rangle$ is its matrix element between the two states. Moreover, this dimensionless parameter measures the optical transition probability for the studied centers.

The oscillator strength f and the defect concentration N can be related to the absorption coefficient α by the *Smakula's equation* [137]:

$$f \cdot N = \frac{m_e c}{\pi e^2 h} \cdot \frac{9n}{(n^2+2)^2} \int \alpha(E)\,\mathrm{d}E \simeq 8.2 \cdot 10^{16} \frac{n}{(n^2+2)^2} \int \alpha(E)\,\mathrm{d}E \ [\mathrm{eV}^{-1}\,\mathrm{cm}^{-2}] \tag{4.6}$$

where $\alpha(E)$ is the absorption in cm^{-1} and n is the refractive index of the medium.
For a gaussian band-shape, $\int \alpha(E)\,\mathrm{d}E = 1.065 \cdot \alpha_{max} \cdot FWHM$.

4.3.2 Raman spectroscopy

Raman scattering is an inelastic scattering of light on molecules [32] (see section 2.2.2). The energy difference between the incident and emitted photons corresponds to the energy

difference between the initial and final vibrational levels and it is independent of the absolute energy of the photon, which generally falls in the visible and near-infrared regions of the spectrum. The Raman spectroscopy is very useful to study the vibrational modes of the molecules and so to obtain information on its structure: a Raman spectrum shows the intensity of the scattered light as a function of its frequency difference with respect to the incident photon.

Confocal micro-spectroscopy setup

All the Raman spectra were performed with the LabRAM Aramis (Horiba Jobin Yvon), an integrated confocal microRaman system [138], whose schema is shown in fig. 4.8.

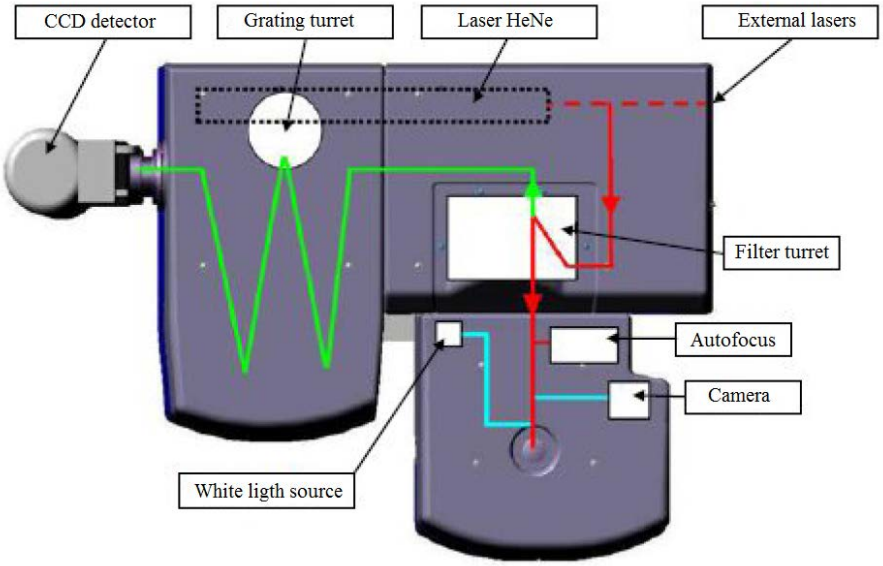

Figure 4.8: Optical path in the LAbRAM Aramis system [138].

To examine small volumes of the sample ($\sim \mu m^3$), a confocal microscope uses a point illumination, which is a laser light focused on the sample by an objective. The light signal from the sample goes through a pinhole placed in an optically conjugate plane in front of the detector and playing the role of the spectrograph entrance slit, to eliminate out-of-focus signal. As a consequence, only the light that can be detected is the one produced in a region very close to the focal plane, within a depth:

$$\Delta z = \frac{0.9\lambda_0 \, n_{medium}}{NA^2} \tag{4.7}$$

where n_{medium} is the refractive index of the medium between the sample and the objective, generally air, NA is the numerical aperture of the objective and λ_0 is the laser wavelength [139]. For example, for a laser light at 325 nm and a 40× objective with $NA = 0.5$,

$\Delta z \sim 1$ μm.

The used confocal system is coupled to a 460 mm focal length spectrograph equipped with a four interchangeable gratings turret. The excitation is realized by three different sources: a HeNe laser working at 633 nm (1.96 eV), an Ar^+ laser at 488 nm (2.54 eV) and a HeCd laser emitting at 442 nm (2.81 eV) and at 325 nm (3.82 eV). The laser power can be reduced by choosing one of the available density filters via software. On the incoming path, the laser beam is reflected towards the microscope by the means of a special filter used in injection/rejection mode. On the return path to the spectrograph, the Raman backscattered light is transmitted towards the confocal slit-hole located at the entrance of the spectrograph. Another filter is necessary to filter out the Rayleigh signal. Then the spectrograph disperses the multichromatic Raman signal onto the CCD multichannel detector.

Thanks to different motors, the sample stage can be moved along the three spatial directions via software: this allows to easily realize mappings of the signal on the sample surface or along its thickness. Spatial resolution depends on the used microscope objective and pinhole diameter: for example, the 40× objective used for the UV excitation light and a 75 μm pinhole imply a spatial resolution of 4.7 μm.

4.3.3 Photo-luminescence spectroscopy

Photo-luminescence, or briefly PL, is a process where an optically active defect, excited by a light at the energy E_{exc} from its ground state to a higher one, decays back to a lower state radiatively, by emitting photons of energy E_{em}, with $E_{em} \leq E_{exc}$.

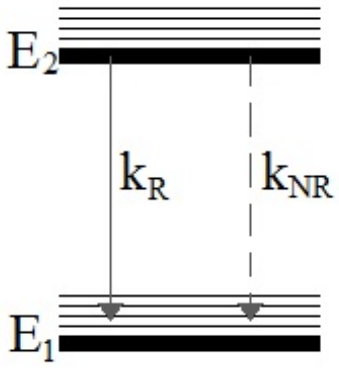

Figure 4.9: Jablonski diagram of a simple two-levels system. The continuous and dotted arrows represent the spontaneous emission and the non-radiative relaxation from the excited state, respectively.

Let us consider the simple two-levels system shown in fig. 4.9: the two levels have

energies E_1 and E_2, where $E_1 < E_2$, and populations N_1 and N_2. When the system is not excited, N_2 is almost zero, for the Boltzmann distribution. Under excitation at energy $E_{exc} \geq E_2 - E_1$, the higher level population N_2 will increase because of the absorption but it will decrease because of two processes [137]: the *spontaneous emission*, when the center decays radiatively with a temperature independent rate k_R and it emits a photon with energy $E_2 - E_1$, and the *non-radiative relaxation*, when the center relaxes with a temperature dependent rate k_{NR}, by producing phonons. So, the variation rate of the excited level population can be described by the equation [140]:

$$\frac{\mathrm{d}N_2}{\mathrm{d}t} = +A \cdot I_0(\lambda_{exc}) \cdot N_1(t) - [k_R + k_{NR}(T)] \cdot N_2(t) \tag{4.8}$$

where the first term considers the absorption of the incident light $I_0(\lambda_{exc})$ and A is a proportional coefficient.

The luminescence signal is constituted by the spontaneously emitted photons and it depends on the emission energy E_{em}, the excitation energy E_{exc} and the temperature T, according the following expression:

$$I_{PL}\left(E_{em}, E_{exc}, T, t\right) = \eta \cdot N_2\left(E_{exc}, T, t\right) \cdot f\left(E_{em}, T\right) \tag{4.9}$$

where $f\left(E_{em}, T\right)$ takes into account all the contributions to the PL band shape: the homogeneous ones, as lifetime and phonon-electron coupling, and the inhomogeneous ones, linked to the differences of the emitting centers. η is the *quantum yield*, defined as the ratio between the emitted and absorbed photons [137]:

$$\eta = \frac{k_R}{k_R + k_{NR}(T)} \tag{4.10}$$

Depending on the excitation system, we can perform different kinds of luminescence that will give different information about the transition.

Steady state luminescence is performed when the system is subjected to a continuous excitation; in this stationary regime, $\mathrm{d}N_2/\mathrm{d}t$ has to be equal to zero, so $N_2\left(E_{exc}, T\right)$ is constant. As the PL intensity is a function of the excitation and emission energies ($I_{PL}\left(E_{em}, E_{exc}\right)$), two types of spectra can be realized:

- the *emission spectrum* (PL spectrum) is obtained by acquiring the PL intensity as a function of E_{em} for a fixed value of E_{exc} and it gives us the shape of the emitted band;

- the *excitation spectrum* (PLE spectrum) is obtained by acquiring the PL intensity as a function of E_{exc} for a fixed value of E_{em} and it represents the excitation efficiency of the emitting band.

Time-resolved luminescence is performed when the system is excited by a laser pulse usually of short duration, which is compatible with the characteristic time of the radiative emission. N_2 increases during the pulse and starts to decrease after it, according the following expressions:

$$\frac{\mathrm{d}N_2}{\mathrm{d}t} = -[k_R + k_{NR}(T)] \cdot N_2(t) \Longrightarrow N_2(t) = N(t=0)\exp(-t/\tau) \tag{4.11}$$

where $\tau = \frac{1}{k_R + k_{NR}(T)}$ is the *lifetime*.

Thanks to this technique, it is possible to separate temporally more PL bands present in the same spectral region and to determine their lifetimes. What is revealed, hereafter named as $F(t)$, is the signal $I_{PL}(t)$ emitted from the sample and integrated in a time window $[T_D\,,\, T_D + \Delta t]$, where T_D is the delay time of the acquisition with respect to the excitation pulse and Δt is the amplitude of the time window, as shown in fig. 4.10:

$$F(T_D + \Delta t) - F(T_D) = \int_{T_D}^{T_D + \Delta t} I_{PL}(t')\,\mathrm{d}t' \tag{4.12}$$

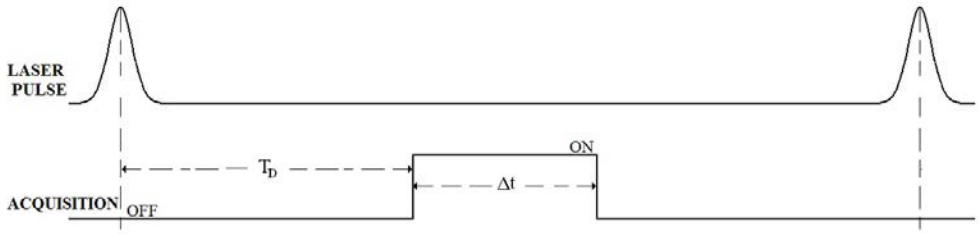

Figure 4.10: Time trends of the laser pulse and the acquisition, conceived as a variable having two values (ON and OFF), for the time-resolved luminescence technique.

The steady state PL spectra were recorded with the confocal microRaman system LabRAM Aramis (Horiba Jobin Yvon), described in the previous section, which can also perform confocal microluminescence measurements. Instead, the time-resolved PL spectra were performed with the setup illustrated in the following.

Time resolved luminescence setup

In contrast to the system available for the stationary luminescence, whose excitation can be realized at four different energies, the excitation source of the time resolved luminescence setup is a tunable laser (Spectra Physics [141]). This consists of a Q-switched Nd:YAG laser emitting at 1064 nm with a repetition rate of 10 Hz. A set of non-linear crystals allows to obtain the third harmonic at 355 nm. Then, the Optical Parametric

Oscillator (OPO) converts the incident light, at frequency ω_0, into two beams, signal and idler, whose frequencies, ω_s and ω_i respectively, have to fulfill the relation:

$$\omega_0 = \omega_s + \omega_i \tag{4.13}$$

The signal wavelength varies from 410 to 709 nm and that of the idler from 710 to 2630 nm. After the OPO, UV modules extend the output wavelength range down to about 200 nm. At the laser exit, the beam energy can be monitored by a pyroelectric detector. The accuracy of the energy measure is 15%, taking into account the laser fluctuations.

The optical fiber can be excited in two ways:

- longitudinal excitation, if the laser beam is injected inside the sample through a cleaved end by using an objective (fig. 4.11(a));
- transverse excitation, if the laser beam is focused, through the cladding, into the core of a stripped piece of fiber (fig. 4.11(b)).

The PL signal emitted by the sample is guided by the optical fiber itself to the other cleaved end, collected by two lenses and injected into the spectrograph, through a slit. The spectrograph is equipped with three gratings with 300 grooves/mm and different values of the blaze wavelength (300, 500 and 1000 nm). The spectral resolution is about 10 nm/mm. Finally, the spectrally resolved signal is amplified and detected by a gated intensified CCD (PI-MAX 3 Princeton-Instruments [142]), working in the UV-Vis-nearIR range. The CCD is triggered by an electronic synchronization signal produced by the laser before the pulse emission, in order to acquire spectra only in the chosen time windows. These are characterized by two parameters: the time width Δt, that is the amplitude of the acquisition window during which the CCD is enabled to reveal the light, and the delay T_D of the acquisition window with respect to the arrival of the laser pulse.

The photoluminescence excitation (PLE) spectra can be measured manually, point by point, by tuning the laser and recording the PL intensity normalized to the laser pulse energy. All the PL spectra plotted in energy scale are corrected for the monochromator dispersion.

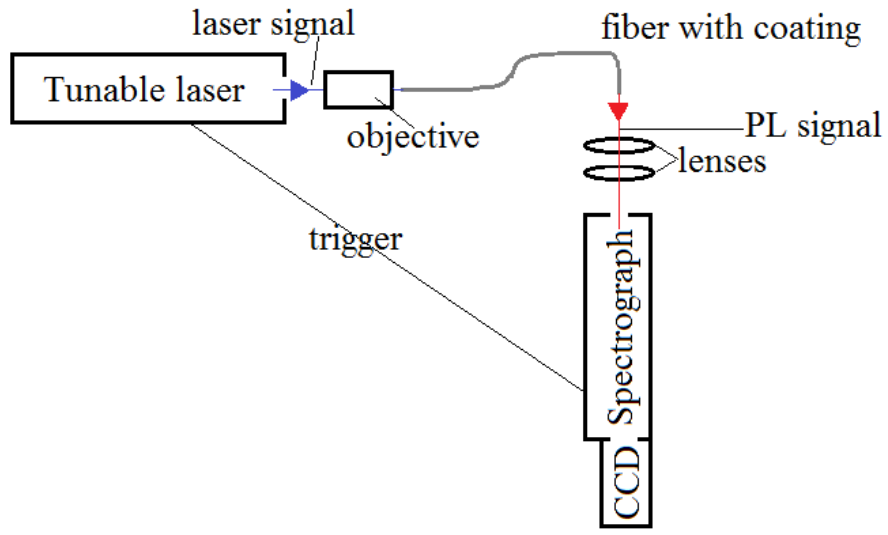

(a) Longitudinal excitation

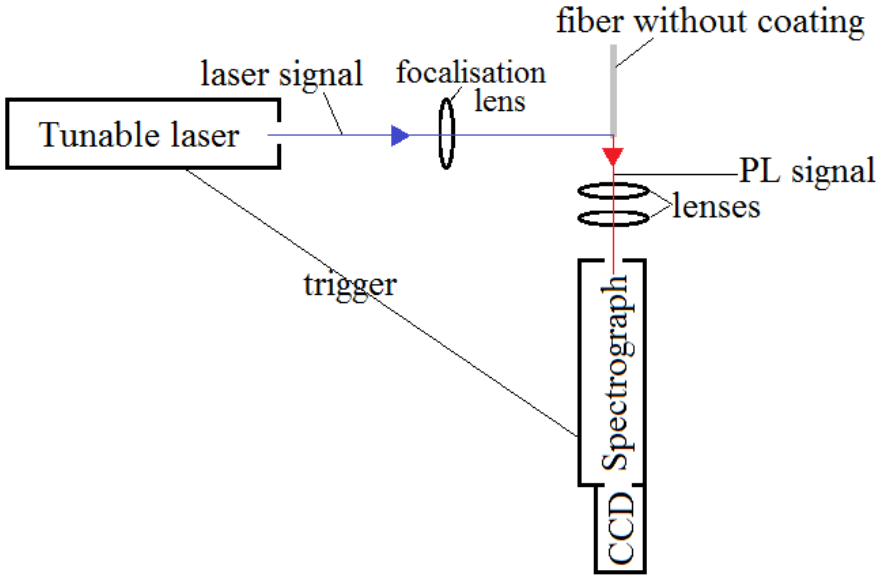

(b) Transverse excitation

Figure 4.11: Block scheme of the time resolved luminescence set-ups: (a) longitudinal excitation and (b) transverse excitation.

4.3.4 Electron Paramagnetic Resonance

Electron Paramagnetic Resonance (EPR), or Electron Spin Resonance (ESR), studies the interaction between magnetic moments and magnetic fields.

Let us consider a center with a spin angular momentum of electrons $\vec{S}$ with magnitude $\hbar[S(S+1)]^{1/2}$, it has also an associated magnetic moment defined as:

$$\vec{\mu} = -\frac{g\beta}{\hbar}\vec{S} \tag{4.14}$$

where $\beta = \frac{|e|\cdot\hbar}{2m_e} \cong 9.3 \cdot 10^{-28}$ J/G is the Bohr magnetic moment and g is a dimensionless quantity, called the *Landé factor*. The g factor is equal to 2.0023 for a free electron, whereas for a center in a solid it is often anisotropic and varies with the direction in a single crystal.

In the presence of an external static magnetic field $\vec{H_0}$, each energetic level of the center is split in $2S+1$ levels, whose energies depend on the eigenvalues m_S of $\vec{S}$ along the $\vec{H_0}$ direction. This interaction is called *Zeeman effect* and it can be described by the following equation:

$$\mathcal{H}_Z = -\vec{H_0}\cdot\vec{\mu} = \frac{g\beta}{\hbar}\vec{H_0}\cdot\vec{S} = g\beta H_0 m_S \tag{4.15}$$

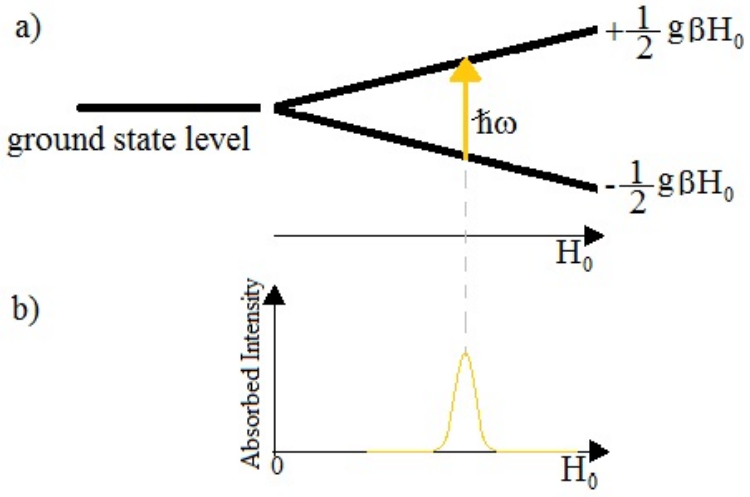

Figure 4.12: (a) Zeeman effect on the ground state level of a system with $S = \frac{1}{2}$. (b) EPR absorption spectrum obtained by varying the H_0 amplitude while keeping constant the microwave frequency ω.

If, for example, $S = \frac{1}{2}$, the ground state of the center will be split by the static field in two levels whose energies are: $E_Z = \pm\frac{1}{2}g\beta H_0$, depending on $m_S = \pm\frac{1}{2}$, as shown in fig. 4.12(a). The transition between these two levels can be induced by photons whose energy fulfills the resonance condition:

$$\hbar\omega = g\beta H_0 \tag{4.16}$$

In an EPR spectrometer, the transitions between the split levels are induced by another magnetic field, $\vec{H}_1$, oscillating at a microwave frequency ω, normal to $\vec{H}_0$ and with amplitude much smaller than the static field. Generally, the EPR spectra are recorded by measuring the microwave power absorbed by the sample as a function of the static magnetic field amplitude H_0, while the amplitude and frequency of $\vec{H}_1$ are fixed (fig. 4.12(b)).

Bruker EMX EPR spectrometer

All the EPR spectra have been recorded by the Bruker EMX EPR spectrometer [143, 144], whose block scheme is shown in fig. 4.13.

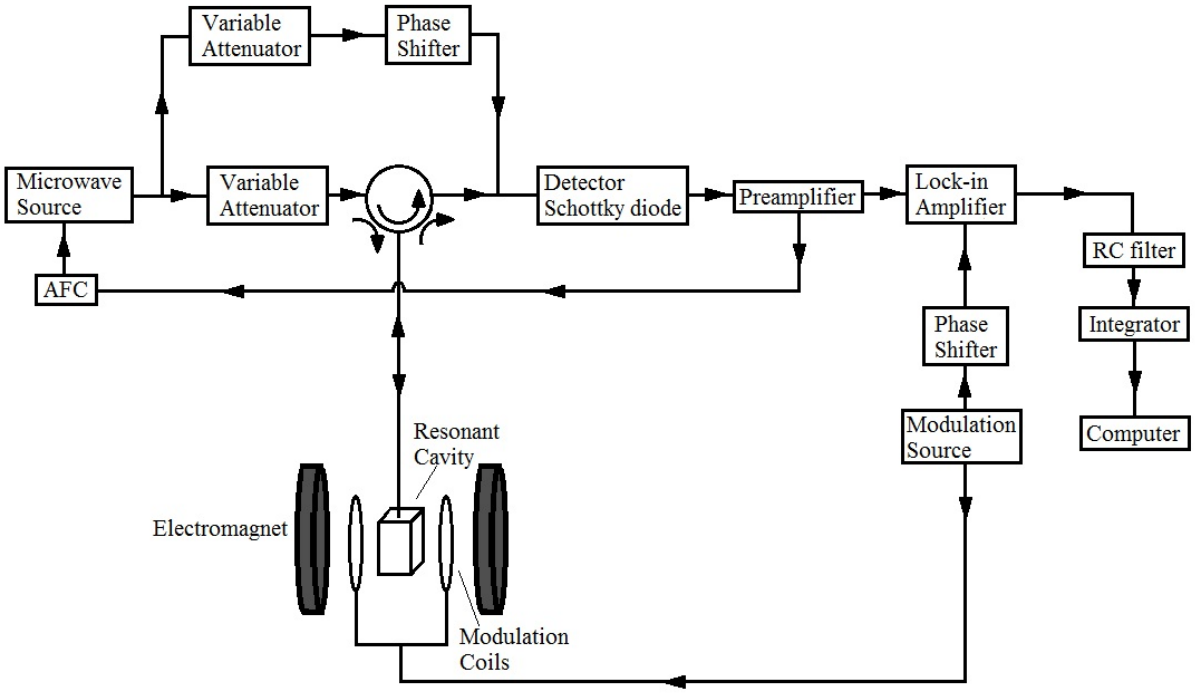

Figure 4.13: Block scheme of the Bruker EMX EPR spectrometer [143].

The resonant cavity is a metallic box with high conductive walls, resonating in the normal mode TE_{102} at about 9.8 GHz (X band). The sample is inserted at its center, where the microwave magnetic field is maximum and the microwave electric field is minimum. The microwave radiation, i.e. the oscillating magnetic field $\vec{H}_1$, is generated by a Gunn diode (a GaAS junction, which a d.c. voltage is applied to): its frequency is controlled by an Automatic Frequency Control (AFC) in order to match the resonant frequency of

the cavity-sample system and its intensity can be varied between 200 nW and 200 mW. The incident power P_i is measured in decibel units of attenuation with respect to the maximum intensity, defined as:

$$\mathrm{Att(dB)} = -10 \cdot \log_{10}\left(\frac{P_i}{200\,\mathrm{mW}}\right) \tag{4.17}$$

The microwave radiation is transmitted from the source to the cavity through a waveguide, coupled to the cavity by changing the position of a tuneable screw inside a small hole, called iris.

The resonant cavity is placed between the poles of an electromagnet, which generates the static magnetic field $\vec{H}_0$. During the measurements, its strength varies within an interval whose center and amplitude are fixed by the user near the resonance condition, and it is measured by a Hall probe, which generates a voltage proportional to the magnetic field.

Once the microwave radiation arrives to the cavity, it is partially absorbed by the sample and partially reflected. The reflected signal is converted by the detector, a Schottky diode, in a current signal proportional to the square root of its value. To enhance the sensitivity of the EPR spectrometer, a third magnetic field is added: this field is called the modulation field $\vec{H}_m$, it is oscillating at the frequency ω_m and parallel to $\vec{H}_0$, it is realized by a pair of Helmholtz coils located at the sides of the resonant cavity. Thanks to this field, the reflected power and consequently the current signal are modulated at the frequency ω_m; in this way, a lock-in amplifier can easily isolate the output signal at that particular frequency from the noise. To improve the signal to noise ratio, a RC circuit filters out all the noise components with frequency higher than $\frac{1}{\tau_{const}}$, where $\tau_{const} = RC$ is the filter response time. Finally, the current signal is converted in the digital EPR signal by an integrating Analog to Digital Converter, characterized by a conversion time T_{conv}.

The spectra were recorded in the *first-harmonic mode* [145]: the detector reveals the component of the reflected signal oscillating at the frequency ω_m and in phase with the modulation magnetic field. The obtained EPR signal is proportional to the first derivative of the real absorption line and the double integral of the EPR spectrum is proportional to the number of centers. So the absolute concentration of defects can be estimated by comparison with the double integral of the EPR spectrum of a reference sample. For this aim, it was used an irradiated silica bulk sample whose E′ concentration was known by absorption measurements. The accuracy of the absolute concentration is estimated as 20%.

To avoid a distortion of the EPR signal, some conditions have to be satisfied [146]. Let us define ΔH_{pp} as the field distance in the derivative spectrum between two consecutive peaks, ΔH_{sweep} as the interval of the magnetic field scanned and T_{sweep} as the scan time.

1. In the first-harmonic mode, the EPR signal amplitude is proportional to the square root of the microwave incident power (P_i), only for values of P_i sufficiently low to allow the relaxation mechanism to dissipate the absorbed energy (non-saturation condition). If this condition is not satisfied, the absorption intensity will reach a constant value and the line shape will be broadened. The non-saturation range of P_i depends on the defect, so a study of the EPR signal for each defect as a function of P_i is indispensable.

2. The modulation amplitude has to be less than the peak-to-peak field distance, not to obtain an average effect; it is recommended to choose:

$$H_m \leq 0.4 \cdot \Delta H_{pp} \tag{4.18}$$

3. The modulation frequency does not have to cause any transition, so $\omega_m << \frac{g\beta\,\Delta H_{pp}}{\hbar}$; if $\Delta H_{pp} \geq 3.6 \cdot 10^{-2}\,\mathrm{mT}$, $\omega_m = 2\pi \cdot (100\,\mathrm{kHz})$ is a good choice.

4. The effective frequency of the derivative of the absorption line may be considered as the inverse of the time that it takes to scan through the resonance spectrum from a peak to the next one: $\frac{v_{sweep}}{\Delta H_{pp}} = \frac{\Delta H_{sweep}}{\Delta H_{pp} \cdot T_{sweep}}$. This frequency has to be lower than the frequency of the low-pass filter:

$$\tau_{const} \leq 0.1 \frac{\Delta H_{pp} \cdot T_{sweep}}{\Delta H_{sweep}} \tag{4.19}$$

5. Because of the acquisition system, there is always a shift of the magnetic field axis: it is $\tau_{const} \cdot \frac{\Delta H_{sweep}}{T_{sweep}}$; H_m has to be larger than this error and consequently:

$$\tau_{const} << \frac{T_{sweep}}{\Delta H_{sweep}} \cdot H_m \tag{4.20}$$

4.4 Treatments

4.4.1 Irradiations

Some samples, fibers or FBGs, were irradiated with X- or γ-rays and neutrons.

X-rays irradiation

The 10 keV X-rays irradiations at RT and at high temperature (T$\approx$ 230°C) were performed at the CEA-Bruyères le Châtel, Commissariat à l'énergie atomique et aux énergies alternatives (Arpajon, France), by using two machines, Aracor and Probix, having comparable characteristics [147, 148]. Their focused beam spot is 2 cm wide and the maximum dose-rate is 50 Gy/s; the irradiation temperature can range from -50°C to 300°C.

γ-rays irradiation

The γ-rays irradiations were performed by a ^{60}Co source in the underwater γ-irradiation facility BRIGITTE in SCK·CEN (Mol, Belgium) [149]. The dose-rate varies between 10 and 30 kGy/h, whereas the temperature ranges from 30 to 50°C. The dose-rate and temperature values depend on the sample position relative to the source and so on the aimed total dose. The maximum reached dose was 10 MGy.

Neutron irradiation

The neutron irradiations were performed at the pool-type reactor TRIGA Mark II of the CNESTEN, Centre National de l'Energie, des Sciences et des Techniques Nucléaires, (Maamoura, Morocco). The neutron flux is about $2.1 \cdot 10^{12}$ n/(cm^2 s) and the γ-dose-rate is about 40 Gy/s; the accumulated dose varies between 10^{15} n/cm^2 (with a γ-dose of 0.02 MGy) and 10^{17} n/cm^2 (with a γ-dose higher than 2 MGy).

4.4.2 Thermal treatments

The thermal treatments were carried out with an electric furnace in air at three temperatures. These, hereafter referred as T_f, were chosen in agreement with the applications and they are: 300, 550 and 750°C. For each T_f treatment, a heating ramp of 10°C/min was set to reach the aimed value, followed by a 15 min lasting step at constant temperature and a cooling down at RT, accelerated by opening the oven.

Set-up for FBGs

As FBGs are both temperature and stress sensors, to study the Bragg wavelength dependence on the temperature, it is mandatory not to apply any stress during the treatments. This is easily realized as shown in fig. 4.14, by placing the written part of the fibers in the center of the oven in air by the means of a cylindrical tube having a small diameter. In order to obtain the characteristic curve $\lambda_{Bragg}(T)$ and to calculate the sensitivity coefficient, during the thermal ramps the temperature in close proximity to the grating was monitored by at least two thermocouples. Moreover, to verify the stability of the gratings already treated at 750°C, an additional treatment at 750°C was carried out with the same heating rate followed by a 45 min long step at constant temperature.

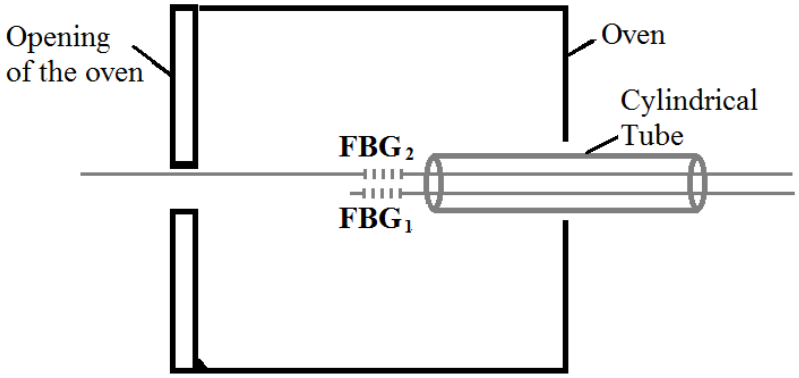

Figure 4.14: Arrangement of the FBGs inside the oven: FBG_1 in the reflection configuration and FBG_2 in the transmission configuration.

This chapter is dedicated to the presentation of the experimental techniques used in this thesis. Spectroscopic techniques (spectral attenuation, photoluminescence and electron paramagnetic resonance) used for studying the radiation-induced defects are introduced. For Bragg gratings the phase mask technique used for their inscription is detailed.

Ce chapitre est dédié à la présentation des techniques expérimentales utilisées dans cette thèse. Les techniques spectroscopiques (atténuation spectrale, photoluminescence et résonance paramagnétique électronique) utilisées pour l'étude des défauts induits sous rayonnement ionisant sont introduites. Pour les réseaux de Bragg la technique du masque de phase utilisée pour leur réalisation est détaillée.

Questo capitolo è dedicato alla descrizione delle tecniche sperimentali utilizzate durante la realizzazione di questa tesi. Diverse tecniche spettroscopiche, come l'attenuazione spettrale, la fotoluminescenza e la risonanza paramagnetica elettronica, sono state combinate per studiare i difetti indotti dalla radiazione. Per i reticoli di Bragg la tecnica della maschera di fase utilizzata per la loro realizzazione è stata illustrata in dettaglio.

Chapter 5

Bragg Grating temperature sensor under radiation

Radiation effects on FBGs have been studied for more than a decade: most of the works published so far in literature are focused on the radiation sensitivity of the oldest grating, the Type-I UV-FBG, whereas there are only few works dealing with the other types of gratings, as the IR fs FBGs.

In addition to the radiation effects on the Bragg peak, it is well known that the radiation increases the transmission losses, causing a degradation of the signal to noise ratio (SNR), up to make it impossible to measure the Bragg peak wavelength. As a consequence, it is important to choose a radiation-resistant fiber to write the grating. The Ge-doping is often used to increase the sensitivity of the fiber to the laser light and to make the FBG writing easier, but this increases the grating sensitivity to the γ-radiation and the transmission losses during irradiation, with respect to other dopings. To maintain a good SNR, short lengths of the photo-sensible Ge-doped fiber can be spliced with a radiation-resistant fiber (Ge-doped or not) [115], however the use of Ge-doped fibers for applications in nuclear environments still remains not recommended.

Since the UV laser writing can be used only in photosensible fibers, whereas the IR fs laser allows the grating inscription in all types of fibers, as the radiation-resistant ones made of pure or F-doped silica, the fs-FBGs seem more interesting for the aimed application. For these reasons, a detailed study will be presented on fs-FBGs inscribed in radiation-resistant fibers, while some results on UV-FBGs are shown for the sake of comparison.

5.1 fs-FBGs as temperature sensors

During thermal treatments, a grating undergoes not only a reversible shift of the Bragg wavelength with the temperature but also an irreversible and unintentional peak change. As example, fig. 5.1 shows the variations of the reflection spectrum of a fs-FBG written in a F-doped fiber, during four thermal treatments: the first at 300°C, the second at 550°C and the last two at 750°C (see section 4.4.2).

λ_{Bragg} varies almost linearly with temperature (fig. 5.1(b)) but its change is not only reversible: the peak at RT does not return to its initial position after a thermal treatment, as it can be observed in fig. 5.1(a). The annealing causes a partial erasure of the grating, i.e. a reduction of n_{eff} and Δn^{mod}. The first implies a blue-shift of the Bragg wavelength, whereas the second causes a decrease of both the peak amplitude (fig. 5.1(c)) and FWHM (fig. 5.1(d)); moreover, the FWHM is also inversely proportional to the grating length,

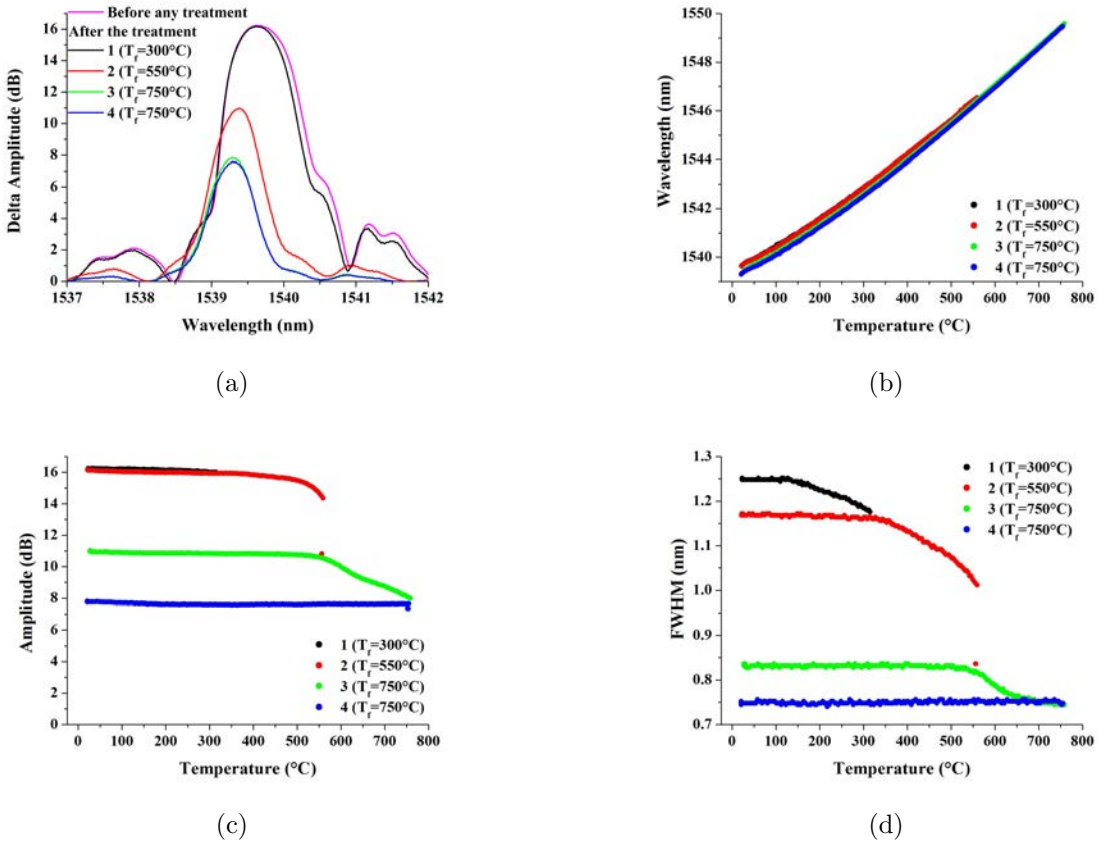

Figure 5.1: fs-FBG written in the F-doped fiber (F-SMF1) with a laser power of 500 mW: (a) changes of the reflection spectra, recorded at RT before and after the treatments; variations of (b) the Bragg wavelength, (c) the amplitude and (d) the FWHM of the peak during the four thermal treatments.

that may be thought to increase because of a lower sharpness of the grating boundaries.

These changes depend on the fiber type and on the inscription conditions. For these reasons, the grating response during the thermal treatments was studied depending on the laser power and the initial value of the amplitude, which depends on the inscription time. Two types of fibers were used: the Ge-SMF and the F-SMF1, as representative of the Ge-doped and the F-doped fibers, respectively.

The thermal treatments cause a permanent blue-shift of the **Bragg wavelength**, that can entail a systematic error on the temperature measurement if it is not considered. The results show that the higher is the initial amplitude (fig. 5.2) or the laser power used for the inscription (data not reported here), the larger is the shift. A dependence on the fiber type is also found. As shown in fig. 5.2, a second thermal treatment at 750°C causes a further shift with respect to the first treatment at the same temperature: this is around 0.2 nm, if the grating is written in the Ge-doped fiber, whereas it is only 0.02 nm, if the fiber is F-doped.

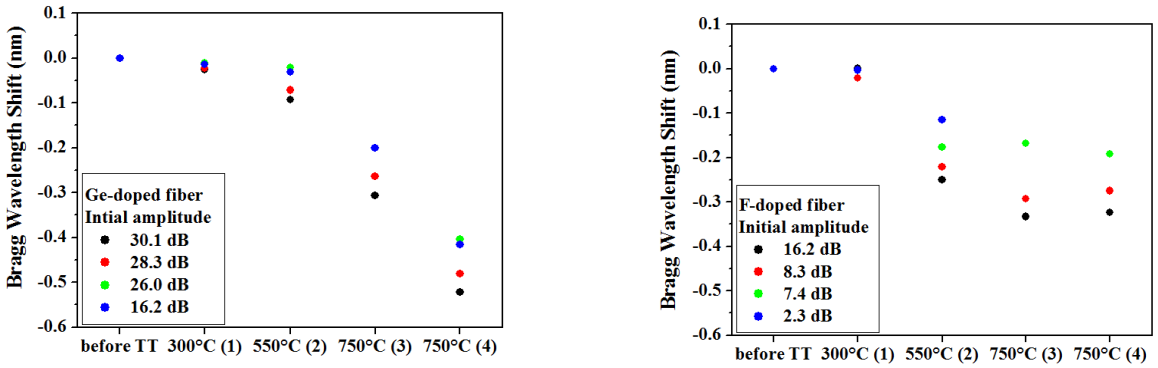

(a) (b)

Figure 5.2: Variation of the Bragg wavelength with respect to its value before any thermal treatment, as a function of the treatment temperature, for gratings written in (a) the Ge-doped and (b) the F-doped fibers. The used laser power for these gratings is 500 mW; the values of the initial amplitude are reported in the graphs.

For the **amplitude** it was obtained that the higher is its initial value, the lower is its reduction in percentage due to the thermal treatments. This depends on:

- the *laser power*, for example for two gratings written in the F-doped fiber with an initial amplitude of ∼16 dB, the ratio between its final (after the forth treatment) and initial values is:

$$\frac{A_{final}}{A_{initial}} = \begin{cases} 0.466 \pm 0.004 & \text{for } P_{\text{laser}} = 500\text{mW} \\ 0.0145 \pm 0.0010 & \text{for } P_{\text{laser}} = 400\text{mW} \end{cases} \tag{5.1}$$

- the *fiber composition*, for example for two gratings written in the two fibers with an initial amplitude of ∼16 dB:

$$\frac{A_{final}}{A_{initial}} = \begin{cases} 0.052 \pm 0.002 & \text{for the Ge} - \text{doped fiber} \\ 0.466 \pm 0.004 & \text{for the F} - \text{doped fiber} \end{cases} \tag{5.2}$$

Fig. 5.3 shows the peak amplitude normalized to its initial value as a function of the annealing temperature for the two fiber types. It can be noted that the initial amplitudes obtained for the gratings written in the Ge-doped fiber are higher than those obtained in the F-doped fiber, because of the photosensitivity of the first. From this figure an important result can be deduced: a second treatment at 750°C or at a lower temperature does not change any further the peak amplitude, if the grating is written in the F-doped fiber; for the grating written in the Ge-doped fiber the second treatment of only 45 min at 750°C causes a further reduction of the amplitude of about 10 %.

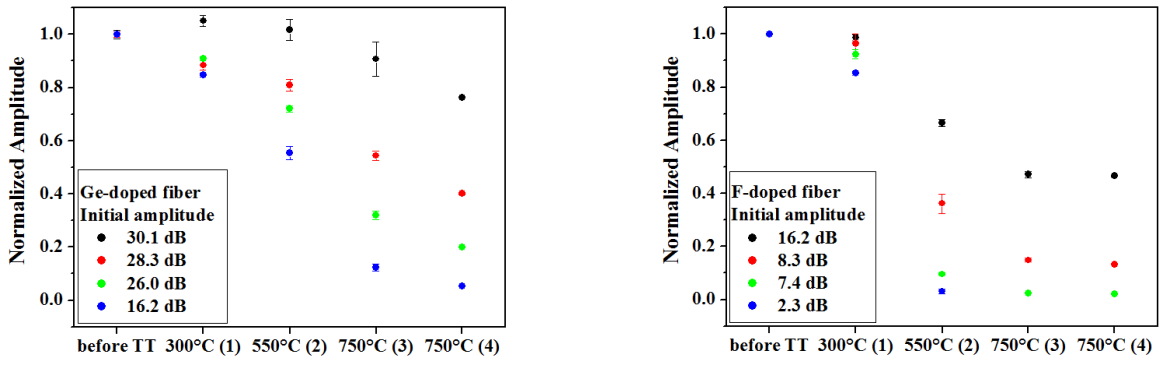

(a) (b)

Figure 5.3: Variation of the peak amplitude, normalized to the initial value, as a function of the annealing temperature, for gratings written in (a) the Ge-doped and (b) the F-doped fibers. The used laser power for these gratings is 500 mW.

Finally, the **FWHM** of the Bragg peak increases by increasing the laser power or the inscription time and it decreases with the thermal treatments, as shown in fig. 5.1(d). Its variation is dependent on the inscription parameters: the higher is the laser power or the initial amplitude, the larger is the variation.

This first study lets us make some conclusions about the best parameters for the inscription of a FBG suitable for a high temperature environment.

- The best value for the laser power among those used for our tests is the maximum, that is 500 mW: the gratings will be erased by the treatment at 750°C, if the laser power is too low.

- The inscription time has to be as long as possible to create a grating with a high initial strength but without deforming the peak shape: care must be taken not to cause too many losses in the cladding and not to saturate the peak, that should not have a top hat shape. Generally, the inscription time is about few minutes but it depends strongly on the alignment of the system.

The more inconvenient effect of these conditions is the larger Bragg peak blue-shift due to the thermal treatments. However, the results obtained by realizing two treatments at 750°C point out that the strength and the Bragg wavelength value at RT do not change anymore, if the grating has already undergone an annealing at a temperature higher than the application one. Moreover, if the grating is pre-treated at 750°C and, when using it, the temperature increases up to 750°C, that of the pre-treatment, the error on the temperature measurement will be less than 2°C, if the grating has been written in a F-doped fiber. In the same situation, the use of a Ge-doped fiber will cause a larger error, around 20°C.

Non linear temperature dependence of the Bragg wavelength

As mentioned before, the dependence of the Bragg wavelength on the temperature is almost linear. In fact, a linear function does not fit well the experimental data over a range of 800°C, as shown in fig. 5.4, where the residual wavelengths from the linear and the polynomial (second or third order) fits are plotted over all the temperature range. The deviation of the data from the linear fit depends on the temperature value in a parabolic way, whereas for the second order polynomial a part of the deviation data is all negative and the other part positive. The third order polynomial shows small deviations from the experimental data, less than 0.03 nm. This non-linear response of gratings over a large temperature range has been already reported by Hill and Meltz, that carried out studies up to 850°C [56].

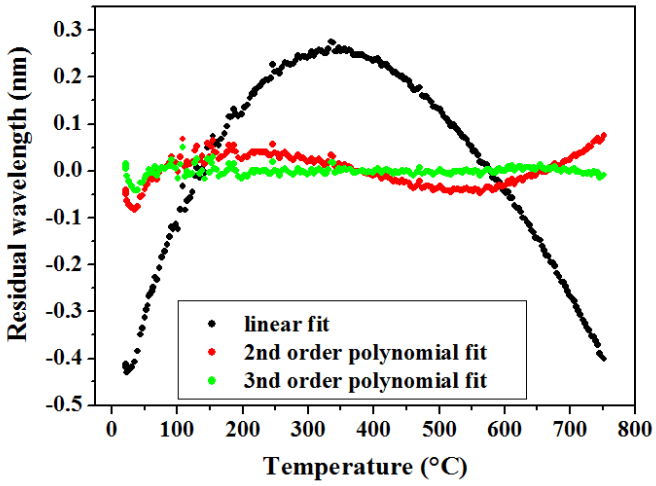

Figure 5.4: Comparison of the residual wavelengths for linear and the polynomial fits for the fs-FBG written in the F-doped fiber with laser power of 500 mW and initial amplitude of ∼16 dB, during the fourth treatment (T_f=750°C).

5.2 Effects of irradiation

The previous section highlights the non-stability at high temperature of the fs-FBG written in the Ge-doped fiber and pre-treated at 750°C for 15 min. As a consequence, these gratings are not good enough to be used as temperature sensors at high temperature and then for our application; this leads us to privilege the gratings written in the F-doped fibers for studies under radiation. However, some irradiation tests were carried out also for the gratings written in the Ge-doped fiber.

Irradiations were performed by the two X-ray Irradiators illustrated in section 4.4.1, with a dose rate of 50 Gy/s both at RT and at a higher temperature, ∼230 °C. At a time, more FBGs were fixed stress-free on the plate of the irradiation system and their transmission (or reflection) spectra were recorded in parallel by the high-performance set-up, with a wavelength resolution of 1 or 2 pm, for the FBGs written in the F-doped and in the Ge-doped fibers, respectively.

During the irradiations a temperature increase was observed, so to calculate the radiation-induced peak shift the temperature effect was compensated by subtracting the computed temperature-induced wavelength shift component, once the temperature sensitivity of the gratings is known. The temperature coefficient was calculated by varying the temperature in a range near the value held during irradiation and by realizing a linear fit on the BWS as a function of the temperature. For example, during these sensitivity tests the temperature was varied from 20°C to 60°C for the irradiation at RT and from 220°C to 240°C for those around 230°C. The following graphs will always show

the compensated values for the Bragg wavelength shift.

Germanium-doped fibers

Two gratings were written by the fs IR laser in the standard Ge-doped fiber, to easily compare the results with the literature. The gratings will be referred hereafter as fs-FBG-I and fs-FBG-II, because the laser power used during the inscription was increased from 300 mW to 870 mW, to have one grating of type I and the other of type II. The initial grating parameters are reported in table 5.1 and their transmission spectra are shown in fig. 5.5. Due to the high inscription laser power used for fs-FBG-II, a strong excitation of the cladding modes is observed; because of this, the FWHM value can not be properly measured. Both gratings did not undergo any thermal treatment before irradiation: since several works state that the temperature coefficient does not change within 10% because of the radiation [131], even the small temperature rise necessary to measure the sensitivity was realized only after irradiation. This coefficient is (10.85 ± 0.05) pm/°C, independently of the inscription laser power.

The irradiation was performed at RT, around 30°C, during $2 \cdot 10^4$ s up to an accumulated dose of 1 MGy, the dose-rate being 50 Gy/s. Fig. 5.6 shows the changes of the Bragg peak position, amplitude and width during the irradiation tests.

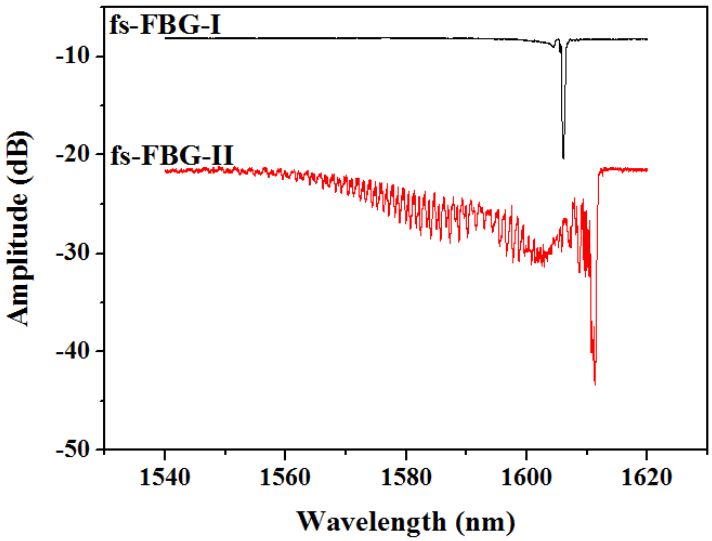

Figure 5.5: Transmission spectra of the two gratings written by the fs IR laser in the Ge-doped Std-SMF fiber, before irradiation. The black curve is referred to the fs-FBG-I and the red one to the fs-FBG-II.

As reported in fig. 5.6(a), during irradiation the BWS shows a non-monotonic behavior with the dose; two regimes can be discerned: a fast one for doses lower than 40 kGy,

Fiber	Sample	Laser power (mW)	Bragg peak wavelength (nm)	Bragg peak amplitude (dB)	FWHM (nm)
Std-SMF	fs-FBG-I		1606.034 ± 0.006	12.21 ± 0.02	0.567 ± 0.003
	fs-FBG-II		1611.262 ± 0.008	21.68 ± 0.06	/

Table 5.1: Parameters of the gratings before irradiation. For fs-FBG-II the FWHM value can not be determined, because the spectrum is too distorted.

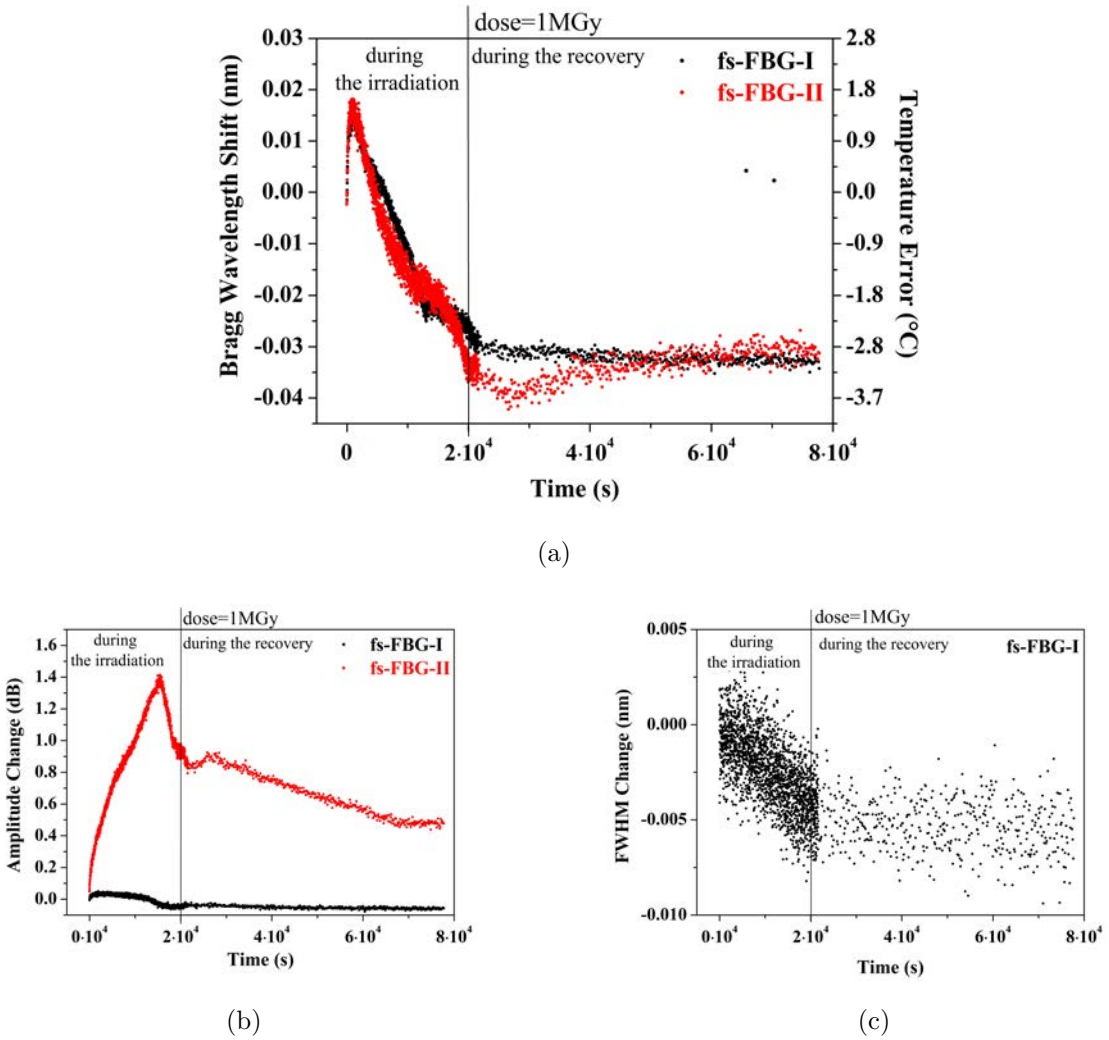

(a)

(b)

(c)

Figure 5.6: Gratings written by the fs laser in the Ge-doped fiber Std-SMF: evolution of the Bragg peak parameters as a function of the time from the irradiation start, during the irradiation up to the dose of 1 MGy and the recovery, both performed at RT. The vertical line indicates the end of the irradiation run. The black points are referred to fs-FBG-I, whereas the red ones to fs-FBG-II. In figure (a) the y-axis on the left indicates the radiation-induced error done by the grating if it works as a temperature sensors.

characterized by a red-shift up to 15 pm, and a slower one for higher doses, where the Bragg wavelength decreases without showing a saturating tendency at the maximal accumulated dose. This behavior does not depend on the inscription power, within an error of 6 pm (around 0.5°C). After irradiation, no significant recovery was observed and for the fs-FBG-II λ_{Bragg} initially continues to blue-shift further, by 5 pm. The error on the temperature measurement due to the radiation is within a range of 5°C.

The amplitude and the FWHM of the fs-FBG-I are rather not affected by the radiation: their decrease is around 1%. In contrast, the fs-FBG-II strength variation is around 6%: it increases up to the dose of 760 kGy and then it decreases, without recovering its initial value.

Fluorine-doped fibers

Two types of F-doped fibers were chosen for the irradiation tests: the *F-SMF1* and the *PCS-SMF*, characterized by a F-doped silica core and a pure silica core, respectively. For each fiber type, five gratings were written by the fs-laser with a power of 500 mW and an initial amplitude higher than 10 dB: one grating was not thermally treated, two were annealed at 350°C and the other two at 750°C. The values of the grating parameters before irradiation are reported in table 5.2, together with the used irradiation temperature. It would be useless to irradiate a not thermally treated grating at a temperature higher than RT, because both radiation and temperature will cause the grating degradation. The temperature sensitivity, obtained before irradiations, varies between 9 and 15 pm/°C and it decreases with increasing annealing temperature.

The X-ray irradiations were performed at RT, around 25°C, and at ∼230°C with a dose rate of 50 Gy/s. At each irradiation temperature, two runs with dose of 1.5 MGy were realized with a duration of $3 \cdot 10^4$ s, total dose being 3 MGy. For the gratings written in the pure silica core fiber, a further run at RT was realized with a duration of $2 \cdot 10^4$ s, for an additional dose of 1 MGy, in this case the total dose was 4 MGy.

Among all the parameters, the radiation-induced BWS is particular relevant, because it represents the error on the temperature measurement caused by the radiation. Fig. 5.7 shows its profile for all the gratings, thermally treated or not, during irradiation at RT.

For the *not thermally treated gratings* written in the two fibers (fig. 5.7(a) and 5.7(d)), λ_{Bragg} shifts towards shorter wavelengths: the first irradiation causes a larger shift for the F-doped core fiber than for the pure silica core fiber (0.06 nm against 0.02 nm at the 1.5 MGy dose). For the F-doped core fiber, the recoveries and the second irradiation produce a shift of about 0.02 nm towards the blue and the red, respectively. For the pure silica core fiber, the observed trend is more complicated but it is easy to note that the

Fiber	Thermal Treatment	Irradiation Temperature	λ_B (nm)	Bragg peak A (dB)	FWHM (nm)
F-doped core	/	RT	1539.736 ± 0.002	18.53 ± 0.02	0.577 ± 0.002
	350°C	RT	1539.610 ± 0.003	8.69 ± 0.02	0.47 ± 0.03
	750°C	RT	1539.298 ± 0.008	2.49 ± 0.12	0.39 ± 0.05
	350°C	230°C	1541.61 ± 0.06	7.51 ± 0.03 *	0.420 ± 0.009
	750°C	230°C	1542.080 ± 0.015	25.9 ± 0.3 *	∼2
Pure silica core	/	RT	1545.345 ± 0.014	12.00 ± 0.07	0.93 ± 0.02
	350°C	RT	1544.601 ± 0.004	12.00 ± 0.02	0.96 ± 0.02
	750°C	RT	1543.727 ± 0.002	1.600 ± 0.006	0.374 ± 0.007
	350°C	230°C	1549.98 ± 0.04	12.88 ± 0.06	0.86 ± 0.02
	750°C	230°C	1546.20 ± 0.02	1.400 ± 0.007	0.424 ± 0.014

Table 5.2: Parameters values of the gratings before irradiation. * These gratings were analyzed in reflection.

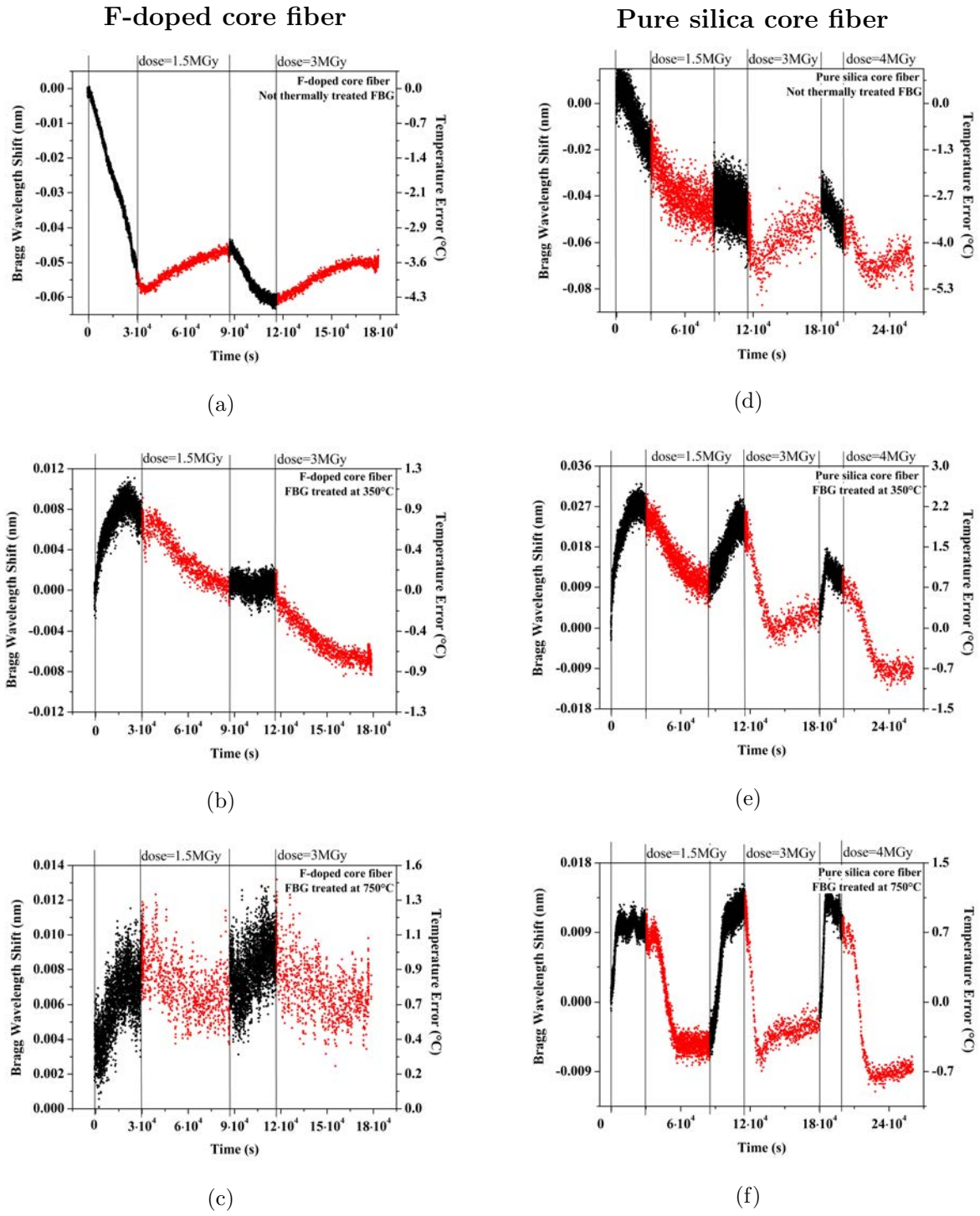

Figure 5.7: **Irradiation at RT**: Bragg wavelength shift, corrected with respect to the temperature variations, as a function of the time from the first irradiation start, for gratings written in (a, b, c) the F-doped core and (d, e, f) the pure silica core fibers. The black points are recorded during irradiations whereas the red ones during recoveries at RT. The vertical lines indicate the start and the end of the two (for the first fiber, on the left) or three (for the second fiber, on the right) irradiation runs. In the upper part of each graph the total dose reached after a run is shown, dose-rate being 50 Gy/s. The y-axis changes from a grating to another. The y-axis on the left indicates the radiation-induced error done by the grating if it works as a temperature sensors.

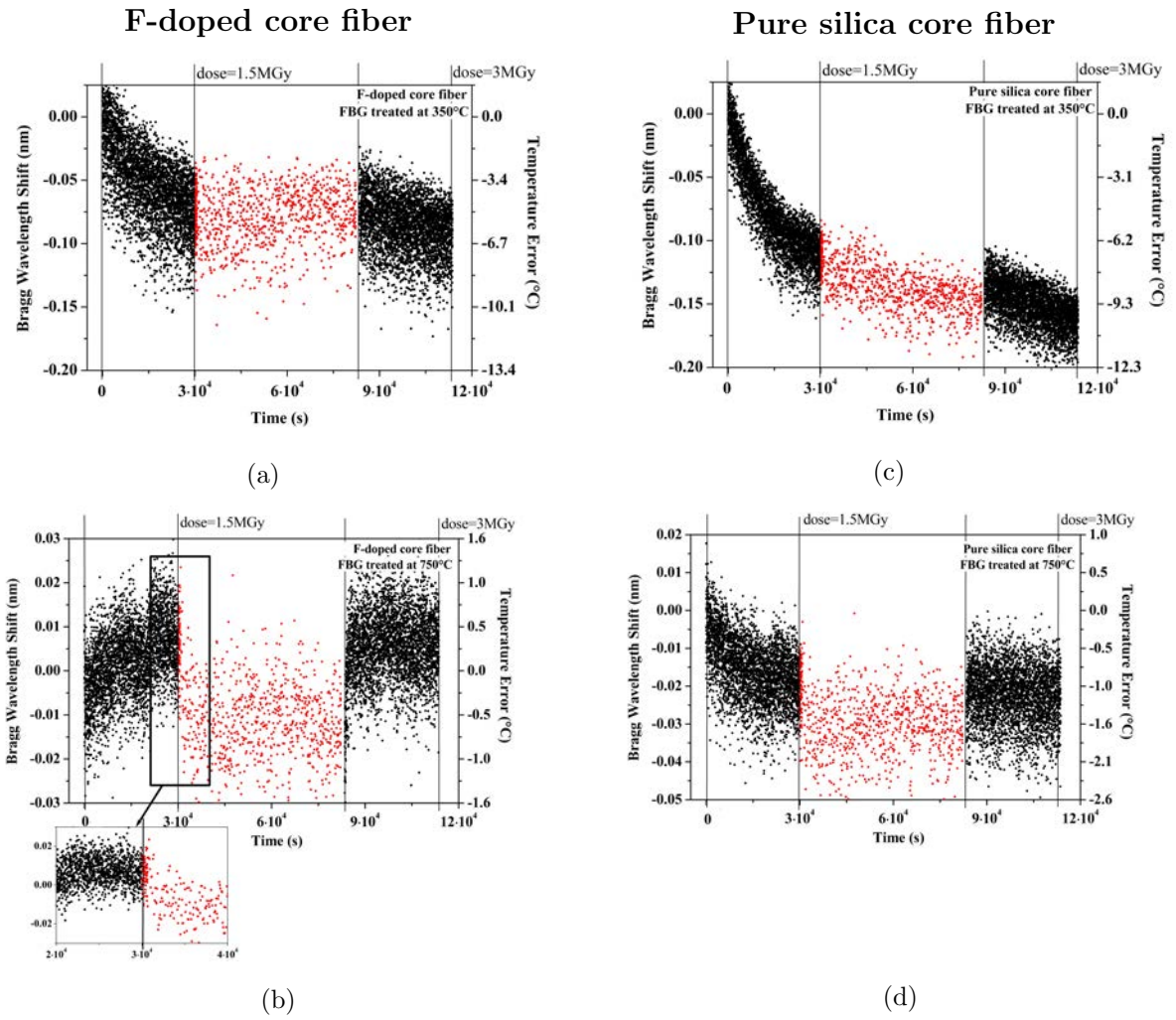

Figure 5.8: **Irradiation at T≈ 230°C**: Bragg wavelength shift, corrected with respect to the temperature variations, as a function of the time from the first irradiation start, for gratings written in (a, b) the F-doped core and (c, d) the pure silica core fibers. The black points are recorded during irradiations whereas the red ones during recoveries at $\sim$ 230°C. The vertical lines indicate the start and the end of the two irradiation runs. In the upper part of each graph the total dose reached after a run is shown, dose-rate being 50 Gy/s. The insert of the graph (d) shows a zoom of the BSW near the end of the first run. The y-axis on the left indicates the radiation-induced error done by the grating if it works as a temperature sensors.

second and third irradiations cause a further blue-shift lower than 0.02 nm. In both the fiber types, this shift of 0.02 nm corresponds to an error on the temperature measurement of about 1.5°C.

For the *gratings annealed at* $350°C$ (fig. 5.7(b) and 5.7(e)), during the first irradiation the BWS initially increases with the dose, then it reaches a maximum value, that is smaller for F-SMF1 than for PSC-SMF (8 pm against 27 pm), and it starts to decrease; during recovery it continues to decrease till 0 pm for the first fiber and 9 pm for the second. For F-SMF1, the second irradiation run does not change λ_{Bragg}, probably because the radiation and the recovery effects compensate. For PSC-SMF, a pre-irradiation improves the grating response, indeed the first 1.5 MGy increase the Bragg wavelength by 27 pm, the second additional 1.5 MGy increase the BWS from 9 pm to 27 pm, whereas the BWS due to the last run of 1 MGy dose is smaller than 18 pm, that corresponds to 1.5°C. Moreover, it can be highlighted that during the last run the Bragg peak reaches the maximum red-shift quickly, at the dose of only 0.3 MGy.

For the *gratings annealed at* $750°C$ (fig. 5.7(c) and 5.7(f)), the Bragg peak red-shifts during irradiation and it blue-shifts during recovery. For the F-doped core fiber, the peak wavelength increases by 12 pm at the total dose of 3 MGy, this corresponds to an error on the temperature measurement of 1°C. Instead, the grating written in the pure silica core fiber shows a saturating BWS behavior at doses of about 0.3 MGy and the maximum temperature error that can be done during all the irradiations is also in this case about 1°C.

For the irradiations at higher temperature, held at 230°C during all the experiment, the compensated Bragg wavelength shift is shown in fig. 5.8.

For the *gratings annealed at* $350°C$ (fig. 5.8(a) and 5.8(c)), the Bragg wavelength decreases during irradiation: after a 3 MGy dose, the maximum shift is around 0.2 nm that means a temperature error due to the radiation of about 10°C. This value is one order of magnitude bigger than in the case of the irradiations at RT. Fig. 5.8(c) highlights that for the grating written in the pure silica core fiber the Bragg peak continues to shift towards the blue during the recovery at 230°C after the first run: this suggests that the thermal treatment is still erasing the grating, so the pre-annealing at 350°C was not enough to stabilize the FBG for an use of two days at 230°C.

For the *gratings annealed at* $750°C$ (fig. 5.8(b) and 5.8(d)), the Bragg wavelength shows a saturating tendency: it does not change anymore after the first run at a dose of 1.5 MGy. During the recovery the peak blue-shifts quickly of about 20 pm (as shown in the inset of fig. 5.8(b)), whereas at the start of the second irradiation run it red-shifts by the same quantity. This shift can not be associated with a temperature change due to

the irradiation light-on or -off, because the BWS was already corrected with respect to these variations. The total shift is always within 30 pm, towards the red or the blue for F-SMF1 and PSC-SMF, respectively. The error on the temperature due to the radiation is lower than 1.5°C. In contrast to the graphs of fig. 5.7, the data in fig. 5.8 possess a significant noise and this causes an uncertainty on the temperature measurement of about (0.5-1)°C. It can be guessed that the origin of this noise is the compensation: the temperature measurements are subjected to random errors and the correction for the temperature variation increases the noise of the BWS.

5.3 Discussion and comparison with the literature

Gratings in Ge-doped fibers

As reported in Chapter 3, very few publications deal with the radiation sensitivity of gratings written with femtosecond IR lasers. For both the type I and the type II gratings written in the standard Ge-doped fiber, it was observed a BWS increase up to ∼15 pm at 100 kGy followed by a slower decrease of ∼8 pm up to 1 MGy dose [66, 131]. A similar evolution under radiation was observed for our samples: no significant difference between the type I and the type II gratings and an initial BWS increase, up to 15 pm at 40 kGy dose, followed by a decrease, which is more important in our case, about 0.05 pm/kGy. This difference can be due to the different conditions: the dose-rate used in our experiment was higher, 50 Gy/s against 1-2 Gy/s, and our gratings were not thermally treated. As stated in literature, the lower dose-rate should decrease the BWS values [126]; however, the exposure to higher temperatures should increase the grating radiation sensitivity [120].

The cause of this blue-shift is not clarified yet. In order to make some hypothesis about its origin, a comparison with a grating written by the cw UV laser in the hydrogenated Std-SMF[1] is reported in the following. Fig. 5.9 shows the peak shift during the X-ray irradiation at RT for the gratings written in the standard Ge-doped fiber by the cw UV and the fs IR laser, UV-FBG and fs-FBG-I, respectively. The UV-FBG shows a red-shift, whereas the fs-FBG-I is mainly characterized by a blue-shift.

From the definition of λ_{Bragg}, reported in Eq. 2.15, it is can be found that:

$$\frac{\Delta\lambda_{Bragg}}{\lambda_{Bragg}} = \frac{\Delta n_{eff}}{n_{eff}} + \frac{\Delta\Lambda}{\Lambda} \tag{5.3}$$

If only the dependence on n_{eff} is taken into account, the red-shift (the blue shift) means an increase (a decrease) of the average effective index, which can be explained with

[1] H_2-loading at 130 mbar and RT, for a week, followed by a thermal treatment at 80°C for 7 h.

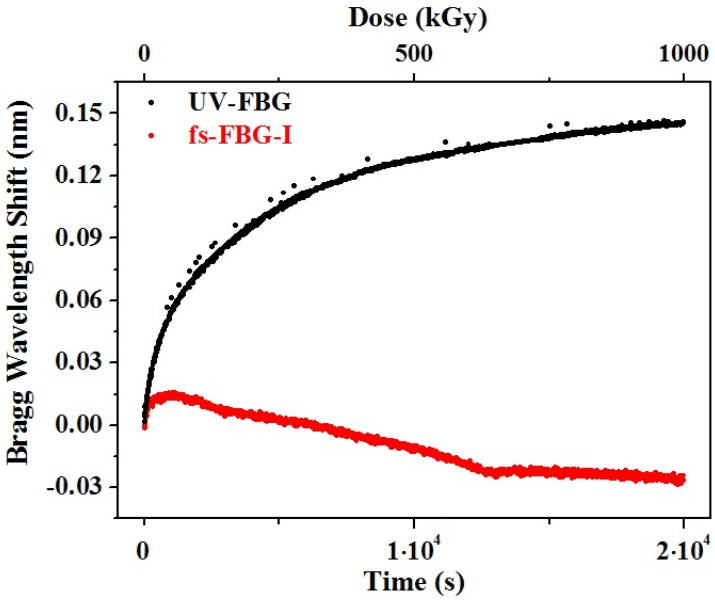

Figure 5.9: Evolution of the Bragg wavelength shift as a function of the time from the irradiation start, or the dose, the dose rate being 50 Gy/s, during irradiation at RT, up to 1 MGy dose. The gratings have been written in the Std-SMF Ge-doped fiber, the UV-FBG (black points) by the cw UV laser, whereas the fs-FBG-I (red points) by the fs IR laser.

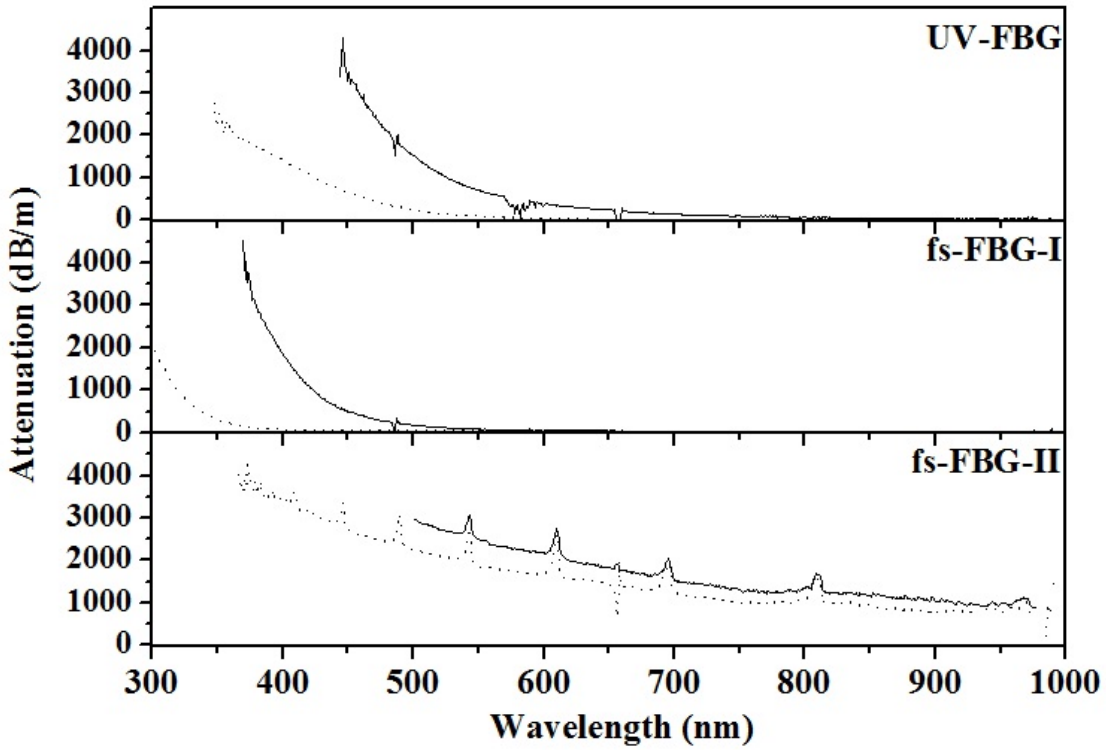

Figure 5.10: Attenuation spectra of the three FBGs written in the Std-SMF Ge-doped fiber, before (dotted line) and after (continuous line) irradiation.

the Kramer-Krönig relation as a consequence of an increase (a decrease) of absorption at shorter wavelengths, the UV-Vis region of the spectrum. To verify this hypothesis, attenuation spectra on the gratings were measured at RT before and after irradiation, using the cut-back technique (see section 4.3.1), and they are reported in fig. 5.10: for all the gratings the radiation causes an increase of the attenuation. Generally, in a fiber the scattering losses can be neglected with respect to the absorption, above all in the UV-Vis range, and the attenuation spectrum can be considered coincident with the absorption one. When a grating is written inside the fiber, the light is reflected and scattered at each refractive index variation: for example, for the fs-FBG-II, the attenuation spectra show all the other orders of λ_{Bragg} and the background around 10^3 dB/m is due to the scattered light. All these spectra let us deduce that the absorption in the UV-Vis range should increase or at most remain unchanged. As a consequence, a blue-shift of the Bragg peak can be explained not with a decrease of n_{eff} but by a Λ reduction, due to a compaction. If Δn_{eff} is neglected, an underestimation of the compaction can be obtained:

$$\frac{\Delta\Lambda}{\Lambda} \sim \frac{\Delta\lambda_{Bragg}}{\lambda_{Bragg}} \sim \frac{-0.03\,\text{nm}}{1606\,\text{nm}} \sim -2 \cdot 10^{-5} = -20\mu\epsilon \tag{5.4}$$

that entails a compaction $\frac{\Delta\rho}{\rho}$ of about 10^{-14}, that is too low to be experimentally verified with other techniques yet.

Gratings in F-doped fibers

For the not pre-treated gratings, the evolution of the BWS under radiation observed in the F-doped fibers is very similar to that observed in the Ge-doped one, except for the lack of the first fast red-shift regime: the Bragg peak blue-shifts directly from the irradiation start. However, the slope of the blue-shift is larger for the Ge-doped FBG than for the Ge-free FBGs, by a factor ∼2 (-0.05 pm/kGy against -0.03 pm/kGy for the F-doped core fiber and -0.02 pm/kGy for the pure silica core fiber).

A surprising result is obtained for the pre-treated gratings. In literature it stated that an exposure to higher temperature increases the grating radiation sensitivity, because defects created during the grating inscription are annealed at high temperature and can be generated again by the ionizing radiation. This was observed for gratings written both by UV lasers [116, 120] and fs lasers [131]. Our results suggest that a pre-annealing enhances the radiation-resistance of gratings: for example, for the F-doped core fiber the BWS due to the only first 1.5 MGy irradiation run decreases from ∼50 pm, without treatments, to ∼8 pm for the treated gratings. Moreover, the annealing changes the BWS direction from the blue to the red.

In conclusion, we focused our attention on the gratings written with the femtosecond radiation at 800 nm, in particular in F-doped fibers.
The thermal response of the gratings depends strongly on the inscription conditions. If the laser power is lower than 450 mW (power density in front of the PM lower than 1.5 kW cm^{-2}) or the inscription time is shorter than 30 s, the gratings will be erased by a treatment at 750°C, necessary for their stabilization. Our studies showed that a laser power of 500 mW (power density in front of the PM around 1.7 kW cm^{-2}) and an initial amplitude larger than 10 dB are good conditions to write a grating having good characteristics. Otherwise, a pre-treatment at a temperature higher than that of the application stabilizes the FBG. However, if the application temperature reaches that of the pre-treatment, 750°C in our case, the induced blue-shift causes an error on the temperature measurement of about 2°C for a grating written in a F-doped fiber and of about 20°C for a grating written in a Ge-doped fiber.
Regarding the grating response under radiation, it does not depend strongly on the inscription conditions for the fs-FBGs. In contrast, the thermal pre-treatment is crucial. For the FBG written in F-doped fibers, the Bragg peak blue-shifts directly from the irradiation start for non pre-treated gratings, whereas it starts shifting towards the red for the gratings that undergo a thermal treatment before irradiation. The pretreatment is essential for the grating stabilization and radiation-resistance: the radiation-induced error on the temperature measurement decreases from 5°C, for the non treated sample, to about 3°C for the gratings treated at 350°C and down to 1.5°C for the samples annealed at 750°C.

Dans ce chapitre, nous avons principalement présenté les résultats relatifs aux réseaux inscrits par laser à impulsion femtoseconde à 800 nm, en particulier dans les fibres dopées au fluor.
La réponse thermique des réseaux dépend fortement des conditions d'inscription. Si la puissance du laser est faible (densité de puissance avant le masque de phase inférieure à 1.5 kW cm^{-2}) ou le temps dinscription est court (inférieur à 30 s), les FBG sont effacés par le traitement à 750°C, nécessaire pour leur stabilisation. Nos études ont montré qu'une puissance de 500 mW (densité de puissance avant le masque de phase de l'ordre de 1.7 kW cm^{-2}) et une amplitude initiale supérieure à 10 dB constituent de bonnes conditions pour obtenir un FBG présentant de bonnes caractéristiques. Par ailleurs, un prétraitement à une température plus élevée que celle de l'application stabilise le FBG. Cependant, si la température de l'application atteint celle du prétraitement, 750°C dans notre cas, on assiste à un décalage vers le bleu causant une erreur sur la mesure de température de ∼2°C pour un réseau inscrit dans une fibre dopée au fluor et d'environ 20°C pour un réseau inscrit dans une fibre dopée au germanium.
En ce qui concerne la réponse des réseaux sous radiation, les réseaux inscrits par laser à impulsion femtoseconde ne présentent pas une forte dépendance aux conditions d'inscription. En revanche, le prétraitement thermique est déterminant. Pour les réseaux de Bragg inscrits dans la fibre dopée au fluor, le pic de Bragg se décale vers le bleu dès le début de l'irradiation pour les réseaux non traitées thermiquement, alors qu'il commence par se décaler vers le rouge pour les réseaux prétraités. Le prétraitement est aussi primordial pour la stabilisation et l'immunité des FBG vis-à-vis des radiations ; l'erreur associée à l'irradiation pour la mesure de la température passe de 5°C, pour l'échantillon non prétraité, à environ 3°C pour les réseaux prétraités à 350°C et à 1.5°C pour les échantillons prétraités à 750°C.

In questo capitolo abbiamo focalizzato la nostra attenzione sui reticoli iscritti con la radiazione al femtosecondo a 800 nm in fibre drogate con fluoro.
La risposta termica dei reticoli dipende fortemente dalle condizioni d'iscrizione. Se la potenza del laser è bassa (densità di potenza prima della maschera di fase inferiore a 1.5 kW cm^{-2}) o il tempo d'iscrizione è breve (inferiore a 30 s), i reticoli vengono rimossi dal trattamento a 750°C, necessario per la loro stabilizzazione. I nostri studi hanno mostrato che una potenza del laser di 500 mW (densità di potenza prima della maschera di fase dell'ordine di 1.7 kW cm^{-2}) e una ampiezza iniziale maggiore di 10 dB costituiscono delle buone condizioni per ottenere un FBG con delle buone caratteristiche. Inoltre, un pre-trattamento ad una temperatura superiore a quella dell'applicazione stabilizza il FBG. Tuttavia, se la temperatura dell'applicazione raggiunge quella del pre-trattamento, 750°C

nel nostro caso, il blu-shift indotto causa un errore sistematico sulla misura della temperatura inferiore ai 2°C, se il reticolo è stato iscritto in una fibra drogata con fluoro, e di circa 20°C in una fibra drogata con germanio.
Per quanto riguarda la risposta del reticolo sotto irraggiamento, essa non dipende fortemente dalle condizioni d'iscrizione, per i reticoli iscritti con la radiazione al femtosecondo. Tuttavia, il pre-trattamento termico è determinante. Per i FBG iscritti in fibre drogate con il fluoro, il picco di Bragg si sposta verso il blu dall'inizio dell'irraggiamento, se non sono pre-trattati, mentre esso inizia a spostarsi verso il rosso, se i reticoli subiscono un trattamento termico prima dell'irraggiamento. Il pre-trattamento è fondamentale per la stabilizzazione dei reticoli e la resistenza alla radiazione: l'errore associato alla misura di temperatura diminuisce da 5°C, per il campione non trattato, a circa 3°C per i reticoli trattati a 350°C, fino a meno di 1.5°C per i campioni pre-trattati a 750°C.

Chapter 6

Spectroscopic characterization

This chapter reports the main results obtained for the radiation effects on the transmission properties of optical fibers doped with fluorine and/or germanium. The origin of the attenuation was studied decomposing the RIA spectra as a sum of Gaussian curves and investigating the photoluminescence emission, whereas the EPR technique allows us to observe the paramagnetic defects.

6.1 Fluorine doped fibers

In this section dealing with the F-doped fibers, the results obtained on F-SMF1 and F-MMF1, unless noted otherwise, will be shown: same conclusions can be realized for all the other F-doped fibers. All the fibers were irradiated with γ-rays or neutrons at different doses.

6.1.1 RIA and its origin

Under γ-radiations, the RIA spectra of the multi- or single-mode fibers made of F-doped silica are displayed in fig. 6.1. These curves show the same trend and consist of at least three contributions:

- an UV-absorption tail which increases with decreasing wavelength,
- an absorption band in the visible range, around 620 nm,
- an IR-absorption which increases for wavelengths longer than 900 nm.

Despite the spectra missing part, due to the range of the two detectors, it is evident that the RIA curves have a minimum around 900 nm. Moreover, for the single-mode fiber, an absorption band around 1400 nm seems present, in fact the IR part of this spectrum has

to be considered as an upper limit, because it is influenced by the fiber bending losses. This problem does not come up for multi-mode fibers.

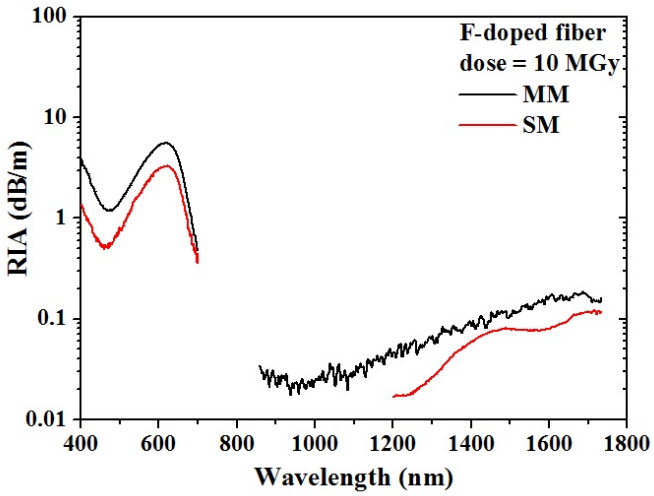

Figure 6.1: RIA spectra of the γ-irradiated F-doped multi- (black curve) and single-mode (red curve) fibers at 10 MGy.

The RIA increases with increasing irradiation dose, as shown in fig. 6.2, whereas fig. 6.3 displays the post-irradiation thermal treatment effects: the absorption bands induced by the radiation decrease their amplitude with increasing annealing temperature.

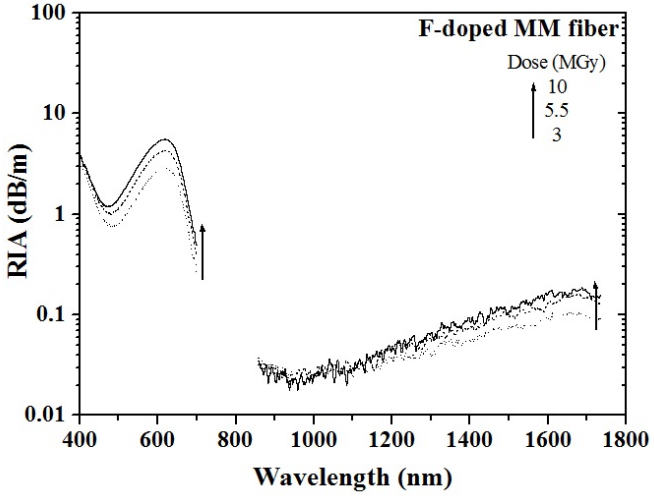

Figure 6.2: RIA spectra of the γ-irradiated F-doped multi-mode fibers at different doses: 3, 5.5 and 10 MGy.

In the visible range (fig. 6.3(a)), the absorption band at 620 nm is completely annealed after the thermal treatment at 550°C, whereas the UV tail amplitude is only slightly reduced by the treatment, indeed the residual attenuation at the wavelength of 400 nm

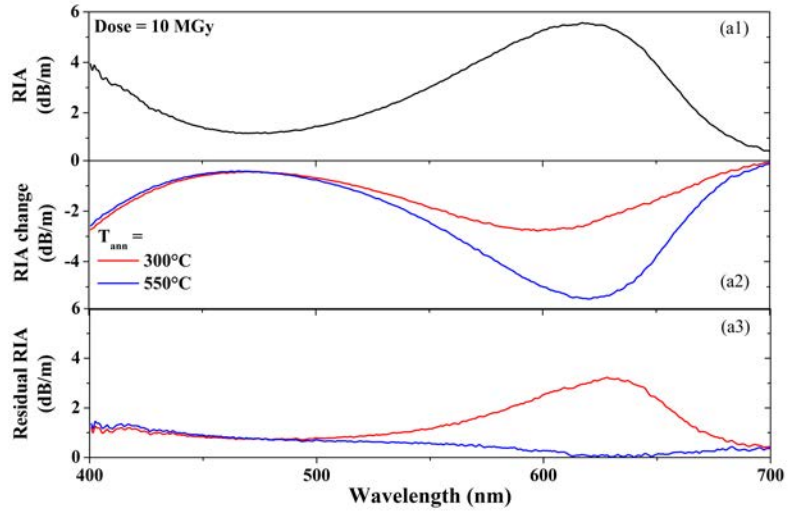

(a) Visible range

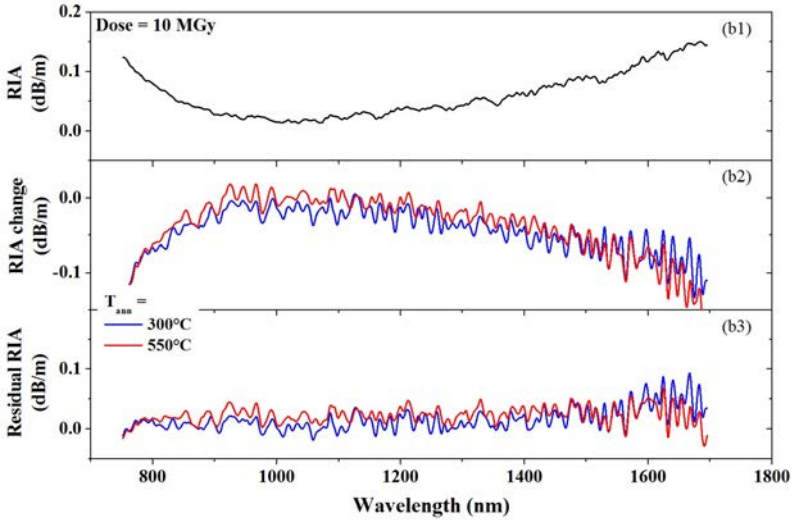

(b) IR range

Figure 6.3: All the spectra are referred to the 10 MGy irradiated F-doped multi-mode fiber: (a1-b1) RIA spectrum obtained with the cut-back technique, (a2-b2) RIA changes induced by the thermal treatments at 300°C (red line) and 550°C (blue line), (a3-b3) Residual RIA after the thermal treatments, obtained as the sum of the curve reported in (a1-b1) and in (a2-b2). The thermal treatment at 750°C causes no further change, so the curves are not shown.

is still around 1 dB/m. In the IR range (fig. 6.3(b)), it is the treatment at 300°C that reduces the attenuation at 0 dB/m, within the experimental uncertainty.

The limited range of the detector lets record only a tail of the IR band, so it is meaningless to fit this curve with a Gaussian function. In literature, a NIR-band peaked at a wavelength longer than 1500 nm and observable only at low temperatures, up to 160 K, is attributed to STH defects by Chernov et al. [150]. Even if it is known that STHs are unstable at RT, Regnier et al. [151] supposed to associate with these defects their NIR-band peaked around 1800 nm (∼0.7 eV, FWHM = 0.3 eV) and observed at RT in a pure silica core fiber γ-irradiated at an accumulated dose of 100 Gy. According to the authors, these defects were observable at RT thanks to their high measurement sensitivity obtained by using several km long fibers.

Also the origin of the absorption around 620 nm (2 eV) is still debated: one of the main questions concerns its assignment to a single or more defects. Under the hypothesis that more components overlap around 620 nm [152], the RIA spectra of fig. 6.2 were analyzed as a sum of three Gaussian curves. The absorption below 450 nm (above 2.8 eV), due to all the defects absorbing in the UV region, is accounted for by another Gaussian centered around 225 nm (∼5.5 eV).

Fig. 6.4 displays the decomposition of the RIA spectrum of the 10 MGy irradiated fiber; the spectral parameters are listed in table 6.1.

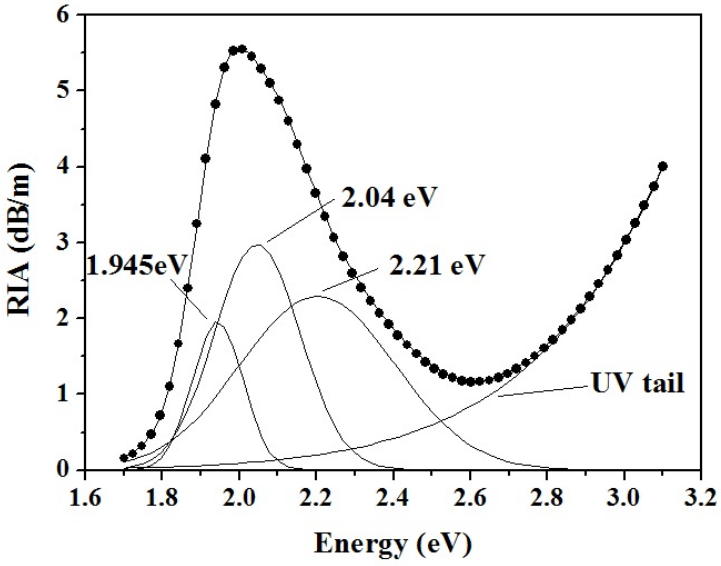

Figure 6.4: Decomposition into Gaussian bands of the RIA spectrum of the 10 MGy irradiated F-doped multi-mode fiber: measured spectrum (dots) and fitted curve (lines).

Band	Position (eV)	FWHM (eV)
1	1.945 ± 0.004	0.161 ± 0.011
2	2.04 ± 0.05	0.27 ± 0.08
3	2.21 ± 0.05	0.46 ± 0.06

Table 6.1: Spectral parameters of the bands used for the decomposition of all the OA spectra recorded in F-doped fibers irradiated at 3, 5.5 and 10 MGy. The error accounts for half of the maximum deviation.

These results, derived from the fitting, agree with previous studies on thermally treated F-doped samples, both fibers and bulks. Griscom and Mizuguchi have attributed a band centered at 1.97 eV with FWHM of 0.18 eV to PORs, a band at 2.08 eV with FWHM of 0.3 eV to NBOHCs induced by the H removal from SiOH groups and a band at 2.19 eV with FWHM of 0.5 eV to NBOHCs produced by the radiolysis of Si-O bonds [152].

However, some findings weaken this model, in favor of a 'single-defect' model, considering only the NBOHC. Firstly, the absorption band shape is independent of the radiation dose, consequently the generation rate under radiation of the three defects should be exactly the same. Secondly, the OH concentration is not high enough (∼0.2 ppm) to justify the 2.04 eV band intensity, associated with the NBOHCs deriving from the SiOH groups, compared to the 2.21 eV component, due to the NBOHCs produced by the Si-O bond rupture, as shown in fig. 6.4. Thirdly, the 2 eV absorption is completely annealed at 550°C, as pointed out in fig. 6.3(a), consequently it seems unlikely a model containing an absorption band due to the PORs, whose annealing is completed around 700°C [153]. But the most important evidence is given by PL measurements obtained with the Confocal Microscopy Luminescence setup. It is known that NBOHC is characterized by an asymmetric luminescence band at ∼1.9 eV that can be excited through all its absorption bands, peaked around 2, 4.8 and 6.8 eV [137]. So, it is possible to study the correlation of the absorption band at 2 eV with NBOHC through this PL: fig. 6.5 highlights the linear correlation between this absorption and the PL intensity emitted from all the fiber-transverse-surface at 1.9 eV under the laser excitation at 3.82 eV, which falls in the tail of the PLE spectrum of the NBOHC. The pristine fiber shows a weak 1.9 eV emission, whose intensity agrees with an absorption lower than the experimental uncertainty (0.10 dB/m).

In conclusion, the identification of the 1.9 eV emission with the NBOHC entails that only this defect is the origin of the 2 eV absorption. This hypothesis has been already advanced in previous studies: for instance, Cannas et al. observed an asymmetric absorption band peaked at 2.01 eV with a FWHM of 0.44 eV in γ- and β-irradiated synthetic wet silica samples and they associated it with NBOHCs thanks to its linear correlation with the 1.9 eV PL [154].

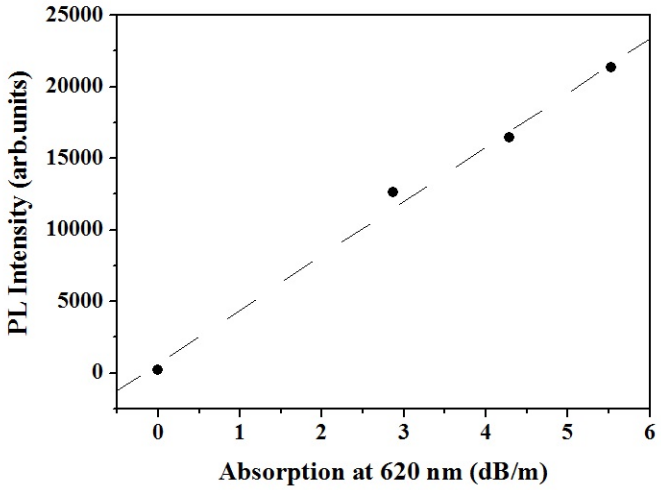

Figure 6.5: PL intensity emitted from all the fiber-transverse-surface at 1.9 eV under excitation at 3.82 eV, as a function of the optical absorption at 2 eV for pristine, 3, 5.5 and 10 MGy irradiated fibers. The dashed line is the fitted straight line (correlation coefficient R = 0.997).

6.1.2 Spectroscopic characteristics of Si-NBOHCs in fibers

Most of the PL studies about NBOHCs were realized in silica bulk samples; in contrast, its spectroscopic characteristics were poorly investigated in fibers [155]. So, in this section a methodical study on the spectral and decay features of the NBOHC in fibers will be presented.

The radiation and annealing effects on the *PL band shape* are reported in fig. 6.6: because of the radiation the peak red-shifts from 1.92 to 1.90 eV while the FWHM increases from 0.15 to 0.17 eV; on the other hand, the thermal treatment causes the opposite effects.

Fig. 6.7 displays an example of the 1.9 eV *PL decay*, obtained carrying out time resolved PL spectra on increasing T_D up to 90 μs with Δt ranging between 1 and 4 μs (see section 4.3.3). It agrees with a stretched exponential, $\exp(-(t/\tau)^{\beta})$, characterized by a lifetime $\tau = (11 \pm 1)$ μs and a stretching parameter $\beta = 0.81 \pm 0.07$. Moreover, it was observed that these decay features remain unchanged regardless the excitation energy both in the visible ($\sim$2.0 eV) and in the UV ($\sim$4.8 eV), the irradiation or the thermal treatments.

Finally, fig. 6.8 displays the *excitation profile* obtained by monitoring the peak emission intensity under laser excitation photon energy ranging from 1.7 to 2.3 eV. Both in the pristine and in the irradiated samples, the visible excitation shows an asymmetric band centered at (1.95 $\pm$ 0.02) eV with FWHM of (0.16 $\pm$ 0.02) eV.

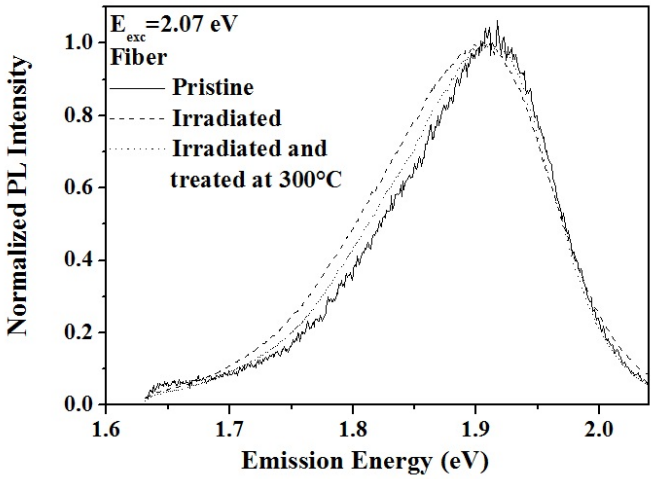

Figure 6.6: PL spectra recorded, with the time-resolved setup using the transverse excitation, on the pristine fiber (continuous line), that irradiated up to 10 MGy before (dashed line) and after the treatment at 300°C (dotted line). The laser excitation energy was 2.07 eV (600 nm) and the temporal parameters were fixed: $T_D = 1$ μs and $\Delta t = 10$ μs.

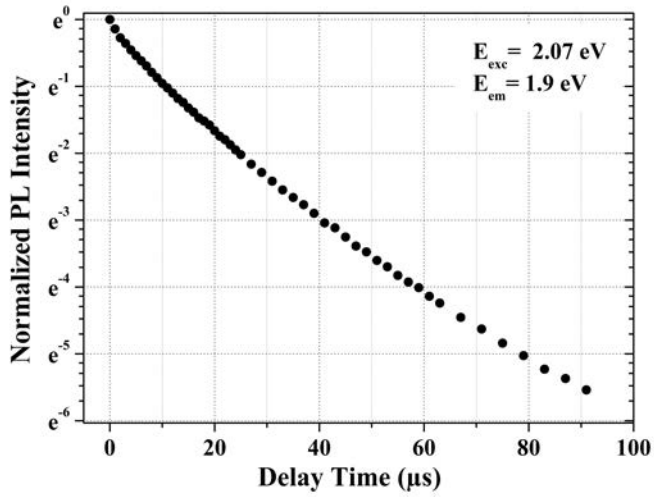

Figure 6.7: Semilog plot of the PL decay measured at 1.9 eV in the 10 MGy irradiated sample excited at 2.07 eV.

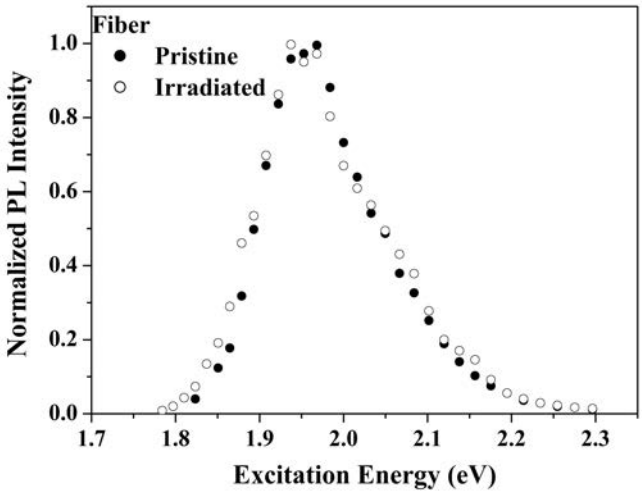

Figure 6.8: Visible-excitation spectra of the PL at 1.9 eV measured with T_D = 1 μs and Δt = 10 μs in the pristine (full circles) and the 10 MGy irradiated sample (empty circles).

All the spectral and decay features evidenced by time-resolved PL experiments support that the defect emitting at 1.9 eV in the F-doped fibers is the NBOHC. However, from a spectroscopic viewpoint, the acceptance of this single-defect model seems to be in contradiction with the different shapes of the absorption and PLE bands. It is known that the asymmetric PL and PLE spectra are accounted for by the weak electron-phonon coupling, characteristic of the NBOHC. As a consequence, these bands can be described by a Pekarian curve, which is the convolution of a Gaussian and a Poissonian and, under the straightforward model of coupling with a single mode having a mean Huang-Rhys factor S and an effective frequency ω, the lineshape $I(E)$ can be approximated by the function [156]:

$$I(E) \propto \sum\nolimits_n \mathrm{e}^{-S} \frac{S^n}{n!} \exp\left[-\frac{(E - E_{00} \pm n\hbar\omega)^2}{2{\sigma_{inh}}^2}\right] \tag{6.1}$$

valid at temperature sufficiently low in order not to populate the higher vibrational levels, that is $K_B T \ll \hbar\omega$. The signs + and − refer to the PL and PLE lineshape, respectively. Because of the glass disorder, the pure electronic transition between the lowest vibrational levels of the first excited and ground states is inhomogeneously distributed in agreement with a Gaussian curve, peaked at E_{00} with $FWHM_{inh} = 2\sqrt{2\ln(2)} \cdot \sigma_{inh}$.

We used the equation 6.1 to best fit the PL and PLE curves measured in the irradiated sample, as shown in fig. 6.9, and we got S = 1.3 ± 0.3, $\hbar\omega$ = (0.053 ± 0.009) eV,

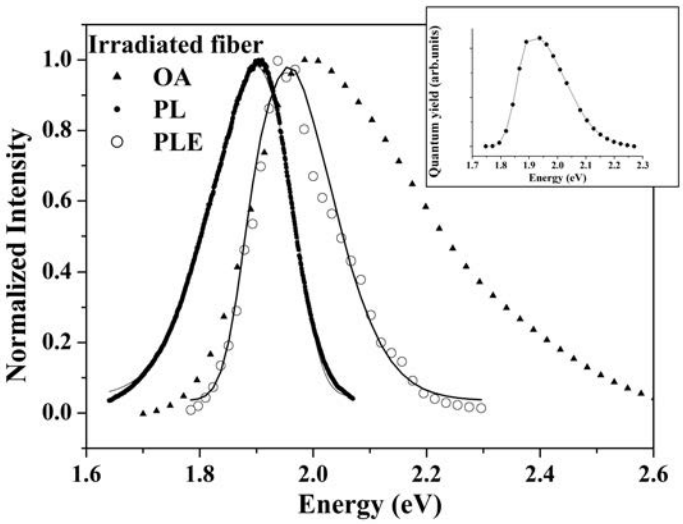

Figure 6.9: Normalized PL, PLE and OA spectra of the sample irradiated at 10 MGy. Solid curves represent the best-fitting functions (Eq. 6.1). The inset shows the quantum yield calculated as the ratio between PLE and absorption.

$E_{00} = (1.93 \pm 0.01)$ eV and $FWHM_{inh} = (0.082 \pm 0.002)$ eV. We note that our spectra are detected at room temperature and $\hbar\omega \sim K_B T$, this introduces a further Gaussian broadening adding to the inhomogeneous one [157], that could be therefore overestimated by our fit procedure. In fact, $FWHM_{inh}$ has been measured in previous works based on site selective luminescence [158] and it varies between 0.071 and 0.086 eV, depending on the irradiation history.

As concerns the absorption spectrum, its band shape is much wider than the PLE one. Under the assumption that it is completely due to NBOHC, the ratio between PLE and absorption curves is proportional to the quantum yield and it results in a photon energy dependent curve, as shown in the inset of fig. 6.9, thus suggesting that there are absorbing NBOHCs with non-radiative emission.

6.1.3 Spatial distribution of NBOHCs in fibers

Thanks to the Confocal Microscopy Luminescence setup, the NBOHC concentration profile along the fiber diameter was studied. PL spectra were recorded using the laser excitation at 3.82 eV. Fig. 6.10 reports the PL intensity at 1.9 eV normalized to that emitted from the core center, in the pristine and the 10 MGy irradiated multi-mode fiber. Both the fiber fabrication process, as the drawing [159], and the radiation create NBOHCs: the lower is the F content, the higher is the defect concentration; moreover,

the NBOHC profile is wider in the irradiated fiber than in the pristine one and it does not change with increasing dose.

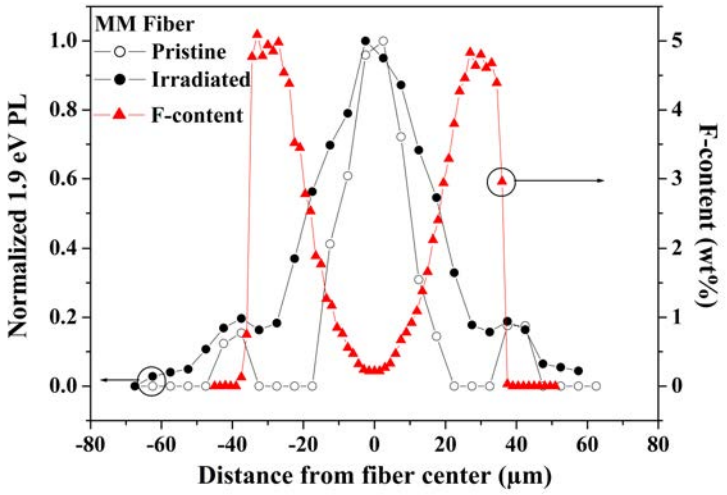

Figure 6.10: NBOHC profile detected through the 1.9 PL band on the pristine and irradiated MM fiber and F concentration profile obtained with the EMPA technique. The PL spectra were performed with the CML setup, under excitation at 3.82 eV, using a 40× objective and a diaphragm diameter of 75 μm, for a spatial resolution of ∼5 μm.

The semi-logarithmic scale of fig. 6.11 points out the anticorrelation existing between the NBOHC concentration and the F content; the concentration of both the drawing and irradiation induced defects decays exponentially with the F content, according the following equation [160]:

$$[NBOHC] \propto \exp\left(-\left[F\right]/\left[F_0\right]\right) \tag{6.2}$$

where $[F_0]$ is the F content at which the NBOHC concentration decreases by a factor of e.

From the derivative of Eq. 6.2,

$$\frac{\mathrm{d}\left[NBOHC\right]}{\left[NBOHC\right]} = -\frac{\mathrm{d}\left[F\right]}{\left[F_0\right]} \tag{6.3}$$

it is evident that the generation rate decreases on increasing the defect concentration or the F content and it depends also on the generation process through the coefficient $1/[F_0]$: it can be thought as the reduction of the effective volume for the defect formation and it is ∼1.3 $(\mathrm{wt}\%)^{-1}$ for the drawing and ∼0.4 $(\mathrm{wt}\%)^{-1}$ for the irradiation.

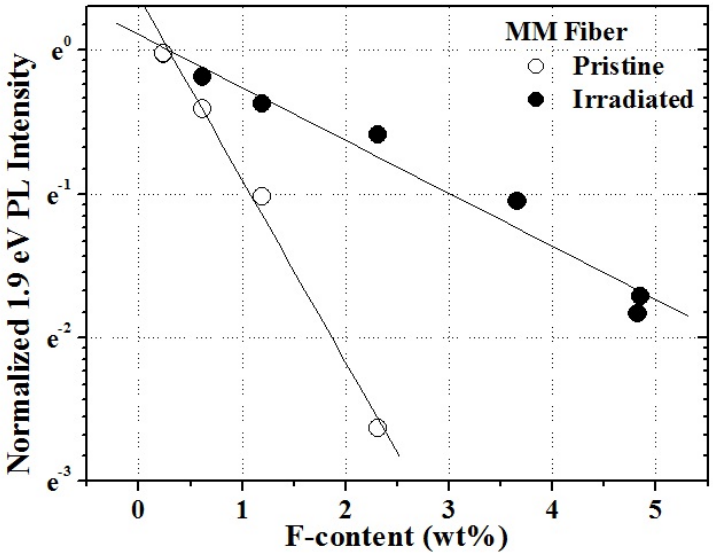

Figure 6.11: Normalized 1.9 eV PL intensity a function of the F content in the pristine and irradiated MM fiber, in semi-logarithmic scale. Solid lines represent the best fitting curves with Eq. 6.2.

6.1.4 Radiation and annealing effects on the Raman spectra

To investigate more the radiation and annealing effects on the samples, Raman spectra were recorded by using the Confocal Microscopy Raman setup. In this case, the results are shown for the fiber F-MMF2, because of the higher signal-to-noise ratio of these spectra.

The fluorine is incorporated into the silica matrix by forming mainly Si-F bonds, indeed the presence of free fluorine atoms was predicted by simulations only in high temperature quenched glasses [161]. Generally, the fluorine tends to depolymerize the silica network, by breaking Si-O-Si linkages, preferentially the strained ones, replacing a bridging oxygen atom and, consequently, resulting in SiO_3F tetrahedra, where the Si-F distance is about 1.7 Å [161]. However, in an experimental and simulation work [161] Youngman et al. observed that a small fraction of fluorine can bond to Si atoms without any rupture of the Si-O network, resulting in fivefold coordinated silicons of the type of SiO_4F, where the Si-F distance is longer, around 1.9-2 Å. Finally, on the basis of bond valence calculations, the fluorine atom can exist in a bridging configuration, as Si-F-Si linkages, but there is still no experimental evidence.

The presence of the fluorine gives rise to two new bands in the Raman spectra: they are peaked around 480 and 945 cm^{-1} and ascribed to the Si-F bending and stretching

vibrational mode of a SiO_3F tetrahedron, respectively [162, 163].

To understand the Raman spectra of the silica glass, reported in the following, table 6.2 reports the assignement of all the most common Raman bands.

Position (cm^{-1})	Assignment
445 (main band)	symmetric stretching of bridging oxygens in n-membered rings, with n higher than 5
495 (D1)	breathing motion of bridging oxygens in 4-membered rings
606 (D2)	breathing motion of bridging oxygens in 3-membered rings
800	bending of the Si-O-Si bridge
1060	TO (transversal optical mode) asymmetric stretching of bridging oxygens
1200	LO (longitudinal optical mode) asymmetric stretching of bridging oxygens

Table 6.2: Raman band assignment for silica glass [10].

Fig. 6.12(a) shows the Raman spectra recorded in different zones of the F-doped multi-mode fiber; in particular, going outwards from the center, the F content increases, causing:

1. an increase in the intensity of the two Raman bands associated with the Si-F bonds, as observed by Shimodaira et al. [163]: the increasing of the 480 cm^{-1} band makes impossible to determine the D1 band presence and the main band position, that seems to shift towards higher wavenumbers;

2. a clear decrease in the intensity of the D2 band, as observed by Mulder et al. [164]; in our case, an increase of the F concentration from 0.2 to 5 wt% leads to a reduction of the D2 band area by ∼10%;

3. the loss of the components at lower wavenumbers of the 1060 cm^{-1} band, causing a shift of its peak, while the other component at 1200 cm^{-1} does not show any change.

It was observed that the γ-radiation up to a 10 MGy dose does not change the silica structure (curves not shown here), whereas the thermal treatment does. Fig. 6.12(b) reports the Raman spectra recorded in different zones of the F-doped multi-mode fiber after an annealing at 750°C and it highlights that the annealing affects more the structure of the zones with higher F content, by inducing bigger changes in the Raman bands, as:

1. the reduction of the D2 area which ranges from 10%, in the core center with only 0.2 wt% F content, to 80%, in the zone with 5 wt% F content;

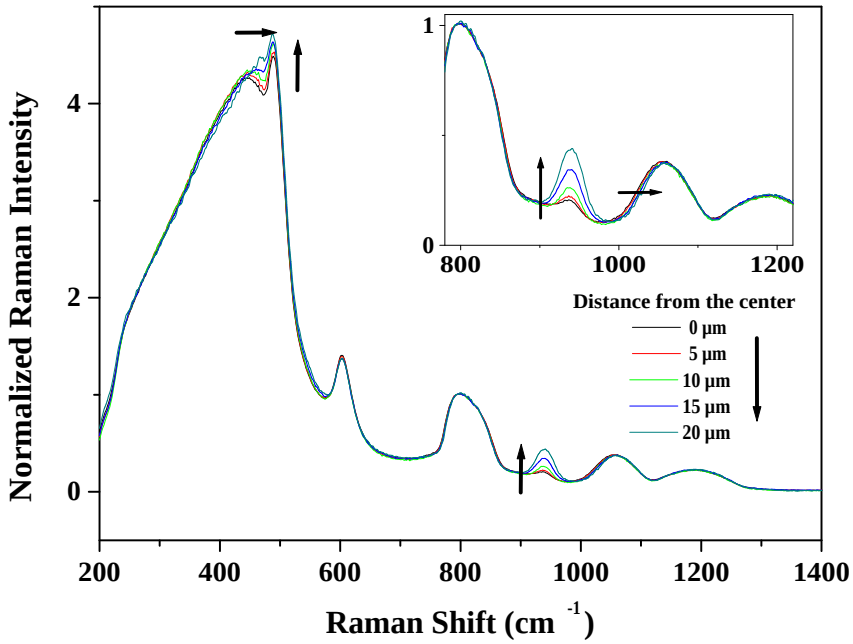

(a) Pristine fiber

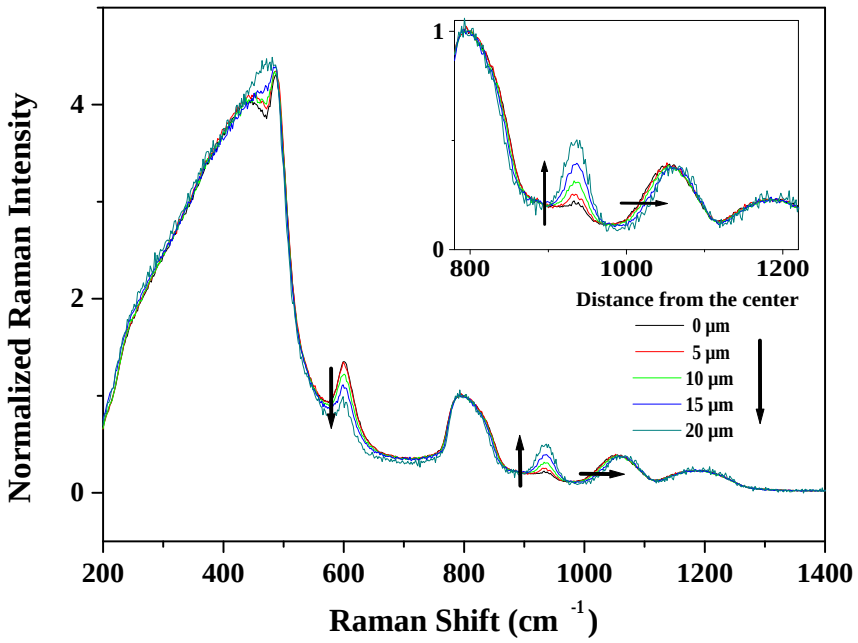

(b) Fiber annealed at 750°C

Figure 6.12: Raman spectra detected at different distances from the center in the pristine F-doped multi-mode fiber, (a) before and (b) after a thermal treatment at 750°C. All the spectra were measured under excitation at 3.82 eV, with a spatial resolution of ∼5 μm (due to the 40× objective and the diaphragm diameter of 75 μm), and normalized to the intensity of the peak around 800 cm^{-1}. The arrows show the trend of Raman bands on increasing the distance.

2. a shift of the 1060 cm^{-1} band peak towards higher wavenumbers.

No observation can be made for the D1 band, because of its overlapping with other bands. In conclusion, it seems that the thermal treatment facilitates the fluorine in fulfilling its task.

To better understand the annealing effects on fluorine, fig. 6.13 displays the area of the 945 cm^{-1} and D2 bands as a function of the distance from the center for the F-doped multi-mode fiber after three thermal treatments. The profile of the Si-F stretching peak coincides with that of the F concentration and does not change with increasing treatment temperature, indeed, as already said, all the F atoms realize Si-F bonds in the silica matrix, independently of the treatment. In contrast, the profile of the D2 band is anticorrelated with the F content and by increasing the annealing temperature its area decreases with a bigger reduction in the zone with a higher F concentration. This seems to point out that, because of a treatment at temperature higher than 300°C, the Si-F bond is broken and the F links to the Si atom of another small membered ring.

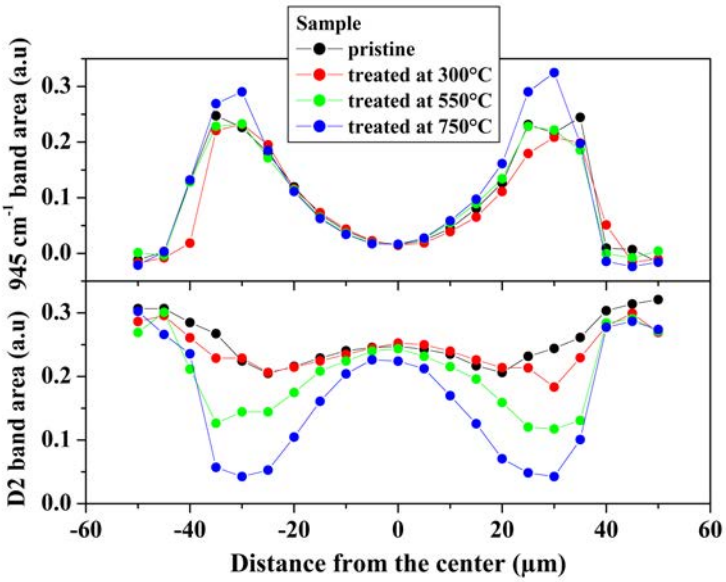

Figure 6.13: Area of (a) the 945 cm^{-1} band due to the Si-F stretching mode and (b) the D2 band ascribed to the breathing mode of the 3-membered rings, as a function of the distance from the fiber center, in thermally treated F-doped multi-mode fibers. The black points are associated with the fiber before any treatment, the others are referred to fibers annealed at different temperatures: red–300°C, green–550°C, blue–750°C.

To corroborate that the D2 band behavior depends on the F content and not on the internal stress inside the fiber core, the D2 area profile was analyzed also in a pure-silica core multi-mode fiber before and after the annealing at 750°C: the D2 area does not de-

pend on the radial position, within an error of 10%, nor before neither after the treatment, which causes only a global reduction of 15%.

A very important parameter which controls the degree of the structural disorder in silica glass is the fictive temperature, defined as the temperature at which the liquid structure is frozen when cooling down through the glass transition [165], and often coinciding with the long-lasting thermal treatment temperature. Shimodaira et al. [166] demonstrated that, in silica bulk, the D1 and D2 bands intensities increase, independently of the F concentration, with the increasing fictive temperature. Because of the 480 cm^{-1} band, which influences the main band around 400 cm^{-1}, it is not possible to determine the fictive temperature from its position in our F-doped samples. However, Martinet et al. [167] studied the changes in the Raman distribution of the fictive temperature in a pure silica cladding single-mode optical fiber and showed that in a pristine fiber the fictive temperature, calculated from the main band position, increases going outwards (from ∼1400°C, near the core, to ∼1700°C) and the D2 area increases with increasing fictive temperature; moreover, a 66 h-long thermal treatment at 1100°C decreases the fictive temperature of all the cladding and also the D2 band area without no difference along the fiber diameter. This lets us conclude that in absence of the fluorine the D2 band area should increase with increasing distance from the center or it should be independent of the distance. In our case the D2 band area decreases going outwards corroborating that this effect is only due to the F content and not on the different stress along the fiber diameter.

Comparison between F, D2 band and contents

It was shown that both D2 band area and NBOHC concentration are anticorrelated with F content: the lower the F content, the higher is the D2 amplitude and the larger is the radiation or drawing induced defect concentration. Since the OH content present in the samples is low (∼0.2 ppm), the main NBOHC generation process is not the radiolysis of ≡Si-OH bonds but rather the cleavage of strained ≡Si-O-Si≡ bonds, which are related to small membered rings. However, it can be deduced that these defects are not generated by a one-to-one conversion of strained bonds [160]. Firstly, inside the fiber core, the D2 band area varies by only 15%, while the NBOHC concentration decreases from the maximum obtained in the fiber center by 80% in the irradiated sample and down to zero (100%) in the pristine one. Secondly, if the NBOHC precursors were the strained bonds of the 3-membered rings, both the concentration and the distribution of the radiation-induced NBOHCs should change because of a pre-treatment at 750°C. Fig. 6.14 displays

a reduction of the 1.9 eV PL intensity in the fiber core only by 20% thanks to the thermal treatment performed before a X-ray irradiation up to 3 MGy dose, whereas the profile of this band does not change with the exception of the pure-silica cladding, whose NBOHC concentration increases because of the thermal treatment.

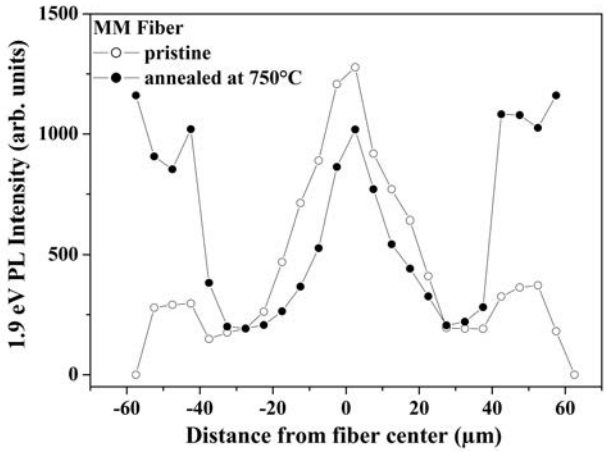

Figure 6.14: Profile of the 1.9 eV PL intensity emitted from the radiation induced NBOHCs, after X-ray irradiation up to 3 MGy dose at RT, in two F-doped MM fibers: one pristine and the other pre-annealed at 750°C, before irradiation. The PL spectra were performed on F-MMF2 with the CML setup, under excitation at 3.82 eV, using a 40× objective and a diaphragm diameter of 75 μm, for a spatial resolution of $\sim$5 μm.

6.1.5 Paramagnetic defects

Because of the limited UV range of the detector used to acquire the attenuation spectra, these measurements allow us to determine the concentration of defects absorbing only in the visible range, that are the NBOHCs. Another important technique that can be used to obtain more information about the defects concentration is the electron paramagnetic resonance that allows us to identify, nonetheless, only the paramagnetic centers.

One of the most common paramagnetic intrinsic defects is the E′: its typical first harmonic EPR spectrum, characterized by axial symmetry, is recorded at RT using the optimal parameters $P_{in} = 8 \cdot 10^{-4}$ mW and $H_m = 0.1$ G and it is shown in fig. 6.15(b). Also a variant of the E′ center can be observed in EPR spectra but using other parameters, $P_{in} = 0.2$ mW and $H_m = 1$ G (or 4 G in case of low defect concentration): it is the H(I) defect, consisting of a dangling Si bond with one neighboring O substituted by a H atom. The hyperfine interaction between the unpaired electron and the H nucleus, with

spin of 1/2, originates the doublet of 74 G, shown in fig. 6.15(a). In contrast to these centers, the oxygen-related defect signals are very large and they overlap, so they can not be distinguished at RT: measurements at low temperature, 77 K (liquid nitrogen), are needed to separate the two contributions. Fig. 6.16 displays an EPR spectrum recorded at 77 K with P_{in} = 1 mW and H_m = 0.6 G and the reference signals of the NBOHC and POR reported in literature [168] and which are used for the deconvolution. The spectrum of fig. 6.16 shows also the E′ signal distorted because of the high used values of P_{in} and H_m.

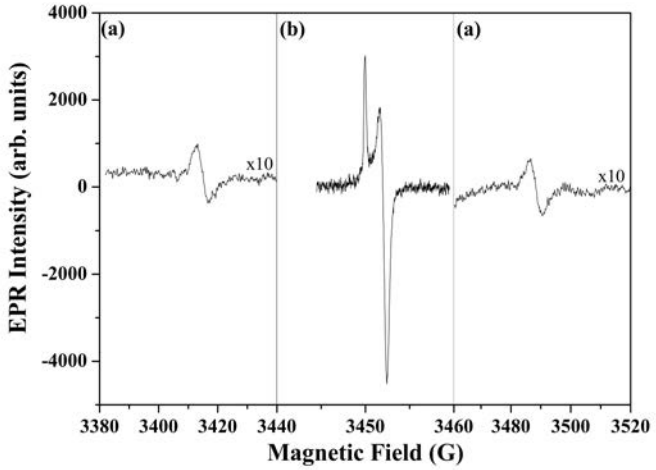

Figure 6.15: EPR first harmonic spectra in the F-doped multi-mode fiber γ-irradiated at 10 MGy. The part (a) was recorded with P_{in} = 0.2 mW (attenuation of 30 dB) and H_m = 1 G and shows the doublet of the H(I) center, whereas the part (b) was recorded with P_{in} = $8 \cdot 10^{-4}$ mW (attenuation of 54 dB) and H_m = 0.1 G and shows the signal of the E′ center.

Before irradiation, the EPR spectra show only a very low signal associated with the E′ center, as a consequence, the pristine samples are characterized by an E′ concentration of about $10^{14}\,\mathrm{cm}^{-3}$ whereas all the other defects, if present, have a concentration under the detection limit.

Figures 6.17 and 6.18 report the calculated concentration values for the different paramagnetic defects and they show that for all the defects:

- the concentration grows with both γ-dose and neutron fluence,
- more defects are created in the multi-mode fiber than in the single-mode one, under the same conditions.

For the E′ center, the concentration reached at 10 MGy dose is about $10^{17}\,\mathrm{cm}^{-3}$, three order of magnitude higher than in the pristine samples.

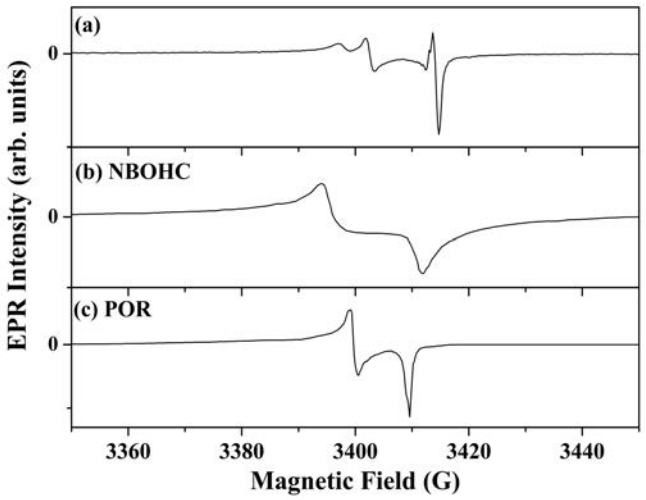

Figure 6.16: (a) EPR first harmonic spectra in the F-doped multi-mode fiber γ-irradiated at 10 MGy, recorded at 77 K with P_{in} = 1 mW (attenuation of 23 dB) and H_m = 0.6 G. (b)-(c) EPR spectrum associated with the NBOHC and the POR [168].

In fig. 6.19, we plot the concentration of the E′ defects as generated through primary (γ-rays associated with the neutron tests) or secondary (indirect effect: 1 Gy for $3 \cdot 10^{13}$ n/cm^2) ionization processes by considering the total ionizing dose as sole generation mechanism. In case displacement damages play mayor role in the defect generation, the concentration for γ-rays and neutron irradiations should present very different total ionizing dose dependence. This is clearly not the case, as only small differences in the dose dependance can be observed, at the highest neutron fluence, maybe due to displacement damages or to the different conditions between the two facilities used for the tests.

Once the concentration of defects, such as NBOHC and E′, is known, the Smakula's equation (Eq. 4.6) can be used to calculate their absorption bands, whose positions and width are reported in literature [169]. Fig. 6.20 compares the RIA curves of the F-doped multi-mode fiber irradiated at 10 MGy: the measured spectrum with that obtained as a sum of the bands associated with NBOHC and E′ defects.
This graph highlights that these centers cause an attenuation of about $5 \cdot 10^3$ dB/m at 5.8 eV (∼210 nm) and they can not be the origin of the UV tail observed in the measured spectrum: this is likely caused by Cl-related centers, since two absorption bands at 3.8 eV (FWHM of 0.67 eV) and at 3.05 eV (weaker than the first one) are associated with the Cl_2 molecules [137], a band at 2.98 eV is attributed to Cl_2^- ions and another at 3.95 eV to Cl atoms [170].

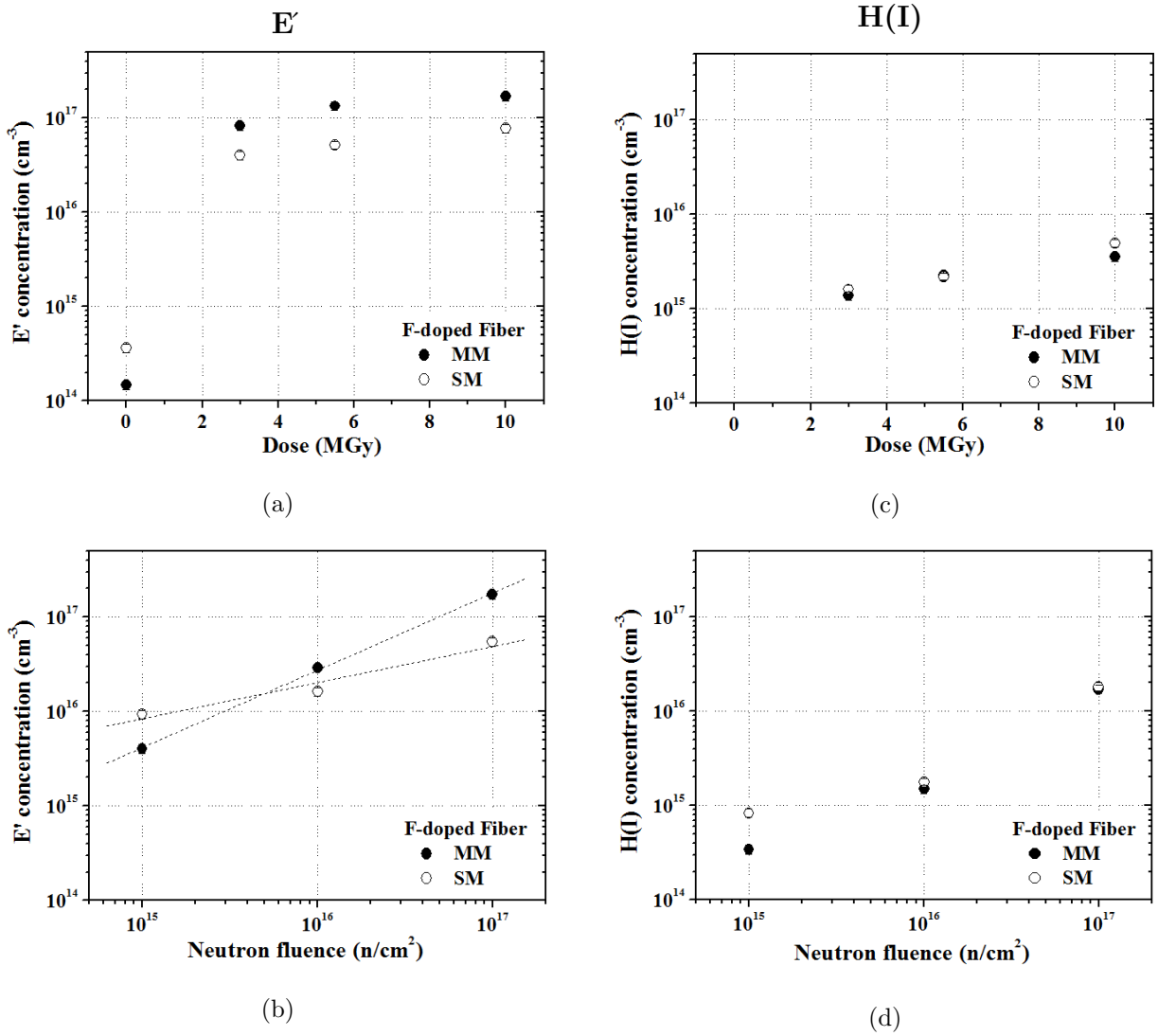

Figure 6.17: E´ and H(I) concentration as a function of (a,c) the γ-radiation dose and (b,d) the neutron fluence, in the F-doped multi- (full circles) and single-mode (empty circles) fibers. In the pristine fibers the H(I) doublet was not observed.

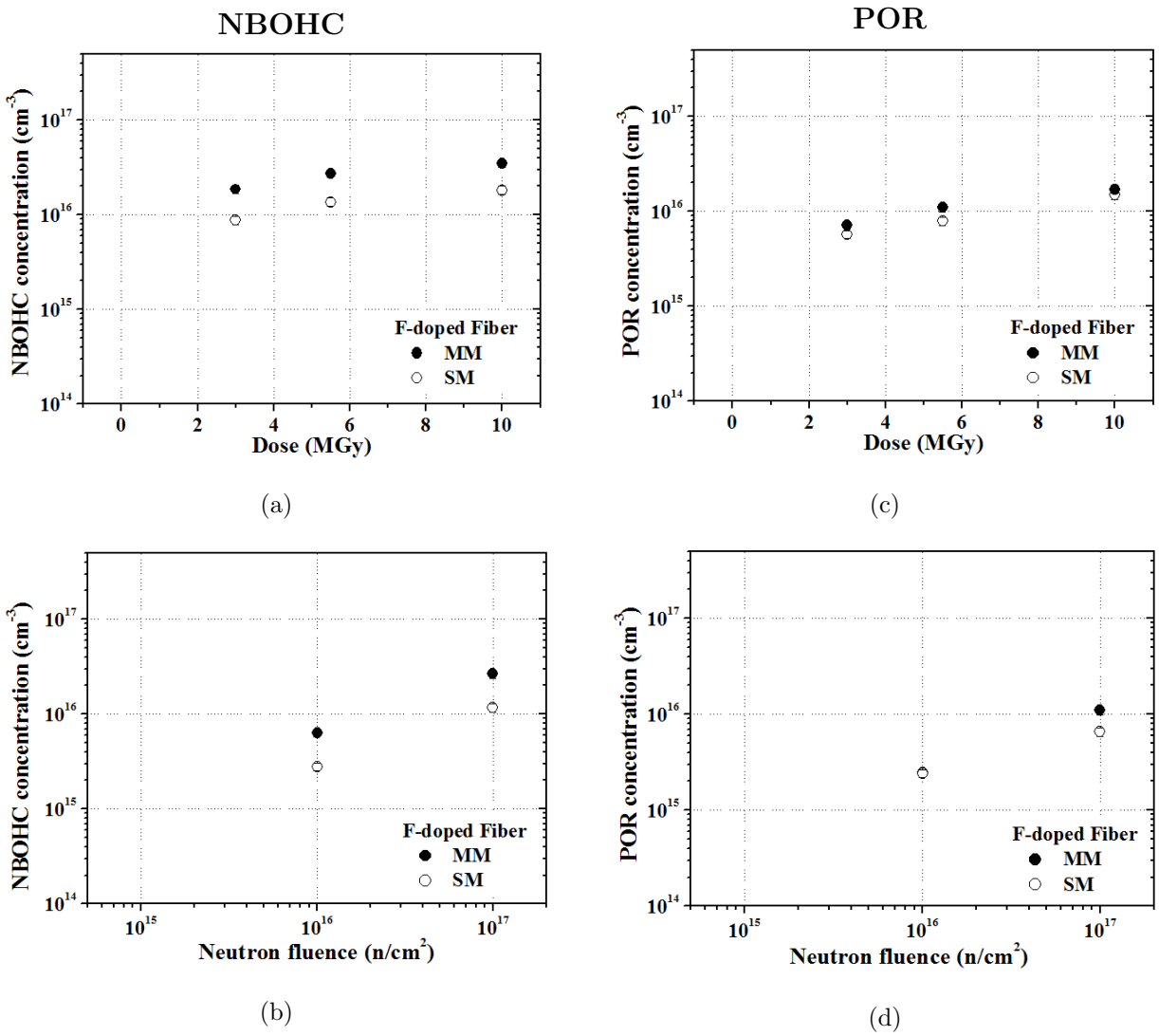

Figure 6.18: NBOHC and POR concentration as a function of (a,c) the γ-radiation dose and (b,d) the neutron fluence, in the F-doped multi- (full circles) and single-mode (empty circles) fibers. With the neutron fluence of 10^{15} n/cm^2, the oxygen-related defect concentrations are under the detection limit, lower than 10^{15} cm^{-3}.

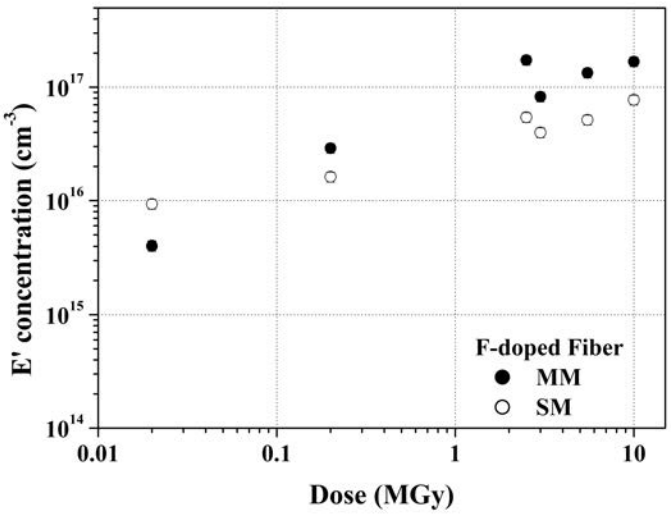

Figure 6.19: E′ concentration generated by γ-rays and neutrons only through ionization.

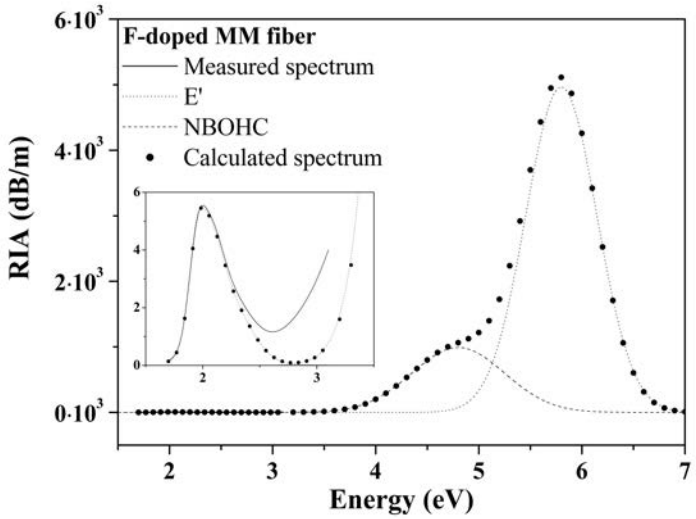

Figure 6.20: RIA spectrum of the F-doped multi-mode fiber irradiated at 10 MGy: measured (continuous line) and calculated (dots) spectra. In the inset a zoom of the curves in the visible region.

6.1.6 Conclusions

Before irradiation, the defect concentration is about $10^{14}\,\mathrm{cm}^{-3}$ for the E′ centers and even lower for the other defects, indeed it can not be determined because under detection limit. Both irradiations, γ-rays and neutrons, produce in the fibers intrinsic defects, as E′, NBOHCs and PORs, whose concentration grows without saturating at the maximum

reached doses, γ-ray dose of 10 MGy or neutron fluence of 10^{17} n/cm^2.

It can be observed that in silica bulk, reported in literature, the concentration of the E′ centers induced by γ-radiation is much higher than that of the oxygen related defects, because the main precursors are the impurities [171], whereas for the fibers the concentrations of the E′, NBOHC and POR defects are of the same order of magnitude.

Generally, it was observed that more defects are created in the multi-mode fibers than in the single-mode one, under the same conditions. Only for the H(I) defect, its concentration does not depend on the fiber type. The presence of this center could seem singular, as the samples are not hydrogenated and the concentration of hydrogen inside the fiber is low (for example, the initial OH concentration is about $4 \cdot 10^{15}$ cm^{-3}). It can be generated from ≡Si-H bonds (whose presence can not be verified) or from the reaction of an H atom with a two-fold-coordinated silicon center [169]:

$$= \mathrm{Si}^{\bullet\bullet} + H \rightarrow = \mathrm{Si}^{\bullet} - \mathrm{H} \tag{6.4}$$

The H atoms can come from the breakage of an O-H bond or from the acrylate coating, in the case of the neutron irradiated samples [21, 172]: hydrogen atoms are released from the coating and diffuse in the fiber glass.

NBOHC and Fluorine

Several results, as the unchanging shape of the 2 eV absorption band with the radiation dose or its correlation with the 1.9 eV photoluminescent band, point out that the NBOHC is the only defect originating the asymmetric absorption around 2 eV. Moreover, their PL band at 1.9 eV was studied in detail in fibers and the obtained results are reported in the following.

- This PL red-shifts and broadens because of the radiation, whereas the thermal treatment causes the opposite effects. The shift of the PL peak may reflect a change in the defect environment induced by the radiation, whereas high temperatures recover the pre-irradiation glass structure, as already explained for other defects, like E′, that presents the same behavior under radiation and annealing [173–175]. The band broadening with irradiation can be explained by an increasing disorder in the surroundings of the NBOHCs [158].

- The decay of this PL can be described by a stretched exponential, $\exp(-(t/\tau)^{\beta})$, with $\tau = (11 \pm 1)$ μs and $\beta = 0.81 \pm 0.07$. The decay features remain unchanged regardless the excitation energy, the irradiation or the thermal treatments; consequently, the interaction between the defect and the environment does not affect the lifetime.

- This PL can be excited in the visible through an asymmetric band peaked at (1.95 ± 0.02) eV with FWHM of (0.16 ± 0.02) eV, that does not change with radiation.
- The PL and PLE band shapes can be described by a Pekarian curve with similar parameters; however, the OA band is wider than the PLE one, resulting in a quantum yield dependent on the photon energy and suggesting that there are absorbing NBOHCs with non-radiative emission.

The NBOHCs can be created by [7]:

- the radiolysis of ≡Si-OH bonds:

$$\equiv \text{Si-O-H} \rightarrow \equiv \text{Si-O}^{\bullet} + \text{H}^{\bullet} \tag{6.5}$$

- the cleavage of strained ≡Si-O-Si≡ bonds:

$$\equiv \text{Si-O-Si} \equiv \rightarrow \equiv \text{Si-O}^{\bullet} +^{\bullet} \text{Si} \equiv \tag{6.6}$$

Since the OH content is low in our fibers, the most likely precursors of NBOHCs are the strained bonds of small membered rings but the conversion process is not linear. Moreover, the fluorine hinders the generation of NBOHCs: the higher the F content, the lower the radiation or drawing induced NBOHC concentration; indeed, the increment of F reduces the effective volume where NBOHCs are formed.

Finally, an annealing at temperature higher than 300°C facilitates the fluorine to modify the silica structure, for example by destroying strained bonds, but it does not improve the fiber radiation-resistance.

6.2 Germanium doped fibers

This section deals with the γ-radiation effects on the Ge-doped fibers: the results here reported were obtained on Ge-MMF and Ge-SMF, fibers doped with germanium and fluorine.

6.2.1 RIA and its origin

Fig. 6.21 shows the RIA spectra of the multi- and single-mode Ge-doped fibers, after a γ-radiation dose of 10 MGy: the curves, that coincide except for the UV region, show the same trend of the F-doped fibers. However, the attenuation values are one order of magnitude higher and the RIA curve minimum is at longer wavelength, around 1200 nm, as observed by Regnier et al. in similar samples [151].

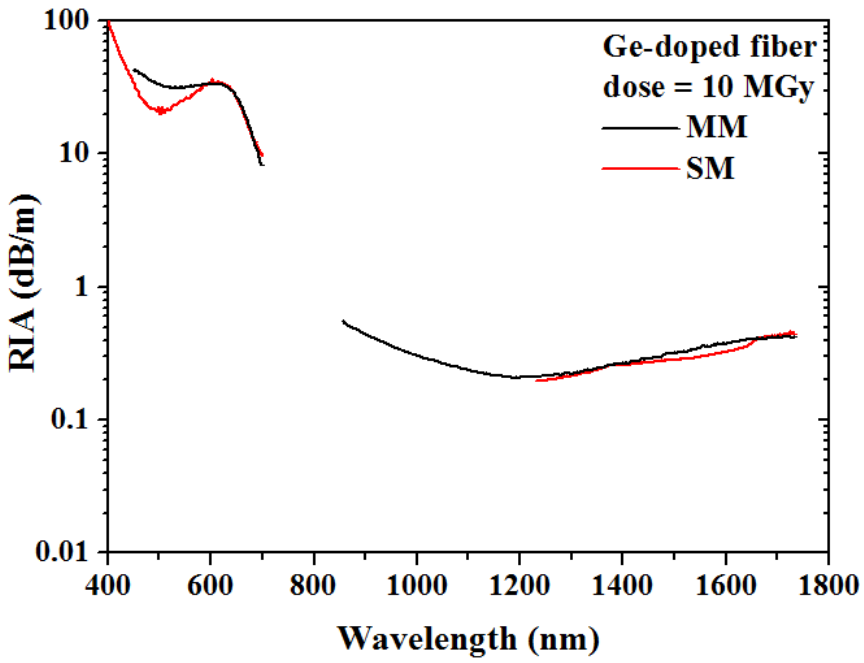

Figure 6.21: RIA spectra of the γ-irradiated Ge-doped multi- (black curve) and single-mode (red curve) fibers at 10 MGy.

As for the F-doped fibers, the RIA increases with increasing irradiation dose, with the exception of the UV component of the SM fiber that clearly decreases in fig. 6.22, whereas it decreases with post-irradiation thermal treatments.

In the UV-visible range (fig. 6.23(a)), the absorption band around 620 nm is not completely bleached because of the thermal treatment at 550°C, after which a residual attenuation of about 2 dB/m is still present at the wavelength of 620 nm. The UV tail

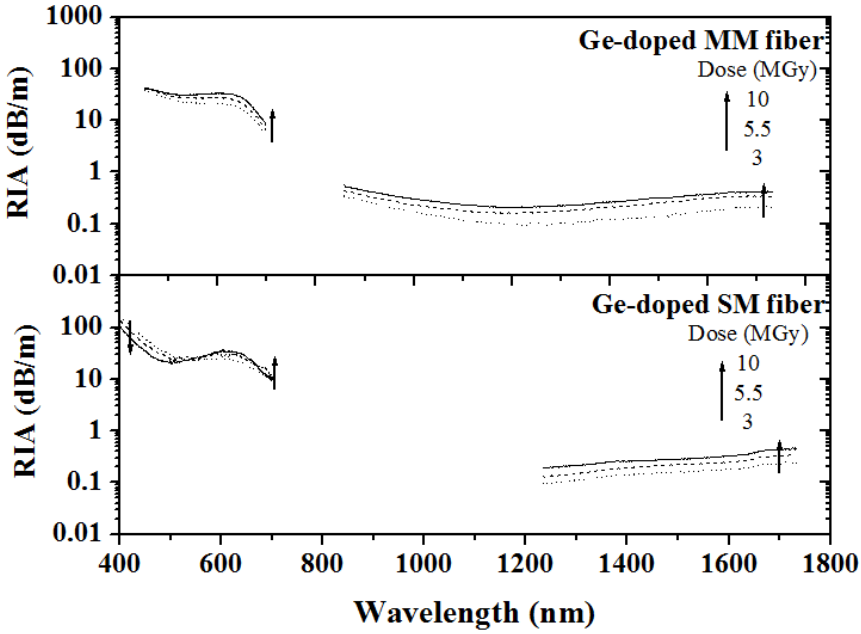

Figure 6.22: RIA spectra of the γ-irradiated Ge-doped (a) multi- and (b) single-mode fibers at different doses.

residual value is higher, around 5 dB/m at the wavelength of 400 nm, but a further treatment at 750°C (curves not shown) does not improve the transmission. In the IR range (fig. 6.23(b)), it is the annealing at 300°C that causes the main change but only after the treatment at 550°C the RIA is reduced at 0 dB/m, within the error of the measurement.

The origin of the IR-band is still unknown: as for F-doped fibers, in literature it is tentatively associated with STHs [151].

For the UV-Visible part of the RIA spectrum, a decomposition as a sum of Gaussians has been realized. Starting from the three Gaussian bands used by Griscom for the decomposition of the RIA curves of γ-irradiated Ge-doped silica fiber image guides and associated with Ge(1), GeX and Ge-NBOHC defects [16], three Gaussian bands were initially used to decompose the RIA spectra. However, the thermal treatment results obliged us to add another band to obtain good fit. Fig. 6.24 shows the decomposition of the RIA spectrum of the 10 MGy irradiated MM fiber; the spectral parameters obtained from the fits are listed in table 6.3[1]. In literature, the absorption band of the Ge-NBOHC defects is simulated by a Gaussian band peaked at 1.97 eV (FWHM of ∼0.3 eV)

[1]The parameters of the Ge(1) band do not have an associated error, indeed they were fixed during the fitting procedure, because only a tail of this band is shown in the RIA spectra and it is not possible to determine its real peak position.

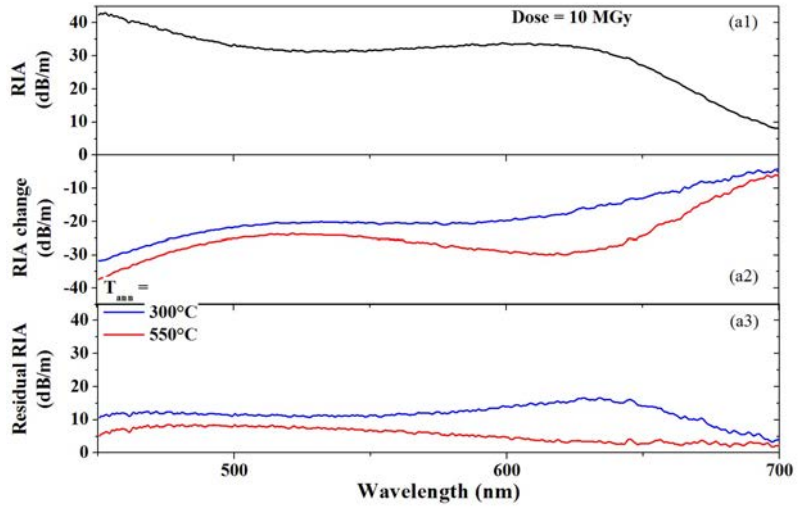

(a) Visible range

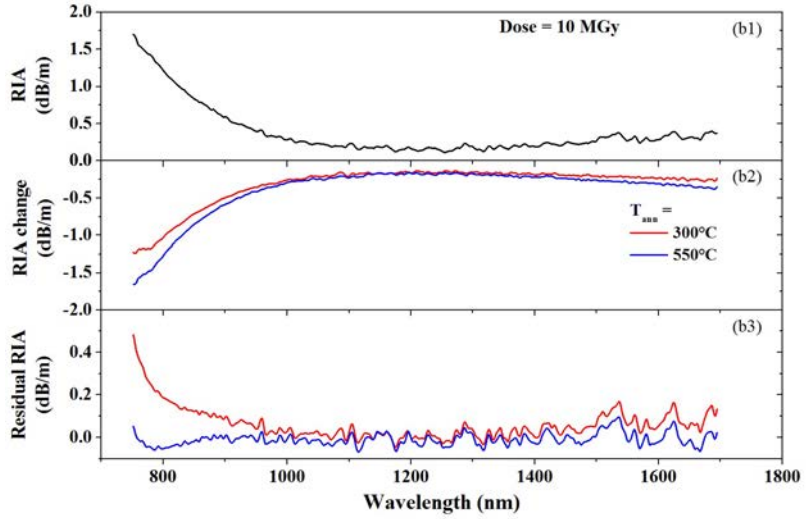

(b) IR range

Figure 6.23: All the spectra are referred to the 10 MGy irradiated Ge-doped multi-mode fiber: (a1-b1) RIA spectrum obtained with the cut-back technique, (a2-b2) RIA changes induced by the thermal treatments at 300°C (red line) and 550°C (blue line), (a3-b3) Residual RIA after the thermal treatments, obtained as the sum of the curve reported in (a1-b1) and those in (a2-b2). The effects of the thermal treatment at 750°C are not shown, because it causes no further change.

[15,16,176], however, with a view to the possibility to associate an asymmetric absorption band with the NBOHCs in F-doped fibers (as demonstrated in section 6.1.1), the 2.11 eV component, not present in literature, could be conceived as another contribution to the absorption due to the Ge-NBOHCs or to both Si- and Ge-NBOHCs.

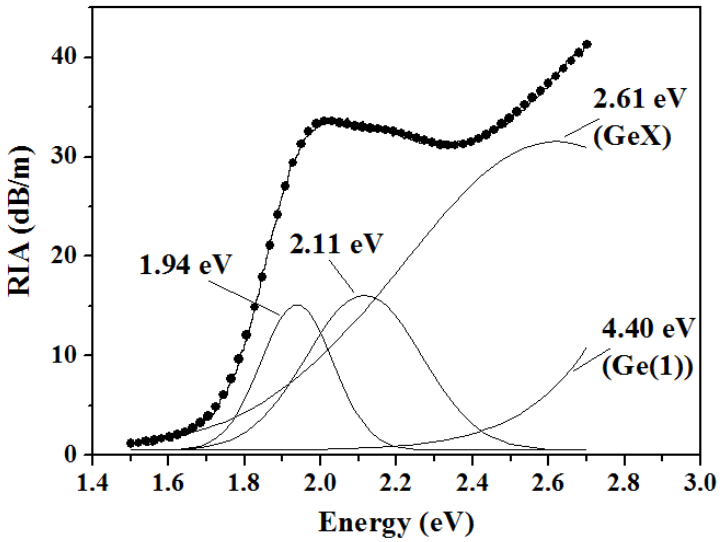

Figure 6.24: Decomposition into Gaussian bands of the RIA spectrum for the 10 MGy irradiated Ge-doped fiber: measured spectrum (dots) and fitted curves (lines).

Band	Assignment	Position (eV)	FWHM (eV)
1	Ge(1)	4.40	1.30
2	GeX	2.61 ± 0.08	0.96 ± 0.08
3	NBOHC	2.11 ± 0.10	0.36 ± 0.07
4		1.94 ± 0.05	0.23 ± 0.08

Table 6.3: Spectral parameters of the bands used for the decomposition of all the OA spectra recorded in Ge-doped irradiated fibers. The error accounts for half of the maximum deviation.

6.2.2 Spectroscopic characteristics of NBOHCs present in Ge-doped fibers

The PL at 1.9 eV due to the Si-NBOHCs was widely studied in pristine and γ-irradiated F-doped fibers (see section 6.1.2). In literature, a PL band having similar characteristics to the Si-NBOHC, with peak position at 1.86 eV, FWHM of 0.16 eV and decay constant of $\sim 5\mu$s, was observed by Skuja et al. in γ-irradiated GeO_2 samples and associated with the Ge-NBOHCs [177]. As a consequence, in Ge-doped silica fibers it

is expected that both types of NBOHCs are induced by the fabrication process and the radiation and contribute to the PL at ∼1.9 eV: the time-resolved PL is a very useful technique to separate the two contributions.

Fig. 6.25 shows the *decay kinetics* of the PL intensity monitored at 1.9 eV and excited at three different energies: 2.07 eV and 4.77 eV, that are the maxima of the visible and UV excitation bands of the Si-NBOHC [154], and 3.44 eV, to make a comparison with the results reported on the GeO_2 bulk by Skuja et al. [177].

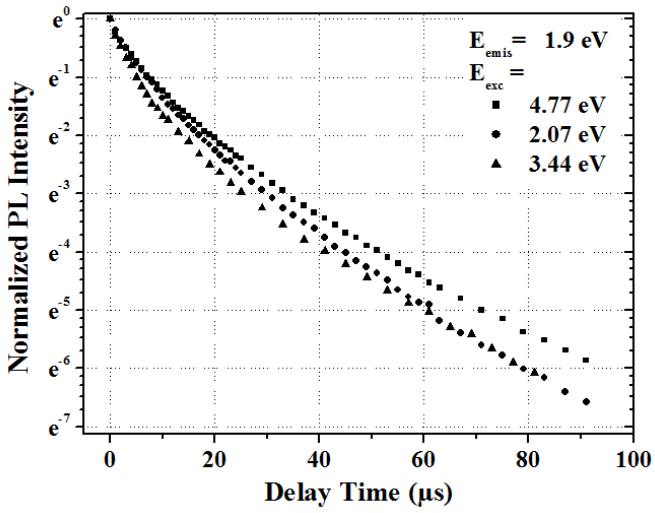

Figure 6.25: Semilog plot of the PL decay measured at 1.9 eV in the 10 MGy irradiated Ge-doped multi-mode fiber, under three different excitations: squares–4.77 eV, circles–2.07 eV, triangles–3.44 eV.

The decay is faster than in the F-doped fibers and the curves are best fitted by the sum of two stretched exponentials, one to attribute to the Si-NBOHC and the other likely to the Ge-NBOHC:

$$I_{PL}\,(t, E_{exc}) = I_{Si}\,(E_{exc}) \cdot \exp(-(t/\tau_{Si})^{\beta_{Si}}) + I_{Ge}\,(E_{exc}) \cdot \exp(-(t/\tau_{Ge})^{\beta_{Ge}}) \qquad (6.7)$$

where I_{Si} and I_{Ge} are coefficients proportional to the number of centers emitting a photon under excitation E_{exc}. In order to reduce the number of free parameters, τ_{Si} and β_{Si} were fixed to the values obtained for the Si-NBOHCs in the previous study on the F-doped fibers, 11 μs and 0.81, respectively. Table 6.4 reports the parameters values obtained by the fitting procedure: they do not change with the irradiation but show a dependence on the excitation energy.

An increase of the parameter I_{Ge} implies an increase of the emitting centers number; consequently, whereas the Si-NBOHCs are only weakly excited at 3.44 eV compared with 4.77 eV [178], the Ge-NBOHCs should be characterized by an excitation spectrum in the

Excitation (eV)	τ_{Ge} (μs)	β_{Ge}	$I_{Si} : I_{Ge}$
4.77	4.7 ± 0.2	0.78 ± 0.01	50:50
3.44	3.5 ± 0.1	0.86 ± 0.02	35:65
2.07	4.94 ± 0.04	0.84 ± 0.03	45:55

Table 6.4: Values of the parameters characterizing the Ge-NBOHCs present in the 10 MGy irradiated multi-mode fiber and obtained by fitting the curves of fig. 6.25 with the function of Eq. 6.7.

UV range with a component at low energies higher than that of the Si-NBOHC. Indeed, the PL spectrum emitted from the Ge-doped fiber under excitation at 3.44 eV is peaked at lower energy than under excitation at 4.77 eV, as reported in fig. 6.26(a) and in table 6.5: this red-shift is due to the bigger contribution of the Ge-NBOHC component at ∼1.86 eV with respect to that of the Si-NBOHC at ∼1.90 eV. By comparing the PL band shape emitted from the Ge-doped fiber and from the F-doped one under excitation at 2.07 eV, as shown in fig. 6.26(b), a very small red-shift, lower than 0.01 eV, can be also observed.

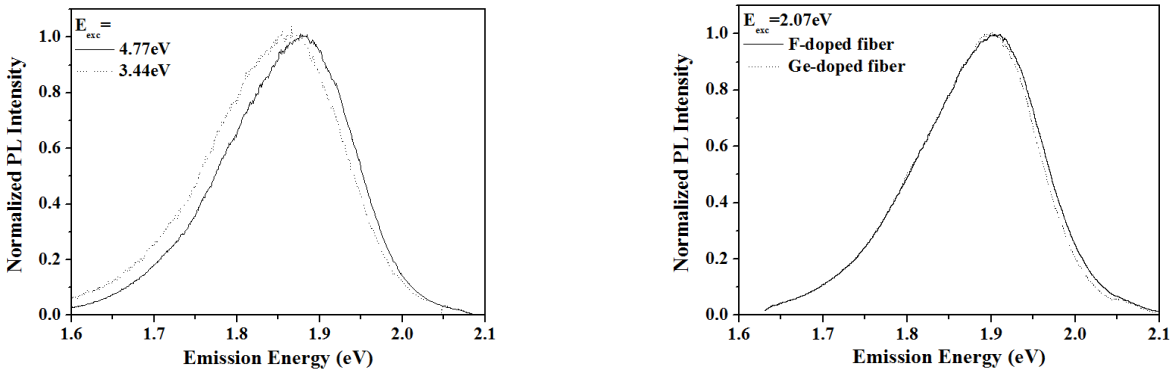

(a) (b)

Figure 6.26: (a) PL spectra recorded on the 10 MGy irradiated Ge-doped MM fiber, under different excitation: dotted line–3.44 eV, continuous line–4.77 eV. The temporal parameters were fixed: T_D = 1 μs and Δt = 5 μs, that is a lifetime of the Ge-NBOHCs. (b) PL specrta recorded under excitation at 2.07 eV on samples γ-irradiated at 10 MGy: dotted line–Ge-doped fiber, continuous line–F-doped fiber. The temporal parameters were fixed: T_D = 1 μs and Δt = 10 μs, that is a lifetime of the Si-NBOHCs.

Finally, the *excitation spectrum* of the PL due to the Ge-NBOHCs was tentatively calculated in the 10 MGy irradiated multi-mode fiber. The excitation photon energy was varied from 1.7 to 2.3 eV and for each of these values two PL spectra were recorded in two different time windows: a fast one having T_D = 1 μs and Δt = 5 μs and a slow one with T_D = 10 μs and Δt = 10 μs. Fig. 6.27(a) reports the PL peak intensity as a function

Excitation (eV)	peak (eV)	FWHM (eV)
4.77	1.88	0.180
3.44	1.86	0.187

Table 6.5: Peak position and FWHM of the PL bands reported in fig. 6.26(a), emitted from the 10 MGy irradiated multi-mode fiber under excitation at 3.44 eV and 4.77 eV.

of the excitation energy for the two time windows: the fact that the two curves do not coincide, above all at low energies, highlights the presence of two emissions, indeed if only the Si-NBOHC was the origin of the 1.9 eV emission, the excitation profile should not change during the PL decay, as observed by Cannas et al. [179].

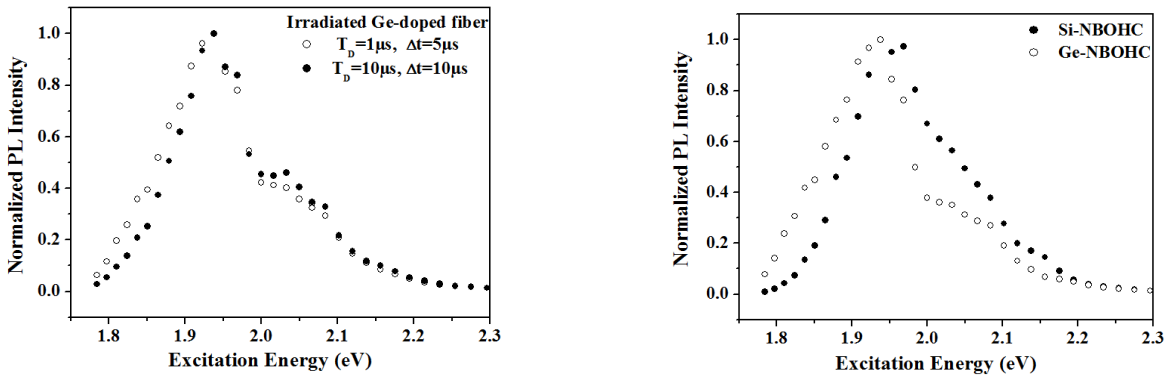

(a) (b)

Figure 6.27: (a) PL peak intensity as a function of the excitation energy measured in the Ge-doped fiber with: $T_D = 1\mu s$ and $\Delta t = 5\mu s$ (empty circles) or $T_D = 10\mu s$ and $\Delta t = 10\mu s$ (full circles). The curves are plotted normalized to their maximum amplitude. (b) Normalized visible excitation spectrum associated with the Si-NBOHC (full circles) and the Ge-NBOHC (empty circles).

As already said, the PL intensity depends on time according to the expression reported in Eq. 6.7, where $\tau_{Si} = 11\ \mu s$, $\beta_{Si} = 0.81$, $\tau_{Ge} = 4.94\ \mu s$ and $\beta_{Ge} = 0.84$, under the hypothesis that the decay features do not change within the visible excitation band. Moreover, the coefficients I_{Si} and I_{Ge} can be considered as the products of a term proportional to the defect concentration and another to the normalized PLE intensity, that means:

$$\begin{aligned} I_{Si}(E_{exc}) &= I^0_{Si} \cdot I^{PLE}_{Si}(E_{exc}) \\ I_{Ge}(E_{exc}) &= I^0_{Ge} \cdot I^{PLE}_{Ge}(E_{exc}) \end{aligned} \tag{6.8}$$

where $I^{PLE}_{Si}(E_{exc})$ is illustrated in fig. 6.8. By substituting the expression of I_{PL} in Eq. 4.12 for the two time windows:

$$\begin{cases} I(\mathrm{T}_D = 1\mu\mathrm{s}, \Delta\mathrm{t} = 5\mu\mathrm{s}, E_{exc}) = I^0_{Si} \cdot I^{PLE}_{Si}(E_{exc}) \cdot \left(\int_{1\mu\mathrm{S}}^{6\mu\mathrm{S}} \exp(-(t'/\tau_{Si})^{\beta_{Si}})\,\mathrm{d}t'\right) + \\ + I^0_{Ge} \cdot I^{PLE}_{Ge}(E_{exc}) \cdot \left(\int_{1\mu\mathrm{S}}^{6\mu\mathrm{S}} \exp(-(t/\tau_{Ge})^{\beta_{Ge}})\,\mathrm{d}t'\right) \\ \\ I(\mathrm{T}_D = 10\mu\mathrm{s}, \Delta\mathrm{t} = 10\mu\mathrm{s}, E_{exc}) = I^0_{Si} \cdot I^{PLE}_{Si}(E_{exc}) \cdot \left(\int_{10\mu\mathrm{S}}^{20\mu\mathrm{S}} \exp(-(t'/\tau_{Si})^{\beta_{Si}})\,\mathrm{d}t'\right) + \\ + I^0_{Ge} \cdot I^{PLE}_{Ge}(E_{exc}) \cdot \left(\int_{10\mu\mathrm{S}}^{20\mu\mathrm{S}} \exp(-(t/\tau_{Ge})^{\beta_{Ge}})\,\mathrm{d}t'\right) \end{cases} \tag{6.9}$$

and by resolving, for each E_{exc}, the system of two equations in the two variables I^0_{Si} and $I^0_{Ge} \cdot I^{PLE}_{Ge}(E_{exc})$, the excitation profile of the Ge-NBOHC can be obtained and the result is reported in fig. 6.27(b): it is constituted by a band peaked around 1.93 eV, with FWHM of ∼0.14 eV.

6.2.3 Spatial distribution of photoluminescent centers

The Confocal Microscopy Luminescence setup allows us to study the profile of the luminescent centers along the fiber diameter. The laser light at 3.82 eV, used to record the spectra, excites two centers: one of the two PL bands of the GLPC, the slow component ($\tau \sim 110$ μs) at 3.1 eV (∼400 nm), and the NBOHC, at 1.9 eV (∼650 nm), as shown in fig. 6.28. Fig. 6.29 displays the intensity profile of these PL bands: the NBOHC concentration increases because of the radiation, whereas the GLPC concentration decreases by 30% for the dose of 3 MGy and remains practically constant for higher doses.

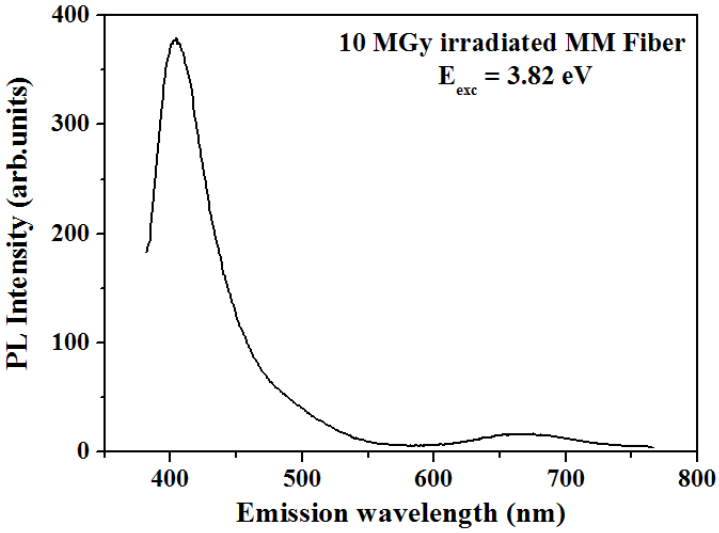

Figure 6.28: Typical PL spectrum recorded on the Ge-doped fiber with the CML setup under excitation at 3.82 eV: the 40× objective and a diaphragm diameter of 50 μm entail a spatial resolution of ∼3 μm. This PL is emitted by the core of the MM fiber irradiated at 10 MGy.

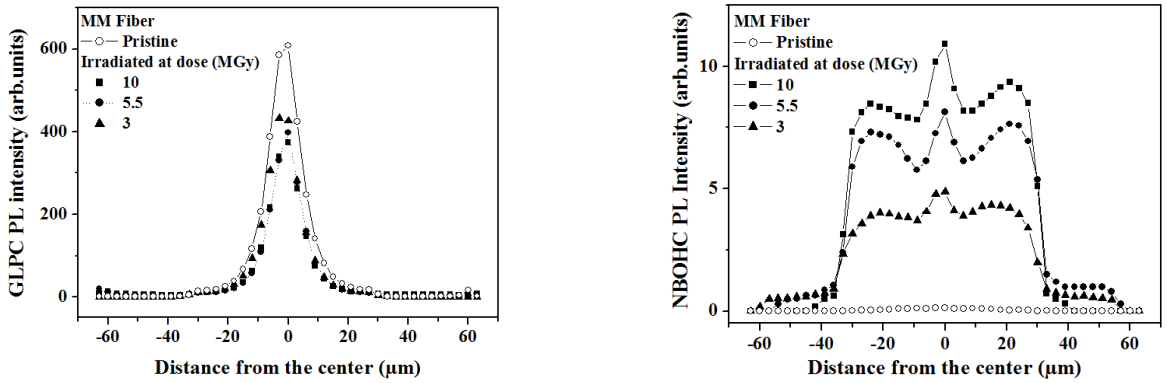

(a) (b)

Figure 6.29: Profile of the PL bands emitted (a) at 3.1 eV (∼400 nm) by GLPCs and (b) at 1.9 eV (∼650 nm) by NBOHCs. The samples are the Ge-doped MM fibers: pristine (empty circles) and γ-irradiated at three doses (full symbols).

6.2.4 Paramagnetic defects

To investigate the radiation effects on the Ge-doped fibers, the electron paramagnetic resonance technique was used to determine the paramagnetic defects and their concentrations. Fig. 6.30 reports the EPR spectra acquired in the multi-mode fibers before and after γ-irradiation at different doses at RT, using the optimal parameters $P_{in} = 1.6$ mW and $H_m = 1$ G. They show that both the fabrication process and the radiation give rise to paramagnetic defects whose concentration increases with increasing dose. These spectra are constituted by the overlap of different signals, as SiE′ and GeE′, whose presence is suggested by the peaks at 3454 G and 3465 G, respectively. As a consequence, to obtain the concentration of the Ge-related defects, a deconvolution of the measured spectra was realized using the reference signals of the Ge(1), Ge(2) and GeE′ defects, shown in fig. 6.31 and obtained by Alessi [144] in samples with similar concentration (∼20 wt% of Ge). As SiE′ signal was used a distorted version of the spectrum already shown in fig. 6.15(b), because of the used high values for the parameters. The SiE′ concentration was obtained by obtain good SiE′ spectra with $P_{in} = 8 \cdot 10^{-4}$ mW and $H_m = 0.1$ G.

Fig. 6.32 reports the concentrations of the Ge-related defects and the SiE′: they increase with the dose without showing a saturating tendency, up to a value of about 10^{17} cm^{-3} at the 10 MGy dose. As it is clear from the absence of the feature around 3485 G in the EPR spectra of fig. 6.30, the Ge(2) center is not created under γ-irradiation in our samples. Moreover, the doublet of 119 G characterizing the H(II) defect, structurally identical to the H(I) center apart from the substitution of Si with Ge, was not observed.

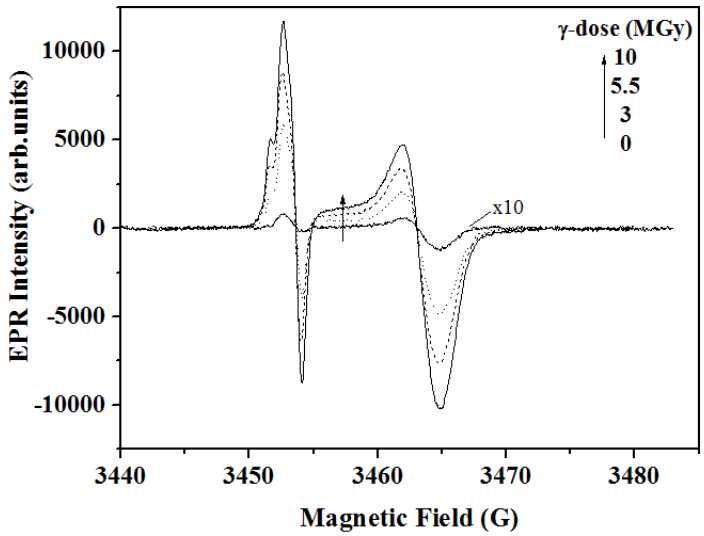

Figure 6.30: EPR spectra of the Ge-doped multi-mode fibers pristine and γ-irradiated at different doses. Parameters for the spectra acquisition: P_{in} = 1.6 mW (attenuation of 23 dB) and H_m = 1 G.

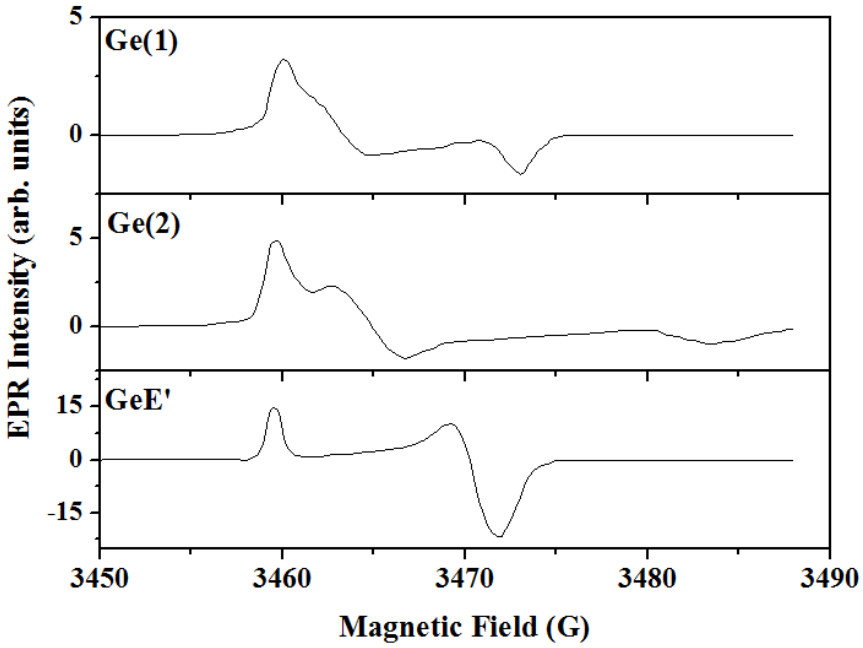

Figure 6.31: EPR signal associated with the Ge-related defects: Ge(1), Ge(2) and GeE′ [144].

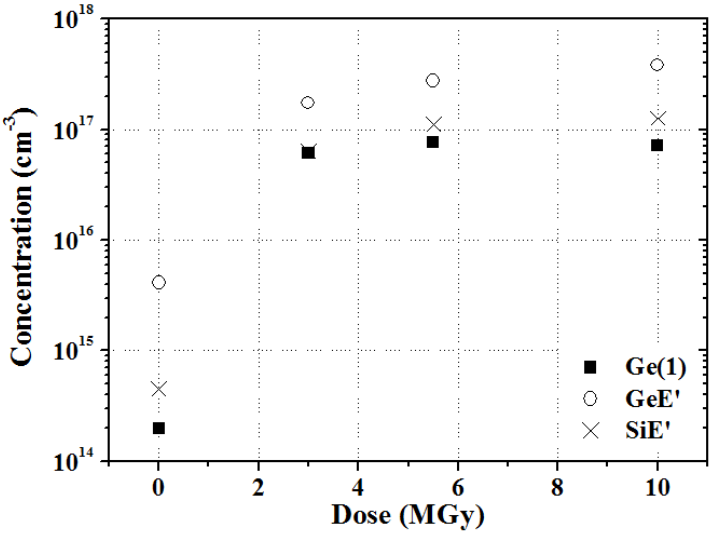

Figure 6.32: Defect concentration of the Ge-doped multi-mode fiber, as a function of the γ-radiation dose. The SiE′ concentration was calculated from spectra recorded with $P_{in} = 8 \cdot 10^{-4}$ mW and $H_m = 0.1$ G. The error coincides with the point dimension.

6.2.5 Conclusions

The γ-radiation induces in the Ge-doped fibers defects related both to Si and to Ge atoms; some paramagnetic defects, such as SiE′, GeE′, Ge(1), Ge(2) and H(II), were investigated with the EPR technique; other defects, as GeX, NBOHC and GLPC, through their absorption and PL bands. All these defects are created during the irradiation, except for the GLPC, whose concentration decreases, and the Ge(2) and H(II), that were not observed. The absence of the Ge(2) center in highly Ge-doped samples was already observed by Alessi [144] and it disagrees with the model according to which the Ge(2) has a Ge(1)-like structure modified by the presence of a second Ge atom, in favor of the other model which considers the Ge(2) an ionized GLPC. Finally, the reduction of the GLPCs induced by radiation can not be due to the generation of Ge(2) or H(II) centers; probably, they convert in neutral oxygen vacancies, like ≡Ge-T≡ (where T is an atom of Si or Ge), that are precursors of E′ centers [180]:

$$= \mathrm{Ge}^{\bullet\bullet} + > \mathrm{T} < \ \rightarrow \ \equiv \mathrm{Ge} - \mathrm{T} \equiv \tag{6.10}$$

Ge-NBOHC

The PL band around 1.9 eV was studied in Ge-doped fibers, where, thanks to the time-resolved photoluminescence technique, another contribution was observed beyond that attributed to the Si-NBOHC. This PL is likely due to the Ge-NBOHC.

- Under excitation at 3.44 eV, since the Si-NBOHC is only weakly excited, the PL band mainly due to the Ge-NBOHC is peaked at 1.86 eV, in agreement with the position of the PL band observed by Skuja et al. in GeO_2 bulk [177].
- The decay of this PL can be described by a stretched exponential, $\exp\left(-(t\ \tau)^{\beta}\right)$, where $\tau = (4.4 \pm 0.7)\ \mu$s and $\beta = 0.83 \pm 0.04$; however, a dependence of these parameters on the excitation energy was observed.
- The visible PLE spectrum of this defect was estimated: it is constituted by an asymmetric band peaked around ∼1.93 eV, with FWHM of ∼0.14 eV, so at lower energies than the excitation band of the Si-NBOHC.

To conclude, we compare the response of two types of fibers, doped with Ge or F, under γ-radiation. The RIA is higher in the Ge-doped fiber and it is more important with decreasing wavelength. It is well known that the higher attenuation of the Ge-doped fiber in the UV-Vis region of the spectrum is due to the Ge-related defects; however, as concerns the IR region, the origin of the OA is still uncertain. Our results let conclude that the F-doped fibers are more suitable for the application in a very harsh environment such as a nuclear reactor core.
The high RIA degrades the performances of the fiber Bragg grating sensor. Around 1550 nm, spectral range of working of FBGs, the RIA in the F-doped fiber is two times smaller than in the Ge-doped one after a γ-dose of only 10 MGy. For the application in a nuclear reactor core, the total γ-dose corresponding to a fuel cycle is one order of magnitude higher than the considered value, without considering the neutrons effects. So, the use of the Ge-doped fibers can not be considered in such an environment. Moreover, as the NIR OA origin is unknown, any solution can be easily adopted to decrease its contribution.

Dans ce chapitre, nous comparons, sous rayonnement gamma, la réponse des deux types de fibres, dopées au germanium et au fluor. L'atténuation induite par irradiation (RIA) est plus élevée dans la fibre dopée au germanium et elle est d'autant plus importante qu'on se décale vers le bleu. Il est bien connu que la forte atténuation de la fibre dopée au germanium dans la région spectrale UV-visible est due aux défauts liés au germanium ; toutefois, en ce qui concerne la région IR, l'origine de l'atténuation est encore incertaine. Nos résultats permettent de conclure que les fibres dopées au fluor sont plus adaptées pour l'application dans un environnement très sévère, comme le coeur d'un réacteur nucléaire. La grande atténuation induite par l'irradiation dégrade les performances du capteur à réseau de Bragg. Autour de 1550 nm, plage de longueurs d'ondes d'utilisation des FBG, la RIA dans la fibre dopée au fluor est deux fois plus faible que dans la fibre au germanium après une dose de seulement 10 MGy. Pour des applications au coeur d'un réacteur nucléaire, la dose gamma totale correspondant à un cycle combustible est un ordre de grandeur plus importante sans compter les effets du flux de neutrons. De ce fait, l'utilisation des fibres dopées au germanium ne peut être envisagée dans un tel environnement d'autant plus que l'origine de l'absorption dans le proche infrarouge n'est pas bien établie pour envisager de supprimer ses causes.

In questo capitolo, confrontiamo la risposta di due tipi di fibre, drogate con germanio o fluoro, sotto irraggiamento gamma. L'attenuazione indotta dalla radiazione (RIA) è maggiore nella fibra drogata con germanio rispetto a quella drogata con fluoro e questo effetto è più importante al diminuire della lunghezza d'onda. È noto che la maggiore attenuazione indotta nella fibra drogata con germanio nella regione UV-Vis dello spettro è dovuta ai difetti del germanio; tuttavia, per quanto riguarda la regione IR, l'origine dell'assorbimento non è stata ancora chiarita. Questi risultati ci permettono di concludere che le fibre drogate con il fluoro sono più adatte per l'applicazione in un ambiente estremo come il nucleo di un reattore nucleare.
L'elevato valore della RIA influenza le prestazioni del sensore a reticolo di Bragg. Attorno a 1550 nm, regione spettrale di funzionamento dei reticoli, l'attenuazione della fibra drogata con fluoro è quasi due volte inferiore al valore ottenuto in quella drogata con germanio dopo una dose di solo 10 MGy. Per l'applicazione nel nucleo di un reattore nucleare, gli effetti della dose gamma corrispondente a un ciclo di combustibile, che è un ordine di grandezza superiore al valore considerato, e dei neutroni potrebbero peggiorare le prestazioni delle fibre drogate con germanio, rispetto a quelle drogate con fluoro. Inoltre, visto che l'origine dell'assorbimento nella regione NIR non è noto, non si può facilmente adottare nessuna soluzione per diminuirne il contributo.

Conclusions and Perspectives

With this thesis we pursued the aim to realize a temperature sensor based on the Fiber Bragg Grating technology and suitable for a very harsh environment, with high γ-dose and high temperature. This objective has been achieved. The grating was written in a radiation-hard fiber, doped only with fluorine, by high intensity femto-second radiation at 800 nm.

First, the results highlighted that the grating resistance at high temperature (up to 750°C) depends strongly on the parameters of the grating inscription. In order to obtain a grating resistant to high temperatures, two conditions must be satisfied:

- the grating strength must be as high as possible but without deforming the peak shape, as saturating the peak or causing too many losses in the cladding;
- the laser power to use must be high, in our case it has been chosen 500 mW (power density in front of the phase mask around 1.7 kW cm^{-2}): it was demonstrated that two gratings written with two different laser power, up to the same value for the initial amplitude, show different behavior during the thermal treatment.

The origin of the grating depends on the laser power and the inscription time, it can be defects or densification, and the thermal response depends on this.

Secondly, the radiation sensitivity of these gratings was tested at room temperature, as a function of the pre-annealing temperature: it was found that the higher is the temperature, the more resistant is the grating.

Finally, we realized a sensor based on a FBG working at 230°C up to an accumulated dose of 3 MGy with an error on the temperature measurement of $\sim$1°C.

Besides the study on FBGs, a part of my PhD was dedicated to the degradation of the fiber transmission: RIA measurements were realized in the visible-IR range of the spectrum and other techniques, such as EPR, PL and Raman, were used in order to identify the radiation effects.

In the F-doped fibers, the radiation creates more NBOHCs than PORs, likely because of the higher concentration of the drawing induced strained bonds, precursors of the NBOHCs. The concentrations of the E′, NBOHC and POR defects are of the same order of magnitude.

Finally, the origin of the asymmetric absorption band around 2 eV was clarified, thanks to its correlation with a photoluminescence emission: it is due to a single defect, that is the Si-NBOHC. A study dedicated to the photoluminescence of this defect showed that it does not change its spectroscopic characteristics, such as lifetime and excitation spectrum, if it is present in fiber or in bulk. A similar study was realized for the Ge-NBOHC.

Even if during this thesis work a temperature sensor suitable for the aimed application has been found, more tests have to be still performed or are in progress: the grating has to be tested under mixed radiation (γ-rays and neutrons) combined to high temperatures ($\sim$550°C) for a long period to reproduce the radiative environment of a Sodium-cooled fast reactor. A test is currently in progress in collaboration with Dr. G. Cheymol and the CEA in Saclay (France): some gratings are being irradiated inside a reactor, up to the neutron fluence of a fuel cycle.

Moreover, our research group has recently shown that the response of optical fibers can have a strong dependence on the thermodynamic path. It has been commonly believed that irradiation followed by heat treatment at a temperature T produced the same effect as the same irradiation at the temperature T; in contrast, it has been shown that these two thermodynamic paths may lead to completely different responses [181]. A study in this direction on fibers and FBGs must be made at temperatures higher than that achieved in this thesis (230°C). This study is currently facing the lack of accessibility to such a radiation environment.

Conclusions et perspectives

L'objectif visé par cette thèse porte sur la réalisation d'un capteur de température à base de réseau de Bragg photo-inscrit sur une fibre permettant de fonctionner dans un environnement radiatif sévère ; forte dose de rayonnement gamma et forte température. Cet objectif a été atteint. Le réseau a été inscrit moyennant un laser à impulsions femtosecondes à 800 nm dans une fibre durcie au rayonnement ionisant.

Notre étude a montré que la résistance du réseau à haute température (jusqu'à 750°C) dépend fortement des paramètres d'inscription. Afin d'obtenir un réseau résistant aux hautes températures, deux conditions doivent être vérifiées :

- l'amplitude du pic doit être la plus élevée possible, mais sans déformer la forme du pic ; sans saturer le pic ou causer trop de pertes dans la gaine ;
- la puissance du laser à utiliser doit être élevée, dans notre cas, il a été choisi 500 mW (la densité de puissance avant le masque de phase d'environ 1.7 kW cm^{-2}) : il a été démontré que deux réseaux de même valeur de l'amplitude inscrits avec deux différentes puissances du laser présentent des comportements différents au cours du traitement thermique.

La force du réseau dépend de la puissance du laser et du temps d'inscription, elle peut être liée à la formation de défauts ou à la densification de la matrice.

La sensibilité au rayonnement de ces réseaux a été testée à température ambiante, en fonction de la température du prétraitement : il a été constaté que plus la température est élevée, plus le réseau est résistant.

Enfin, nous avons réalisé un capteur à réseau de Bragg permettant de fonctionner à 230°C sous une dose cumulée de 3 MGy avec une erreur induite d'environ 1°C.

En plus de l'étude des FBGs, une partie de ma thèse a été consacrée à l'étude de la dégradation de la transmission de la fibre sous rayonnement ionisant. Les mesures d'atténuation optique ont été réalisées dans les régions spectrales visible et infrarouge. D'autres techniques de caractérisation ont été utilisées : la résonance paramagnétique électronique, la photoluminescence et le Raman.

Dans les fibres dopées au fluor, le rayonnement crée plus de NBOHCs que de PORs, probablement à cause de la concentration plus élevée de liaisons contraintes induites par le fibrage, précurseurs des NBOHCs. Les concentrations des défauts, comme E′, NBOHC et POR sont du même ordre de grandeur.

Enfin, l'origine de la bande d'absorption asymétrique centrée à environ 2 eV a été

clarifiée, grâce à sa corrélation avec une bande de photoluminescence. Elle est due à un seul défaut ; le Si-NBOHC. Une étude consacrée à la photoluminescence de ce défaut a montré que ses caractéristiques spectroscopiques (durée de vie et spectre d'excitation) ne changent pas lors du passage de la silice massive aux fibres. Une étude similaire a été réalisée sur le Ge-NBOHC.

Même si nous avons réalisé au cours de ce travail de thèse un capteur de température répondant au cahier de charges lié à un profil d'utilisation demandé par la société AREVA, plusieurs études complémentaires sont en cours ou doivent être réalisées. Le réseau doit être testé sous un rayonnement mixte combinant à une température élevée (∼550°C) radiations gamma et flux de neutrons pendant une longue période pour reproduire ou au moins se rapprocher le plus possible de l'environnement radiatif propre aux réacteurs à neutrons rapides refroidis au sodium. Un test est actuellement en cours en collaboration avec Dr G. Cheymol et le CEA - Saclay (France). Quelques réseaux sont en train d'être irradiés dans un réacteur pour atteindre les fluences compatibles avec un cycle combustible.

Par ailleurs notre groupe de recherche a montré récemment que la réponse des fibres optiques peut présenter une forte dépendance du chemin thermodynamique. Alors qu'il était communément admis qu'une irradiation suivie d'un traitement thermique à une température T produisaient le même effet que la même irradiation à la température T, il a été montré que ces deux chemins thermodynamiques peuvent conduire à des réponses complétement différentes [181]. Une étude dans ce sens sur la fibre et le FBG retenus doit être réalisée à des températures supérieures à celle atteinte dans la présente thèse (230°C). Cette étude se trouve actuellement confronté à l'absence d'accessibilité à un tel environnement radiatif.

Conclusioni e prospettive

Con questa tesi abbiamo perseguito l'obiettivo di realizzare un sensore di temperatura basato sulla tecnologia dei reticoli di Bragg (Fiber Bragg Grating o FBG) e adatto ad un ambiente estremo, con elevata dose di raggi gamma e alta temperatura. L'obiettivo è stato raggiunto. Il reticolo è stato iscritto in una fibra resistente alla radiazione drogata con fluoro, da radiazione laser a 800 nm, pulsata al femtosecondo, di alta intensità.

In primo luogo, i risultati hanno evidenziato che la resistenza del reticolo ad alta temperatura (fino a 750°C) dipende fortemente dai parametri d'iscrizione del reticolo. Per ottenere un reticolo resistente alle alte temperature, devono essere soddisfatte le seguenti due condizioni:

- l'ampiezza del picco di Bragg deve essere la più grande possibile, ma senza deformarne la forma, come per esempio saturando il picco o causando troppe perdite nel cladding;
- la potenza del laser da utilizzare deve essere elevata, nel nostro caso è stata scelta pari a 500 mW (densità di potenza prima della maschera di fase pari a circa 1.7 kW cm^{-2}): è stato infatti dimostrato che due reticoli iscritti con due differenti valori della potenza del laser, fino allo stesso valore per l'ampiezza iniziale, mostrano differenti comportamenti durante il trattamento termico.

La risposta termica dipende, attraverso la potenza del laser e il tempo d'iscrizione, dall'origine del reticolo che può essere legata ai difetti o alla densificazione.

In secondo luogo, la sensibilità alla radiazione di questi reticoli è stata testata a temperatura ambiente, in funzione della temperatura del pre-trattamento: si è constatato che più elevata è la temperatura, più resistente è il reticolo.

Infine, è stato realizzato un sensore a reticolo di Bragg funzionante a 230°C fino ad una dose accumulata pari a 3 MGy con un errore indotto sulla misura di temperatura di circa 1°C.

Oltre allo studio sui FBG, una parte del mio dottorato è stata dedicata all'attenuazione della trasmissione della fibra: misure di RIA sono state realizzate nella parte visibile-IR dello spettro e altre tecniche, come EPR, PL e Raman, sono state utilizzate per identificare gli effetti dell'irraggiamento.

Nelle fibre drogate con fluoro, la radiazione crea NBOHC a causa dell'elevata concentrazione di legami "stressed" indotti durante il tiraggio della fibra. Inoltre, le concentrazioni di E′, NBOHC e POR sono dello stesso ordine di grandezza.

Infine, l'origine della banda di assorbimento asimmetrica, centrata a 2 eV, è stata chiarata grazie alla sua correlazione con unemissione di fotoluminescenza: essa è dovuta ad un solo difetto, cioè NBOHC. Uno studio dedicato alla fotoluminescenza di questo difetto ha mostrato che le sue caratteristiche spettroscopiche, quali tempo di vita e spettro di eccitazione, sono confrontabili fra le fibre e le preforme "bulk". Uno studio simile è stato realizzato per il Ge-NBOHC.

Anche se durante il lavoro di tesi è stato realizzato un sensore di temperatura adatto all'applicazione desiderata, i risultati ottenuti hanno aperto numerose prospettive che meritano di essere investigate. I reticoli devono essere testati sotto radiazione mista (raggi gamma e neutroni) combinata ad alte temperature ($\sim$550°C) per un lungo periodo, per riprodurre l'ambiente radiativo di un reattore nucleare veloce raffreddato con sodio. Un test è attualmente in corso in collaborazione con il Dott. G. Cheymol e il CEA a Saclay (Francia): alcuni reticoli sono stati irradiati all'interno di un reattore, fino ad un flusso di neutroni compatibile con un ciclo di combustibile.

Inoltre, il nostro gruppo di ricerca ha recentemente dimostrato che la risposta delle fibre ottiche può dipendere dal percorso termodinamico. Mentre si credeva che l'irraggiamento seguito da un trattamento termico a una temperatura T produceva lo stesso effetto dello stesso irraggiamento alla temperatura T, è stato dimostrato che questi due percorsi possono portare a risposte completamente differenti [181]. Uno studio in questa direzione sulle fibre e i FBG deve essere realizzato a delle temperature superiori a quelle raggiunte in questa tesi (230°C). Questo studio si sta confrontando con la mancanza di accessibilità a un tale ambiente radiativo.

List of related papers and communications

List of papers

1. L. Vaccaro, M. Cannas, S. Girard, A. Alessi, A. Morana, A. Boukenter, Y. Ouerdane and R. Boscaino, *Influence of fluorine on the fiber resistance studied through the Non Bridging Oxygen Hole Center related luminescence*, Journal of Applied Physics **113** (19), 193107 (2013).

2. A. Morana, M. Cannas, S. Girard, A. Boukenter, L. Vaccaro, J. Périsse, J.-R. Macé, Y. Ouerdane and R. Boscaino, *Origin of the visible absorption in radiation-resistant optical fibers*, Optical Materials Express **3** (10), pp.1769-1776 (2013).

List of communications

International conferences

1. A. Morana, A. Boukenter, Y. Ouerdane, S. Girard, M. Cannas, J. Périsse, J.-R. Macé, *Thermal bleaching of gamma-induced-defects in optical fibers*, 9th Symposium "SiO2 - Advanced Dielectrics and Related Devices", Hyères, France, June 2012, Oral contribution.

2. S. Girard, A. Morana, C. Marcandella, J. Périsse, J-R. Macé, A. Boukenter, P. Paillet, M. Gaillardin, Y. Ouerdane, M. Cannas, R. Boscaino, H*arsh environments (temperature, radiations) effects on silica-based optical fibers and components*, "Advancements in Nuclear Instrumentation Measurement Methods and their Applications" (ANIMMA), Marseille, France, June 2013, Oral Contribution.

3. S. Girard, C. Marcandella, A. Morana, J. Périsse, D. Di Francesca, P. Paillet, J-R. Macé, A. Boukenter, M. Leòn, M. Gaillardin, N. Richard, M. Raine, S. Agnello, M. Cannas and Y. Ouerdane, *Combined High Dose and Temperature Radiation Effects on Multimode Silica-based Optical Fiber*, "Nuclear and Space Radiation Effects

Conference" (NSREC), San Francisco, California, July 2013, Oral Contribution.

National conferences (France)

1. A. Morana, A. Boukenter, Y. Ouerdane, S. Girard, M. Cannas and M. Marin, *Comportement de fibres optiques et réseaux de Bragg sous forte dose gamma et à haute température*, 2nd Journées "Tenue des fibres optiques en Milieu Radiatif", Saint-Etienne, November 2011, Oral contribution

2. A. Morana, A. Boukenter, S. Girard, J.-R. Macé, Emmanuel Marin, Y. Ouerdane et J. Périsse, *Tenue des fibres optiques à base de silice sous rayonnement gamma*, 32th Journées Nationales d'optique guidée (JNOG), Lyon, July 2012, Poster contribution.

3. A. Morana, M. Cannas, A. Boukenter, Y. Ouerdane, S. Girard, J.-R. Macé and J.Périsse, *Etude spectroscopique des centres NBOH induits sous irradiation gamma dans des fibres multimodes*, 3rd Journées sur les Fibres Optiques en Milieu Radiatif, Nice, November 2012, Oral contribution.

4. A. Morana, A. Boukenter, M. Cannas, S. Girard, J. Périsse, J.-R. Macé, C. Marcandella, P. Paillet et Y. Ouerdane, *Etude spectroscopique de fibres durcies pour un environnement radiatif sévère*, 4th Journées sur les Fibres Optiques en Milieu Radiatif, Lannion, November 2013, Oral contribution.

Bibliography

[1] G. Keiser, "Optical Fiber Communications", McGraw-Hill Internation Editions (1991).

[2] G. P. Agrawal, "Fiber-Optic Communication Systems", Wiley Interscience (2002).

[3] W.H. Zachariasen, "The atomic arrangement in glass", Journal of the American Chemical Society, **54** (1), pp. 3841-3851 (1932).

[4] A.C. Wright, "Defect-free vitreous networks: the idealized structure of SiO_2 and related glasses" in *Defects in SiO_2 and Related Dielectrics: Science and Tecnology*, Editors: G. Pacchioni, L.Skuja e D.L. Griscom; Kluwer Academic Publishers; pp. 1-35 (2000).

[5] F.L. Galeener, R.A. Barrio, E. Martinez and R.J. Elliott, "Vibrational decoupling of rings in amorphous solids", Physical Review Letters, **53** (25), pp. 2429-2432 (1984).

[6] F.L. Galeener, "Planar rings in glasses", Solid State Communications, **44** (7), pp. 1037-1040 (1982).

[7] L. Skuja, M. Hirano, H. Hosono and K. Kajihara, "Defects in oxide glasses", Physica Status Solidi (c), **2** (1), pp. 15-24 (2005).

[8] D.L. Griscom, "Self-trapped holes in amorphous silicon dioxide", Physical Review B, **40** (6), pp. 4224-4227 (1989).

[9] S. Girard, J. Kuhnhenn, A. Gusarov, B. Brichard, M. Van Uffelen, Y. Ouerdane, A. Boukenter and C. Marcandella, "Radiation effects on silica-based optical fibers: recent advances and future challenges", IEEE Transactions on Nuclear Science, **60** (3), pp. 2015-2036 (2013).

[10] G.S. Henderson, D.R. Neuville, B. Cochain and L. Cormier, "The structure of GeO_2SiO_2 glasses and melts: a Raman spectroscopy study", Journal of Non-Crystalline Solids, **355**, pp. 468-474 (2009).

[11] L. Skuja, "Isoelectronic series of twofold coordinated Si, Ge, and Sn atoms in glassy SiO_2: a luminescence study", Journal of Non-Crystalline Solids, **149** (1-2), pp. 77-95 (1992).

[12] V.B. Neustruev, "Colour centres in germanosilicate glass and optical fibres", Journal of Physics Condensed Matter, **6**, pp. 6901-6936 (1994).

[13] E.J. Friebele and D.L. Griscom, "Color centers in glass optical fiber waveguides", Materials Research Society Symposium Proceedings, **61**, pp. 319-331 (1986).

[14] M. Fujimaki, T. Watanabe, T. Katoh, T. Kasahara, N. Miyazaki, Y. Ohki and H. Nishikawa, "Structures and generation mechanisms of paramagnetic centers and absorption bands responsible for Ge-doped SiO_2 optical-fiber gratings", Physical Review B, **57** (7), pp. 3920-3926 (1998).

[15] E.V. Anoikin, V.M. Mashinsky, V.B. Neustruev and Y.S. Sidorin, "Effects of exposure to photons of various energies on transmission of germanosilicate optical fiber in the visible to near IR spectral range", Journal of Non-Crystalline Solids, **179**, pp. 243-253 (1994).

[16] D.L. Griscom, "γ-ray induced optical attenuation in Ge-doped silica fiber image guides", Journal of Applied Physics, **78** (11), pp. 6697-6704 (1995).

[17] S. Girard, "Analyse de la reponse des fibres optiques soumises à divers environnements radiatifs", PhD thesis, Université de Saint Etienne, France (2003).

[18] F. Piao, W.G. Oldham and E.E. Haller, "The mechanism of radiation-induced compaction in vitreous silica", Journal of Non-Crystalline Solids, **276**, pp. 61-71 (2000).

[19] W. Primak and E. Edwards, "Radiation-induced dilatations in vitreous silica", Physical Review, **128** (6), pp. 2580-2588 (1962).

[20] A.I. Gusarov and S.K. Hoeffgen, "Radiation effects on fiber gratings", IEEE Transactions on Nuclear Science, **60** (3), pp. 2037-2053 (2013).

[21] B. Brichard, P. Borgermans, A. Fernandez Fernandez, K. Lammens and M. Decréton, "Radiation effect in silica optical fiber exposed to intense mixed neutron gamma radiation field", IEEE Transactions on Nuclear Science, **48** (6), pp. 2069-2073 (2001).

[22] A. Kersey, "A review of recent developments in fiber optic sensor technology", Optical Fiber Technology **2**, pp. 291-317 (1996).

[23] G.F. Fernando, D. Webb and P. Ferdinand, "Optical-fiber sensors", Optical-Fiber Sensors; MRS Bulletin May 2002, pp. 359-364 (2002).

[24] Y.B. Yu and W.K. Chow, "Review on an advanced high-temperature measurement technology: the optical fiber thermometry", Journal of Thermodynamics, **2009** 823482 (2009).

[25] F. Jensen, T. Kakuta, T. Shikama, T. Sagawa, M. Narui and M. Nakazawa, "Optical measurements of high temperatures for material investigations in nuclear reactor environments", Fusion Engineering and Design, **42**, pp. 449-454 (1998).

[26] R.R. Dils, "High-temperature optical fiber thermometer", Journal of applied Physics, **54** (3), pp. 1198-1201 (1993).

[27] G. Wang and X.Y. Wang, "Temperature measurement technology with sapphire fiber blackbody sensor", International Conference on Optics Photonics and Energy Engineering (OPEE), Wuhan (China), **1**, pp. 138-141 (2010).

[28] J.P. Dakin, "Distributed optical fiber sensors", Proc. SPIE **1797**, Distributed and Multiplexed Fiber Optic Sensors II, Boston (USA), 76 (1993).

[29] Y. Li, F. Zhang and T. Yoshino, "Wide temperature-range Brillouin and Rayleigh optical-time-domain reflectometry in a dispersion-shifted fiber", Applied Optics, **42** (19), pp. 3772-3775 (2003).

[30] D.K. Gifford, B.J. Soller, M.S. Wolfe and M.E. Froggatt, "Distributed fiber-optic temperature sensing using Rayleigh backscatter", 31st European Conference on Optical Communication (ECOC 2005), **3**, pp. 511-512 (2005).

[31] A.K. Sang, M.E. Froggatt, D.K. Gifford, S.T. Kreger and B.D. Dickerson, "One centimeter spatial resolution temperature measurements in a nuclear reactor using Rayleigh scatter in optical fiber", IEEE Journal Sensors, **8** (7), pp. 1375-1380 (2008).

[32] J. R. Ferraro, K. Namamoto, and C. W. Brown, "Introductory Raman Spectroscopy", Academic Press (2003).

[33] D. Hwang, D.-J. Yoon, I.-B. Kwon, D.-C. Seo and Y. Chung, "Novel auto-correction method in a fiber-optic distributed-temperature sensor using reflected anti-Stokes Raman scattering", Optics Express **18** (10), pp. 9747-9754 (2010).

[34] A. Fernandez Fernandez, P. Rodeghiero, B. Brichard, F. Berghmans, A.H. Hartog, P. Hughes, K. Williams and A.P. Leach, "Radiation-tolerant Raman distributed temperature monitoring system for large nuclear infrastructures", IEEE Transactions on Nuclear Science, **52** (6), pp. 2689-2694 (2005).

[35] K. Suh and C. Lee, "Auto-correction method for differential attenuation in a fiber-optic distributed-temperature sensor", Optics Letters, **33** (16), pp. 1845-1847 (2008).

[36] J.P. Dakin, D.J. Pratt, G.W. Bibby and J.N. Ross, "Distributed anti-Stokes ratio thermometry", Proc. International Conference on Optical Fiber Sensors (1985).

[37] D. Liu, S. Liu and H. Liu, "Temperature performance of Raman scattering in data fiber and its application in distributed temperature fiber-optic sensor", Frontiers of Optoelectronics in China **2** (2), pp. 159-162 (2009).

[38] Z.-X. Zhang, J.-F. Wang, H.-L. Liu, H.-F. Xu, B.-Z. Dai, C.-X. Li, L.-X. Li, D. Geng and S.K. Insoo, "The long range distributed fiber Raman photon temperature sensor", OptoElectronics Letters **3** (6), pp. 404-405 (2007).

[39] S. Kher, G. Srikant, S. Chaube, A.L. Cjakraborty, T.P.S. Nathan and D.D. Bhawalkar, "Design, development and studies on Raman-based fibre-optic distributed temperature sensor", Current Science **83** (11), pp. 1365-1368 (2002).

[40] D.A. Thorncraft, M.G. Sceats and S.B. Poole, "An ultra high resolution distributed temperature sensor", Proc. 8th Optical Fiber Sensors Conference, New York (USA), pp. 258-261 (1991).

[41] F. Jensen, E. Takada, M. Nakazawa, H. Takahashi, T. Iguchi, T. Kakuta and S. Yamamoto, "Development of a distributed monitoring system for temperature and coolant leakage", Proc. IAEAOECD/NEANSC Incore 96 Meeting (1996).

[42] F.B.H. Jensen, E. Takada, M. Nakazawa, T. Kakuta and S. Yamamoto, "Consequences of radiation effects on pure-silica-core optical fibers used for Raman-scattering-based temperature measurements", IEEE Transactions on Nuclear Science, **45** (1), pp. 50-58 (1998).

[43] A. Kimura, E. Takada, K. Fujita, M. Nakazawa, H. Takahashi and S. Ichige, "Application of a Raman distributed temperature sensor to the experimental fast reactor JOYO with correction techniques", Measurement Science and Technology **12**, pp. 966-973 (2001).

[44] L. Thèvenaz, "Novel schemes for optical signal generation using laser injection locking with application to Brillouin sensing", Frontiers of Optoelectronics in China, **3** (1), pp. 13-21 (2010).

[45] M. Niklès, L. Thèvenaz and P.A. Robert, "Simple distributed fiber sensor based on Brillouin gain spectrum analysis", Optics Letters, **21** (10), pp. 758-760 (1996).

[46] W. Kaiser and M. Maier, "Laser Handbook", North-Holland Publications (1973).

[47] M.A. Soto, P.K. Sahu, G. Bolognini and F. Di Pasquale, "Brillouin-based distributed temperature sensor employing pulse coding", IEEE Sensors Journal, **8** (3), pp. 225-226 (2008).

[48] M.N. Alahbabi, Y.T. Cho and T.P. Newson, "100 km distributed temperature sensor based on coherent detection of spontaneous Brillouin backscatter", Measurement Science and Technology, **15**, pp. 1544-1547 (2004).

[49] T. Kurashima, T. Horiguchi and M. Tateda, "Distributed-temperature sensing using stimulated Brillouin scattering in optical silica fibers", Optics Letters, **15** (18), pp. 1038-1040 (1990).

[50] X. Bao, D.J. Webb and D.A. Jackson, "Combined distributed temperature and strain sensor based on Brillouin loss in an optical fiber", Optics Letters, **19** (2), pp. 141-143 (1994).

[51] X. Bao, D.J. Webb and D.A. Jackson, "32-km distributed temperature sensor based on Brillouin loss in an optical fiber", Optics Letters, **18** (18), pp. 1561-1563 (1993).

[52] D. Alasia, A. Fernandez Fernandez, L. Abrardi, B. Brichard and L. Thvenaz, "The effects of gamma-radiation on the properties of Brillouin scattering in standard Ge-doped optical fibres", Measurement Science and Technology, **17**, pp. 1091-1094 (2006).

[53] X. Phéron, "Durabilité d'un capteur à fibre optique sous environnement radiatif", PhD thesis, Université de Saint Etienne, France (2013).

[54] S.W. James and R.P. Tatam, "Optical fibre long-period grating sensors: characteristics and application", Measurement Science and Technology, **14**, pp. R49-R61 (2003).

[55] V. Bhatia and A.M. Vengsarkar, "Optical fiber long-period grating sensors", Optics Letters, **21** (9), pp. 692-694 (1996).

[56] K. O. Hill and G. Meltz, "Fiber Bragg grating technology: Fundamentals and Overview", Journal of Lightwave Technology, **15** (8), pp. 1263-1276 (1997).

[57] K. O. Hill, Y. Fujii, D. C. Johnson and B.S. Kawasaki, "Photosensitivity in optical fiber waveguides: Application to reflection filter fabrication", Applied Physics Letters, **32** (10), pp. 647-649 (1978).

[58] T.T. Tam, D.Q. Trung, T.A. Vu, L.H. Minh and D.N. Chung, "Investigation of the embedded fiber bragg grating temperature sensor", VNU Journal of Science, Mathematics - Physics, **23**, pp. 237-242 (2007).

[59] Y. Zhan, H. Cai, R. Qu, S. Xiang, Z. Fang and X. Wang, "Fiber Bragg grating temperature sensor for multiplexed measurement with high resolution", Optical Engineering, **43** (10), pp. 2358-2361 (2004).

[60] S.-L. Tsao, J. Wu and B.-C. Yeh, "High-resolution neural temperature sensor using fiber Bragg gratings", IEEE Journal of Quantum Electronics, **35** (11), pp. 1590-1956 (1999).

[61] T.-E. Tsai, G.M. Williams and E.J. Friebele, "Index structure of fiber Bragg gratings in Ge-SiO_2 fibers", Optics Letters, **22** (4), pp. 224-226 (1997).

[62] P. Saidi Reddy, R.L.N. Sai Prasad, K. Srimannarayana, M. Sai Shankar and D. Sen Gupta, "A novel method for high temperature measurements using fiber Bragg grating sensor", Optica Applicata, **XL** (3), pp. 685-692 (2010).

[63] A.I. Gusarov, D.S. Starodubov, F. Berghmans, O. Deparis, Y. Defosse, A. Fernandez Fernandez, M. Décreton, P. Mégret and M. Blondel, "Comparative study of MGy dose level γ-radiation effect on FBGs written in different fibres", Proc. SPIE **3746**, International Conference on Optical Fiber Sensors (OFS-13), Kyongju (Korea), pp. 608-611 (1999).

[64] F. Berghmans, A. Fernandez Fernandez, B. Brichard, F. Vos, M. Decréton, A. Gusarov, O. Deparis, P. Mégret, M. Blondel, S. Caron and A. Morin, "Radiation hardness of fiber-optic sensors for monitoring and remote handling applications in nuclear environments", Proc. SPIE **3538**, Process Monitoring with Optical Fibers and Harsh Environment Sensors, 28 (1998).

[65] A. Fernandez Fernandez, A. Gusarov, B. Brichard, M. Decrton, F. Berghmans, P. Mégret and A. Delchambre, "Long-term radiation effects on fibre Bragg grating temperature sensors in a low flux nuclear reactor", Measurement Science and Technology, **15**, pp. 1506-1511 (2004).

[66] D. Grobnic, H. Henschel, S.K. Hoeffgen, J. Kuhnhenn, S.J. Mihailov and U. Weinand, "Radiation sensitivity of Bragg gratings written with femtosecond IR lasers", Fiber Optic Sensors and Application VI, Orlando (US), E. Udd, H.H. Du and A. Wang Eds., Proc. SPIE **7316**, pp. 7316-11 (2009).

[67] A.M. Vengsarkar, P.J. Lemaire, J.B. Judkins, V. Bhatia and T. Erdogan, "Long-period fiber gratings as band-rejection filters", Journal of Lightwave Technology, **14**, pp. 58-64 (1996).

[68] V. Bhatia, "Applications of long-period gratings to single and multi-parameter sensing", Optics Express, **4** (11), pp. 457-466 (1999).

[69] F.J. Flaherty, Z. Ghassemlooy, P.S. Mangat and K.P. Dowker, "Temperature characterization of long-period gratings for sensor applications", Microwave and Optical Technology Letters, **42** (5), pp. 402-405 (2004).

[70] Y. Liu, C. Ge, D. Zhao, Z. Liu, Z. Guo, X. Dong and H.Y. Tam, "Long-period fiber grating temperature sensor based on intensity measurement", Acta Photonica Sinica, **28** (4), pp. 356-359 (1999).

[71] Y. Zhang, H. Cai and S. Xiang, Chinese Journal of Lasers, **32**, pp.83 (2005).

[72] S.A. Vasiliev, E.M. Dianov, K.M. Golant, O.I. Medvedkov, A.L. Tomashuk, V.I. Karpov, M.V. Grekov, A.S. Kurkov, B. Leconte and P.Niay, "Performance of Bragg and long-period gratings written in N- and Ge-doped silica fibers under γ-radiation", IEEE Transactions on Nuclear Science, **45** (3), pp. 1580-1583 (1998).

[73] X. Lan, Q. Han, T. Wei, J. Huang, H. Xiao, "Turn-Around-Point Long-Period Fiber Gratings fabricated by CO_2 laser Point-by-Point irradiations", IEEE Photonics Technology Letters, **23** (22), pp. 1664-1666 (2011).

[74] S. Kher, S. Chaubey, R. Kashyap, S.M. Oak, "Turn-Around-Point Long-Period Fiber Gratings (TAP-LPGs) as high-radiation-dose sensors", IEEE Photonics Technology Letters, **24** (9), pp. 742-744 (2012).

[75] H. Henschel, S.K. Hoeffgen, J. Kuhnhenn, S.J. Mihailov and U. Weinand, "High radiation sensitivity of chiral long period gratings", IEEE Transactions on Nuclear Science, **57** (5), pp. 2915-2922 (2010).

[76] E. Udd, "An overview of fiber optic sensors", Review of Scientific Instruments, **66** (8), pp. 4015-4030 (1995).

[77] http://www.gen-4.org/Technology/systems/sfr.htm.

[78] A. Fernandez Fernandez, B. Brichard, F. Berghmans H. El Rabii, M. Fokine and M. Popov, "Chemical composition fiber gratings in a high mixed gamma neutron radiation field", IEEE Transactions on Nuclear Science, **53** (3), pp. 1607-1613 (2006).

[79] A. Othonos and K. Kalli, "Fiber Bragg Gratings: fundamentals and applications in telecommunications and sensing", Artech House (1999).

[80] R. Kashyap, "Fiber Bragg Gratings", Second Edition, Academic Press (2009).

[81] X. Sang, C. Yu and B. Yan, "Bragg gratings in multimode optical fibres and their applications", Journal of Optoelectronics and Advanced Materials, **8** (4), pp. 1616-1621 (2006).

[82] S.A. Slattery, D.N. Nikogosyan and G. Brambilla, "Fiber Bragg grating inscription by high-intensity femtosecond UV laser light: comparison with other existing methods of fabrication", Journal of the Optical Society of America B, **22** (2), pp. 354-361 (2005).

[83] H. Kogelnik, "Coupled wave theory for thick hologram gratings", Bell System Technical Journal, **48** (9), pp. 2909-2947 (1969).

[84] D.K.W. Lam and B.K. Garside, "Characterization of single-mode optical fiber filters", Applied Optics, **20** (3), pp. 440-445 (1981).

[85] T. Erdogan, "Fiber grating spectra", Journal of Lightwave Technology, **15** (8), pp. 1277-1294 (1997).

[86] I.H. Malitson, "Interspecimen comparison of the refractive index of fused silica", Journal of the Optical Society of America, **55** (10), pp. 1205-1209 (1965).

[87] Y. Li, Z. Hua, F. Yan and P. Gang, "Metal coating of fiber Bragg grating and the temperature sensing character after metallization", Optical Fiber Technology, **15**, pp. 391-397 (2009).

[88] K. Krebber, H. Henschel and U. Weinand, "Fibre Bragg gratings as high dose radiation sensors?", Measurement Science and Technology, **17**, pp. 1095-1102 (2006).

[89] S.J. Mihailov, C.W. Smelser, P. Lu, R.B. Walker, D. Grobnic, H. Ding, G. Henderson and J. Unruh, "Fiber Bragg gratings made with a phase mask and 800-nm femtosecond radiation", Optics Letters, **28** (12), pp. 995-997 (2003).

[90] G. Meltz, W.W. Morey and W.H. Glenn, "Formation of Bragg gratings in optical fibers by a transverse holographic method", Optics Letters, **14** (15), pp. 823-825 (1989).

[91] B. Malo, K.O. Hill, F. Bilodeau, D.C. Johnson and J. Albert, "Point by point fabrication of micro-Bragg gratings in photosensitive fibre using single excimer pulse refractive index modification techniques", Electronics Letters, **29**, pp. 1668-1669 (1993).

[92] K. O. Hill, B. Malo, F. Bilodeau, D. C. Johnson and J. Albert, "Bragg gratings fabricated in monomode photosensitive optical fiber by UV exposure through a phase mask", Applied Physics Letters, **62** (10), pp. 1035-1037 (1993).

[93] C.G. Askins, T.-E. Tsai, G.M. Williams, M.A. Putnam, M. Bashkansky and E.J. Friebele, "Fiber Bragg reflectors prepared by a single excimer pulse", Optics Letters, **17** (11), pp. 833-835 (1992).

[94] D.A. Barber and N.H. Rizvi, Proc. SPIE **4941**, "A practical study of the effects of exposure conditions on the quality of fibre Bragg gratings written with excimer and argon-ion lasers", Laser Micromachining for Optoelectronic Device Fabrication, 16 (2003).

[95] B. Malo, J. Albert, K.O. Hill, F. Bilodeau, D.C. Johnson and S. Thériault, "Enhanced photosensitivity in lightly doped standard telecommunication fibre exposed to high fluence ArF excimer laser light", Electronics Letters, **31** (11), pp. 879-880 (1995).

[96] J.-L. Archambault, L. Reekie and P.St.J. Russell, "100% Reflectivity Bragg reflectors produced in optical fibers by single excimer laser pulses", Electronics Letters, **29** (5), pp. 453-455 (1993).

[97] Y. Liu, J.A.R. Williams, L. Zhang and I. Bennion, Optic Letters, **27**, pp. 586-588 (2002).

[98] G. Simpson, K. Kalli, K. Zhou, L. Zhang and I. Bennion, "Formation of type IA fibre Bragg gratings in germanosilicate optical fibre", Electronics Letters, **40** (3), pp. 163-164 (2004).

[99] G. Simpson, K. Kalli, K. Zhou, L. Zhang and I. Bennion, "Blank beam fabrication of regenerated type IA gratings", Measurement Science and Technology, **15**, pp. 1665-1669 (2004).

[100] L. Dong, W. F. Liu and L. Reekie, "Negative-index gratings formed by a 193-nm excimer laser", Optics Letters, **21** (24), pp. 2032-2034 (1996).

[101] S. Pissadakis and M. Konstantaki, "Type IIA gratings recorded in B-Ge codoped optical fibre using 213nm Nd:YAG radiation", 31st European Conference on Optical Communication, **3**, pp. 563-564 (2005).

[102] E. Lindner, J. Canning, C. Chojetzki, S. Bruckner, M. Becker, M. Rothhardt and H. Bartelt, "Thermal regenerated type IIa fiber Bragg gratings for ultra-high temperature operation", Optics Communications, **284**, pp. 183-185 (2011).

[103] G. Violakis, M. Konstantaki and S. Pissadakis, "Accelerated recording of negative index gratings in Ge-doped optical fibers using 248 nm 500 fs laser radiation", IEEE Photonics Technology Letters, **18** (10), pp. 1182-1184 (2006).

[104] S.J. Mihailov, C.W. Smelser, D. Grobnic, R.B. Walker, P. Lu, H. Ding, and J. Unruh, "Bragg Gratings written in All-SiO_2 and Ge-doped core fibers with 800-nm femtosecond radiation and a phase mask", Journal of Lightwave Technology, **22** (1), pp. 94-100 (2004).

[105] C.W. Smelser, S.J. Mihailov and D. Grobnic, "Hydrogen loading for fiber grating writing with a femtosecond laser and a phase mask", Optics Letters, **29** (18), pp. 2127-2129 (2004).

[106] K.-I. Kawamura, N. Sarukura, M. Hirano and H. Hosono, "Holographic encoding of fine-pitched micrograting structure in amorphous SiO_2 thin films on silicon by a single femtosecond laser pulse", Applied Physics Letters, **78**, pp. 1038-1040 (2001).

[107] G.D. Marshall and M.J. Withford, "Annealing properties of femtosecond laser inscribed point-by-point fiber Bragg gratings", Nonlinear Photonics, OSA Technical Digest (Optical Society of America), Quebec City (Canada), paper JWA30 (2007).

[108] Y. Li, C.R. Liao, D.N. Wang, T. Sun and K.T.V. Grattan, "Study of spectral and annealing properties of fiber Bragg gratings written in H_2-free and H_2-loaded fibers by use of femtosecond laser pulses", Optics Express, **16** (26), pp. 21239-21247 (2008).

[109] C.W. Smelser, S.J. Mihailov and D. Grobnic, "Formation of Type I-IR and Type II-IR gratings with an ultrafast IR laser and a phase mask", Optics Express, **13** (14), pp. 5377-5386 (2005).

[110] D. Grobnic, C.W. Smelser, S.J. Mihailov and R.B. Walker, "Long-term thermal stability tests at 1000°C of silica fibre Bragg gratings made with ultrafast laser radiation", Measurement Science and Technology, **17**, pp. 1009-1013 (2006).

[111] S. Ishikawa, H. Kanomori, T. Kohgo, M. Nishimura and H. Yokota, "New mode-field conversion technique in optical fiber using thermal relaxation of residual stress", Proc. Conference on Optical Fiber Communication/International Conference on Integrated Optics and Optical Fiber Communication, OSA Technical Digest Series (Optical Society of America), **4**, paper TuB4 (1993).

[112] T. Erdogan, V. Mizrahi, P.J. Lemaire and D. Monroe, "Decay of ultraviolet-induced fiber Bragg gratings", Journal of Applied Physics, **76** (1), pp. 73-80 (1994).

[113] S.A. Vasiliev, O.I. Medvedkov, A.S. Bozhkov and E.M. Dianov, "Annealing of UV-induced fiber gratings written in Ge-doped fibers: investigation of dose and strain effects", Proc. Bragg Gratings, Photosensitivity, and Poling in Glass Waveguides, OSA Technical Digest (Optical Society of America), Monterey (Canada), paper MD31 (2003).

[114] S.R. Baker, H.N. Rourke, V. Baker and D. Goodchild, "Thermal decay of fiber Bragg gratings written in boron and germanium codoped silica fiber", Journal of Lightwave Technology, **15** (8), pp. 1470-1477 (1997).

[115] P. Niay, P. Bernage, M. Douay, F. Fertein, F. Lahoreau, J.F. Bayon, T. Georges, M. Monerie, P. Ferdinand, S. Rougeault, and P. Cetier, "Behavior of Bragg gratings, written in germanosilicate fibers, against γ-ray exposure at low dose rate", IEEE Photonics Technology Letters, **6** (11), pp. 1350-1352 (1994).

[116] A. Gusarov, S. Vasiliev, O. Medvedkov, I. Mckenzie and F. Berghmans, "Stabilization of fiber Bragg gratings against gamma radiation", IEEE Transactions on Nuclear Science, **55** (4), pp. 2205-2212 (2008).

[117] V.B. Neustruev, E.M Dianov, V.M. Kim, V.M. Mashinsky, M.V. Romanov, A.N. Guryanov, V.F. Khopin and V.A. Tikhomirov, "Ultraviolet radiation- and γ-radiation-induced color centers in germanium-doped silica glass and fibers", Fiber and Integrated Optics, **8** (2), pp. 143-156 (1989).

[118] A.I. Gusarov, B. Brichard and D.N. Nikogosyan, "Gamma-radiation effects on Bragg gratings written by femtosecond UV laser in Ge-doped fibers", IEEE Transactions on Nuclear Science, **57** (4), pp. 2024-2028 (2010).

[119] A.I. Gusarov, and D.B. Doyle, "Modeling of gamma-radiation impact on transmission characteristics of optical glasses", Proc. SPIE **4547**, Photonics for Space and Radiation Environment II, Toulouse (France), pp. 78-85 (2001).

[120] H. Henschel, S.K. Hoeffgen, K. Krebber, J. Kuhnhenn and U. Weinand, "Influence of fiber composition and grating fabrication on the radiation sensitivity of fiber Bragg gratings", IEEE Transactions on Nuclear Science, **55** (4), pp. 2235-2242 (2008).

[121] S. Lin, N. Song, J. Jin, X. Wang and G. Yang, "Effect of grating fabrication on radiation sensitivity of fiber Bragg gratings in gamma radiation field", IEEE Transactions on Nuclear Science, **58** (4), pp. 2111-2117 (2011).

[122] A.I. Gusarov, F. Berghmans, A. Fernandez Fernandez, O. Deparis, Y. Defosse, D. Starodubov, M. Décreton, P. Mégret and M. Blondel, "Behavior of fibre Bragg gratings under high total dose gamma radiation", IEEE Transactions on Nuclear Science, **47** (3), pp. 688-692 (2000).

[123] A. Gusarov, C. Chojetzki, I. Mckenzie, H. Thienpont and F. Berghmans, "Effect of the fiber coating on the radiation sensitivity of type I FBGs", IEEE Photonics Technology Letters, **20** (21), pp. 1802-1804 (2008).

[124] H. Henschel, S.K. Hoeffgen, J. Kuhnhenn and U. Weinand, "Influence of manufacturing parameters and temperature on the radiation sensitivity of fiber Bragg gratings", IEEE Transactions on Nuclear Science, **57** (4), pp. 2029-2034 (2010).

[125] S.K. Hoeffgen, H. Henschel, J. Kuhnhenn, U. Weinand, C. Caucheteur, D. Grobnic and S.J. Mihailov, "Comparison of the radiation sensitivity of fiber Bragg gratings made by four different manufacturers", IEEE Transactions on Nuclear Science, **58** (3), pp. 906-909 (2011).

[126] A. Fernandez Fernandez, B. Brichard, F. Berghmans and M. Décreton, "Dose-rate dependencies in gamma-irradiated fiber Bragg grating filters", IEEE Transactions on Nuclear Science, **49** (6), pp. 2874-2877 (2002).

[127] A.I. Gusarov, D. Kinet, C. Caucheteur, M. Wuilpart and P. Mégret, "Gamma radiation induced short-wavelength shift of the Bragg peak in type I fiber gratings", IEEE Transactions on Nuclear Science, **57** (6), pp. 3775-3778 (2010).

[128] A.I. Gusarov, F. Berghmans, O. Deparis, A. Fernandez Fernandez, Y. Defosse, P. Mégret, M. Décreton and M. Blondel, "High total dose radiation effects on temperature sensing fiber Bragg gratings", IEEE Photonics Technology Letters, **11** (9), pp. 1159-1161 (1999).

[129] A.Faustov, P. Saffari, C. Koutsides, A. Gusarov, M. Wuilpart, P. Mégret, K. Kalli and L. Zhang, "Highly radiation sensitive type IA FBGs for future dosimetry applications", IEEE Transactions on Nuclear Science, **59** (4), pp. 1180-1185 (2012).

[130] R.R.J. Maier, W.N. MacPherson, J.S. Barton, J.D.C. Jones, S. McCulloch, A. Fernandez Fernandez, L. Zhang and X. Chen, "Fibre Bragg gratings of type I in SMF-28 and B/Ge fibre and type IIA B/Ge fibre under gamma radiation up to 0.54 MGy", Proc. SPIE **5855**, 17th International Conference on on Optical Fiber Sensors, Brugge (Belgium), pp. 511-514 (2005).

[131] H. Henschel, D. Grobnic, S.K. Hoeffgen, J. Kuhnhenn, S.J. Mihailov and U. Weinand, "Development of highly radiation resistant fiber Bragg gratings", IEEE Transactions on Nuclear Science, **58** (4), pp. 2103-2110 (2011).

[132] A. Fernandez Fernandez, A.I. Gusarov, B. Brichard, S. Bodart, K. Lammens, F. Berghmans, M. Décreton, P. Mégret, M. Blondel and A. Delchambre, "Temperature monitoring of nuclear reactor cores with multiplexed fiber Bragg grating sensors", Optical Engineering, **41** (6), pp. 1246-1254 (2002).

[133] A.I. Gusarov, A. Fernandez Fernandez, S. Vasiliev, O. Medvedkov, M. Blondel and F. Berghmans, "Effect of gamma-neutron reactor radiation on the properties of Bragg gratings written in photosensitive Ge-doped optical fiber", Nuclear Instruments and Methods in Physics Research B, **187**, pp. 79-86 (2002).

[134] A. Gusarov, "Long-term exposure of fiber Bragg gratings in the BR1 low-flux nuclear reactor", IEEE Transactions on Nuclear Science, **57** (4), pp. 2044-2048 (2010).

[135] http://www.bureauveritas.fr.

[136] J. Bisutti, "Étude de la transmission du signal sous irradiation transitoire dans les fibres optiques", PhD thesis, Université de Saint Etienne, France (2010).

[137] L. Skuja, "Optical properties of defects in silica" in *Defects in SiO_2 and Related Dielectrics: Science and Tecnology*, Editors: G. Pacchioni, L.Skuja e D.L. Griscom; Kluwer Academic Publishers; pp. 73-116 (2000).

[138] LabRAM Aramis (Horiba Jobin Yvon) Manual.

[139] M.J. Matthews, A.L. Harris, A.J. Bruce and M.J. Cardillo, "Characterization of phosphosilicate thin films using confocal Raman microscopy", Review of Scientific Instruments, **71**, pp. 2117-2120 (2000).

[140] M. Cannas, "Point Defects in Amorphous SiO_2: Optical Activity in the Visible, UV and Vacuum-UV Spectral Regions", PhD thesis, Università degli Studi di Palermo, Italy (1998).

[141] www.newport.com/cms/brands/spectra-physics.

[142] www.princetoninstruments.com.

[143] Bruker EMX user Manual.

[144] A. Alessi, "Germanium point defects induced by irradiation in Ge-doped silica", PhD thesis, Universitá degli studi di Palermo, Italy (2010).

[145] G. Buscarino, "Experimental investigation on the microscopic structure of intrinsic paramagnetic point defects in amorphous silicon dioxide", PhD thesis, Universitá degli studi di Palermo, Italy (2006).

[146] C. P. Poole, "Electron Spin Resonance", John Wiley and Sons Inc., New York (1967).

[147] P. Paillet, J. R. Schwank, M. R. Shaneyfelt, V. Ferlet-Cavrois, R. L. Jones, O. Flament and E. W. Blackmore, "Comparison of charge yield in MOS devices for different radiation sources", IEEE Transactions on Nuclear Science, **49**, pp. 2656-2661 (2002).

[148] S. Girard, Y. Ouerdane, G. Origlio, C. Marcandella, A. Boukenter, N. Richard, J. Baggio, P. Paillet, M. Cannas, J. Bisutti, J.-P. Meunier and R. Boscaino, "Radiation effects on silica-based preforms and optical fibersI: experimental study with canonical samples", IEEE Transactions on Nuclear Science, **55**, pp. 3473-3482 (2008).

[149] A. Fernandez Fernandez, H. Ooms, B. Brichard, F. Berghmans, A. Hermanne and H. Thienpont, "Test facilities at SCK·CEN for radiation tolerance assessment: from space applications to fusion environments", (2001).

[150] P.V. Chernov, "Spectroscopic manifestations of self-trapped holes in silica", Physica Status Solidi., **B115**, pp. 663-675 (1989).

[151] E. Regnier, I. Flammer, S. Girard, F. Gooijer, F. Achten and G. Kuyt, "Low-dose radiation-induced attenuation at infrared wavelengths for P-doped, Ge-doped and pure silica-core optical fibres", IEEE Transactions on Nuclear Science, **54** (4), pp. 1115-1117 (2007).

[152] D.L. Griscom and M. Mizuguchi, "Determination of the visible range optical absorption spectrum of peroxy radicals in gamma-irradiated fused silica", Journal of Non-Crystalline Solids, **239**, pp. 66-77 (1998).

[153] K. Kajihara, L. Skuja, M. Hirano and H. Hosono, "Role of mobile interstitial oxygen atoms in defect processes in oxides: interconversion between oxygen-associated defects in SiO_2 glass", Physical Review B, **92** (1), 015504 (2004).

[154] M. Cannas, L. Vaccaro and B. Boizot, "Spectroscopic parameters related to non-bridging oxygen hole centers in amorphous-SiO_2", Journal of Non-Crystalline Solids, **352**, pp. 203-208 (2006).

[155] G.H. Sigel and M.J. Marrone, "Photoluminescence in as-drawn and irradiated silica optical fibers: an assessment of the role of non-bridging oxygen defect centers", Journal of Non-Crystalline Solids, **45**, pp. 235-247 (1981).

[156] L. Vaccaro, M. Cannas and R. Boscaino, "Phonon coupling of non-bridging oxygen hole center with the silica environment: Temperature dependence of the 1.9 eV emission spectra", Journal of Luminescence, **128**, pp. 1132-1136 (2008).

[157] M. Leone, M. Cannas and F.M. Gelardi, "Local dynamic properties of vitreous silica probed by photoluminescence spectroscopy in the temperature range 300 - 4.5 K", Journal of Non-Crystalline Solids, **232-234**, pp. 514-519 (1998).

[158] L. Vaccaro and M. Cannas, "The structural disorder of a silica network probed by site selective luminescence of the nonbridging oxygen hole centre", Journal of Physics Condensed Matter, **22** (14), 235801 (2010).

[159] S. Girard, J.-P. Meunier, Y. Ouerdane, A. Boukenter, B. Vincent and A. Boudrioua, "Spatial distribution of the red luminescence in pristine, γ rays and ultraviolet-irradiated multimode optical fibers", Applied Physics Letters, **84**, pp. 4215-4217 (2004).

[160] L. Vaccaro, M. Cannas, S. Girard, A. Alessi, A. Morana, A. Boukenter, Y. Ouerdane and R. Boscaino, "Infuence of fuorine on the fiber resistance studied through the Non Bridging Oxygen Hole Center related luminescence", Journal of Applied Physics, **113** (19), 193107 (2013).

[161] R.E. Youngman and S. Sen, "The nature of fluorine in amorphous silica", Journal of Non-Crystalline Solids, **337**, pp. 182-186 (2004).

[162] P. Dumas, J. Corset, W. Carvalho, Y. Levy and Y. Neuman, "Fluorine doped vitreous silica analysis of fiber optic preforms by vibrationnal spectroscopy,", Journal of Non-Crystalline Solids, **47** (2), pp. 239-241 (1982).

[163] N. Shimodaira, K. Saito, N. Hiramitsu, S. Matsushita and A.J. Ikushima, "Effects of fictive temperature and halogen doping on the boson peak in silica glass", Physical Review B, **72**, 024209 (2005).

[164] C.A.M. Mulder, R.K. Janssen, P. Bachmann and D. Leers, "Micro-Raman spectroscopy of fluorine-doped PCVD silica fibre preforms", Journal of Non-Crystalline Solids, **72** (2-3), pp. 243248 (1985).

[165] A.Q. Tool, "Relation between inelastic deformability and thermal expansion of glass in its annealing range", Journal of the American Ceramic Society, **29**, pp. 240-253 (1946).

[166] N. Shimodaira, K. Saito and A.J. Ikushima, "Raman spectra of fluorine-doped silica glasses with various fictive temperatures", Journal of Applied Physics, **91** (6), pp. 3522-3525 (2002).

[167] C. Martinet, V. Martinez, C. Coussa, B. Champagnon and M. Tomozawa, "Radial distribution of the fictive temperature in pure silica optical fibers by micro-Raman spectroscopy", Journal of Applied Physics, **103**, 083506 (2008).

[168] K. Kajihara, M. Hirano, L. Skuja and H. Hosono, "Role of interstitial voids in oxides on formation and stabilization of reactive radicals: interstitial HO_2 radicals in F_2-laser-irradiated amorphous SiO_2", Journal of American Chemical Society, **128**, pp. 5371-5374 (2006).

[169] L. Skuja, "Optically active oxygen-deficiency-related centers in amorphous silicon dioxide", Journal of Non-Crystalline Solids, **239**, pp. 16-48 (1998).

[170] H. Takada, Y. Suzuki, H. Kimura and M. Hirai, "Radiation-induced absorption bands due to chlorine-related defects in α-SiO_2", Conf. on Defects in Insulating Crystals, Parma (Italy), pp. 221-222 (1988).

[171] J.C. Lagomacini, D. Bravo, M. León, P. Martín, A. Ibarra, A. Martín and F.J. López, "EPR study of gamma and neutron irradiation effects on KU1, KS-4V and Infrasil 301 silica glasses", Journal of Nuclear Materials, **417**, pp. 802-805 (2011).

[172] B.R.L. Siebert and H. Henschel, "Calculation of fast neutron dose in plastic-coated optical fibres", IEEE Transactions on Nuclear Science, **45** (3), pp. 1570-1575 (1998).

[173] S. Agnello, G. Buscarino, F.M. Gelardi and R. Boscaino, "Optical absorption band at 5.8 eV associated with the E'_γ centers in amorphous silicon dioxide: Optical absorption and EPR measurements", Physical Review B, **77**, 195206 (2008).

[174] M. León, P. Martín, A. Ibarra and E.R. Hodgson, "Gamma irradiation induced defects in different types of fused silica", Journal of Nuclear Materials, **386-388**, pp. 1034-1037 (2009).

[175] P. Martín, M. León, A. Ibarra and E.R. Hodgson, "Thermal stability of gamma irradiation induced defects for different fused silica", Journal of Nuclear Materials, **417**, pp. 818-821 (2011).

[176] S. Girard, J. Baggio and J. Bisutti, "14-MeV neutron, γ-ray, and pulsed X-ray radiation-induced effects on multimode silica-based optical fibers", IEEE Transactions on Nuclear Science, **53**, pp. 3750-3757 (2006).

[177] L. Skuja and A. Naber, "Site-selective luminescence study of defects in gamma-irradiated glassy germanium dioxide", Nuclear Instruments and Methods in Physics Research B, **116**, pp. 549-553 (1996).

[178] L. Vaccaro, M. Cannas and V. Radzig, "Time-resolved luminescence of non-bridging oxygen hole centre in silica: Bulk and surface properties", Il Nuovo Cimento, **122** (6-7), pp. 677-684 (2007).

[179] M. Cannas, L. Vaccaro and R. Boscaino, "Time resolved photoluminescence associated with non-bridging oxygen hole centers in irradiated silica", Nuclear Instruments and Methods in Physics Research B, **266**, pp. 29452948 (2008).

[180] H. Hosono, Y. Abe, D.L. Kinser, R.A. Weeks, K. Muta and H. Kawazoe, "Nature and origin of the 5 eV band in SiO_2:GeO_2 glasses", Physical Review B, **46** (18), pp. 11445-11451 (1992).

[181] S. Girard, C. Marcandella, A. Morana, J. Périsse, D. Di Francesca, P. Paillet, J.-R. Macé, A. Boukenter, M. Léon, M. Gaillardin, N. Richard, M. Raine, S. Agnello, M. Cannas and Y. Ouerdane, "Combined high dose and temperature radiation effects on multimode silica-based optical fibers ", IEEE Transactions on Nuclear Science, **60** (6), pp. 4305-4313 (2013).